"Carrier Transport Properties Measurements in Wide Bandgap Materials"

by

Andre′ D. Cropper

Dissertation submitted to the Faculty of the Virginia Polytechnic Institute and State University in partial fulfillment of the requirements of the degree Doctor of Philosophy in Electrical Engineering

APPROVED:

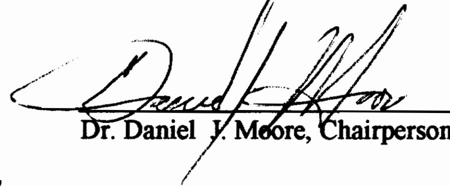

Dr. Daniel J. Moore, Chairperson

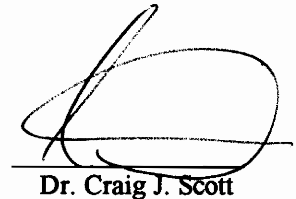

Dr. A.Elshabini-Riad

Dr. Craig J. Scott

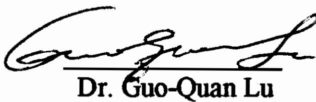

Dr. Guo-Quan Lu

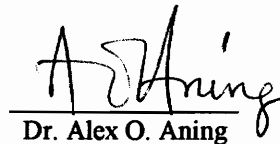

Dr. Alex O. Aning

Dr. Carl White

April 7, 1995

Blacksburg, Virginia

Key words: Diffusion Length, Carrier Lifetime, Electron Beam Induced Current

c.2

LD
5655
V856
1995
C767
c.2

"Carrier Transport Properties Measurements in Wide Bandgap Materials"

by

Andre' Dominic Anthony Peter Cropper

Dr. Daniel Moore, Chairman

The Bradley Department of Electrical Engineering

(ABSTRACT)

This dissertation examines the carrier transport properties; diffusion length, effective carrier lifetime, and resistivity in two wide bandgap materials, GaN and diamond. A combination of two methods was used to obtain these transport properties. The two were optical beam induced current (OBIC) and electron beam induced current (EBIC) time of flight transient measurements. These techniques consist of measuring the current response to the drift and diffusion of generated electron-hole pair carriers created by a short-duration pulse of radiation.

Under OBIC, a short duration pulsed optical source, with an electron beam excitation pulse time much less than the transit time of the material, was used to generate excess carriers within the absorption depth of the material. The second method of excitation, EBIC involved the use of a modified SEM with a photoemission source (L-EBIC) and a high speed pulsed thermionic electron source (T-EBIC) to generate an electron beam. This electron beam was used to create a large number of electron-hole pairs at various penetration depths within the materials.

Measurements on GaN found the diffusion length was 7.84 μm with the L-EBIC and 7.78 μm with the T-EBIC. After annealing at 900°C for 30 min. the GaN diffusion length increased to 9.89 μm (L-EBIC). The dark resistivity was 1.79 x $10^{10}\Omega$-cm, and the carrier lifetimes were 1.7 μs with L-EBIC and 3.36 & 3.9 ns with OBIC. The author believed that the L-EBIC result was a good representation of the carrier lifetime within the material, while the shorter OBIC results were due to the combine high surface and interface recombination processes. The diamond dark resistivity was found to be 6.14 x $10^{11}\Omega$-cm and the diffusion lengths were 94.1 μm and 97 μm from the L-EBIC and T-EBIC respectively. All measurements were within 10 % spread.

The real value of this contribution lies in determining the diffusion lengths in GaN and diamond by the EBIC techniques, measuring the effective surface\interface and thin film carrier lifetime of GaN utilizing a combination of OBIC and L-EBIC techniques, and evaluating the dark resistivity in GaN and diamond materials. These measurements can lead to a better understanding and exploitation of the electrophysical behavior of these materials.

Dedication

I would like to dedicate this work to my parents, Anthony and Vilma Cropper, who always gave unconditional support and encouragement throughout my life, and to my sisters, Renee and Siobhan Cropper for their motivation during my educational endeavors.

I would also like to acknowledge my other family members, friends and colleagues for their support and understanding during my perseverance of this Doctoral Program.

Also, I would like to pay homage to my ancestors, whom without their perseverance, sacrifice and hard work I would not be here today.

Acknowledgment

I would like to acknowledge Max Yoder, at The Office of Naval Research, for funding this research project (grant number: N00014-93-1-0128), S. Binari, at Naval Research Laboratory, for supplying the GaN and diamond samples used in this project, Dr. M. Spencer and Dr. G. Harris for supplying the Si and GaAs samples used in calibrating the systems used in this project. Special acknowledgement to the school of Engineering, Morgan State University for making available the Microelectronics Laboratory, where the research project was performed.

I would like to thank the faculty and staff at the school of Engineering at Virginia Polytechnic Institute and State University for their encouragement and assistance especially Dr. Daniel Moore, Chairperson and Dr. A. Elshabini-Riad. Special thanks to Loretta Estes, Graduate Coordinator for her help in navigating the Doctoral Program at Virginia Polytechnic Institute and State University, the faculty and staff at Morgan State University, especially Dr. Craig Scott, Dr. Carl White and Dr. V. Jeyasingh Nithianandam for their support and advice during the crucial stages of the project. I would also like to thank Dr. Alex Aning and Dr. Guo-Quan Lu from the Materials Science and Engineering Department for their guidance and motivation.

Table of Contents

Abstract ii
Dedication iv
Acknowledgment v
Table of Contents vi
List of Illustrations viii
List of Tables x

Chapter 1 Motivation 1
1.1 Introduction 2
1.2 Background 3

Chapter 2 Theory 6
2.1 Background Information 8
2.2 Optical Beam Induced Current 13
2.2.1 Optical Absorption 13
2.2.2 Photoinduced Current 19
2.2.3 Trapping Limitations 23
2.3 Electron Beam Induced Current 29
2.3.1 Transport Equations 29
2.3.2 Space Charge Limitations 48

Chapter 3 Scanning Electron Microscope 51
3.1 Background Information 52
3.1.1 History 52
3.1.2 Operational Overview 53
3.2 SEM Breakdown 55
3.2.1 Electron Optical System 57
3.2.2 Electron Beam/Specimen Interaction 61
3.2.3 Secondary Electron Detector 65
3.2.4 Vacuum System 66

Chapter 4 Experimental Preparation 70
4.1 Component Development 72
4.11 Faraday Cup 72
4.12 Test Fixtures 73
4.13 Photocathodes 76
4.2 Material Preparation 89
4.21 Silicon Samples 90
4.22 Gallium Arsenide Samples 97
4.23 Diamond & Gallium Nitride Samples 102

4.3 Spot Size 102
4.31 Electron Beam Spot Size 103
4.32 Optical Beam Spot Size 103

Chapter 5 Experimental Setup 108
5.1 Optical Beam Induced Current Setup 109
5.1.1 Lasing System 110
5.1.2 Second Harmonic Generator 112
5.1.3 High Speed Detection System 113
5.2 Laser-Electron Beam Induced Current Setup 116
5.2.1 Third Harmonic Generator 116
5.2.2 Modified SEM 120
5.3 Thermal-Electron Beam Induced Current Setup 122
5.3.1 Thermal Source System 122
5.3.2 High Speed Blinker 124

Chapter 6 Results, Discussion and Conclusions 130
6.1 Preliminary Evaluation 131
6.1.1 Si and GaAs Evaluation 132
6.2 GaN Testing 137
6.2.1 OBIC Testing 142
6.2.2 EBIC Testing 150
6.3 Diamond Testing 156
6.3.1 EBIC Testing 157
6.4 Discussion of Results and Conclusion 163
6.4.1 Future Work 165
6.4.2 Summary and Conclusion 165

7.0 References 168

8.0 Appendix A. EBIC Drift Velocity and Mobility Considerations 171
A.1 Transport Equations 171
A.2 Trapping Limitations 176

9.0 Vita 181

List of Illustrations

Figure 2.1 Basic Transition Process for Photon Interaction with Materials..............................15
Figure 2.2 Intrinsic and Extrinsic Transition..............................16
Figure 2.3 Distribution of Photoexcited Current in Material..............................18
Figure 2.4 Trapping and Recombination Centers..............................25
Figure 2.5 Effect of Carrier Trapping in Material..............................28
Figure 2.6 Electron-Hole Pair Generation Rates..............................34
Figure 2.7 Electron Range in Various Wide Bandgap Materials..............................35
Figure 2.8 Two Geometries of Electron Beam Interaction with Sample..............................37
Figure 2.9(a) Theoretical Induced Diffusion Current 5 μm from Contact (GaN)..............................40
Figure 2.9(b) Theoretical Induced Diffusion Current 5 μm from Contact (Diamond)..............................41
Figure 2.10(a) Theoretical Induced Diffusion Current 25 μm from Contact(GaN)..............................42
Figure 2.10(b) Theoretical Induced Diffusion Current 25 μm from Contact (Diamond)..............................43
Figure 2.11(a) Theoretical Induced Diffusion Current for 100 pA Primary Current (GaN)........44
Figure 2.11(b) Theoretical Induced Diffusion Current for 100 pA Primary Current (Diamond)..45
Figure 2.12(a) Theoretical Induced Diffusion Current for 10 μA Primary Current (GaN)..........46
Figure 2.12(b) Theoretical Induced Diffusion Current for 10 μA Primary Current (Diamond)....47
Figure 2.13 Space Charge Effects due to Drifting of Carriers..............................50
Figure 3.1 Comparison between Light Microscope and SEM..............................54
Figure 3.2 SEM Basic Component Configuration..............................56
Figure 3.3 Anode/Cathode Configuration of the Thermionic Source..............................58
Figure 3.4 Volume Created from Interaction of Electron Beam & Specimen..............................63
Figure 3.5 Generation of Secondary Electrons..............................64
Figure 3.6 Secondary Electron Detector..............................66
Figure 3.7 Vacuum System of SEM..............................68
Figure 4.1 Faraday Cup..............................72
Figure 4.2 Test Fixtures used in OBIC Experiments..............................74
Figure 4.3 Test Fixtures used in EBIC Experiments..............................75
Figure 4.4 Diamond and GaN Test Fixtures..............................75
Figure 4.5 Photocathode Test Setup..............................79
Figure 4.6 Photoemission Current vs Ultraviolet Power..............................81
Figure 4.7 Photoemission Current vs Wavelength..............................82
Figure 4.8 Photoemission Current for 355 Å Gold Photocathode..............................85
Figure 4.9 Photoemission Current for 400/2540 Å CaF_2/Au Photocathode..............................86
Figure 4.10 Photocathode Current Voltage Characteristics..............................88
Figure 4.11 Si Double Ohmic Device in Vertical Test Fixture..............................91
Figure 4.12 Current-Voltage Characteristics of Si Double Ohmic Device..............................93
Figure 4.13 Si p-n Junction Device..............................94
Figure 4.14 Current-Voltage Characteristics of Si p-n Junction Device..............................95
Figure 4.15 Si MIS Device..............................96
Figure 4.16 IV Characteristics of GaAs Double Ohmic Device..............................98
Figure 4.17 IV Characteristics of GaAs Double Ohmic Device Before Testing..............................99
Figure 4.18 IV Characteristics of GaAs Double Ohmic Device After Testing..............................100

Figure 4.19 Electron Beam Diameter Analysis Results 104
Figure 4.20 Measured Beam Spot Size vs Electron Energy 105
Figure 4.21 Optical Beam Knife Edge Experiment 106
Figure 4.22 Optical Beam Diameter Analysis Results 107
Figure 5.1 OBIC Experimental Setup 111
Figure 5.2 Second Harmonic Generator 112
Figure 5.3 Trigger System for OBIC Measurements 115
Figure 5.4 L-EBIC Experimental Setup 117
Figure 5.5 Generation of the Third Harmonic 118
Figure 5.6 T-EBIC Experimental Setup 121
Figure 5.7 Stage Current vs Acceleration Voltage 125
Figure 5.8 Stage Current vs Emission Current 126
Figure 5.9 High Speed Blinker 127
Figure 5.10 Turn-off Voltage of High Speed Blinker 129
Figure 6.1 Diffusion Length for Silicon 133
Figure 6.2 Si Double Ohmic Testing of Drift Velocity vs Electric Field 134
Figure 6.3 GaAs Double Ohmic Testing of Drift Velocity vs Electric Field 136
Figure 6.4 Dark Current for GaN Sample 138
Figure 6.5 Comparison between Theoretical & Measured Diffusion Current 140
Figure 6.6 Comparison of Theoretical & Measured Diffusion Current after Annealing 141
Figure 6.7 Photoinduced Response of GaN in OBIC System 143
Figure 6.8 Expanded View of GaN Photoinduced Response under OBIC 144
Figure 6.9 Extracted OBIC Carrier Lifetime for GaN 145
Figure 6.10 GaN Transient Response to L-EBIC in Raster Mode 147
Figure 6.11 L-EBIC Carrier Lifetime for GaN 148
Figure 6.12 GaN Transient Response for Various Electric Fields in L-EBIC 149
Figure 6.13 Diffusion length in GaN for T-EBIC and L-EBIC 151
Figure 6.14 GaN Annealed & Non-Annealed Diffusion Length 152
Figure 6.15 Dark Current for Type IIa Natural Diamond 154
Figure 6.16 Induced Current in L-EBIC for Type IIa Diamond as a Function of Acceleration Voltage 155
Figure 6.17 Comparison of Theoretical & Measured Diffusion Current in T-EBIC 158
Figure 6.18 Comparison of Theoretical & Measured Diffusion Current in L-EBIC 159
Figure 6.19 Comparison of Theoretical & Measured Diffusion Current vs Primary Current in T-EBIC 160
Figure 6.20 Diffusion Length for Type IIa Diamond 162
Figure A.1 Electron-Hole Pairs Generation in Samples 172
Figure A.2 Induced Current Response 175
Figure A.3 Induced Current Response due to Deep Traps 175
Figure A.4 Trapping Distribution in Samples 177

List of Tables

Table 3.1 Relationship Between Aperture Size and Image Quality 61
Table 4.1 Photoemission Current for various Photocathodes 83
Table 4.2 Internal Surface Resistance of the Best Photocathodes 83
Table 4.3 Photoemission Current for Improved Photocathodes 87

Chapter 1

Motivation

1.1 Introduction
1.2 Background

1.1 Introduction

The continual need for microelectronic devices that operate under severe electronic and environmental conditions (high temperature, high frequency, high power, and high radiation fields) has sustained research in wide bandgap semiconductor materials. The transport properties of GaN and diamond wide bandgap semiconductor materials meet these requirements and have tremendous potential for industrial and military applications. High frequency field effect transistors, and short wavelength optical devices have been proposed for these materials(1-3). Although research efforts involving the study of transport properties in these wide bandgap materials have made significant advances, much work is still needed to understand the material electronic properties so that the electrophysical behavior of device structures can be further understood and exploited. Carrier transport measurements serve to verify theoretical calculations and device predictions to developed the next generation of devices. These factors in turn, tend to indicate that some wide bandgap semiconductor materials hold promise for substantial improvements over today's devices. The thermal, mechanical, chemical, and electronic properties of diamond, and gallium nitride (GaN), to name a few, make these applications possible.

The electrical transport properties for GaN and diamond wide bandgap materials have presented experimental problems in their determination. The conventional Hall effect technique is difficult to perform due to the minuscule currents that flow within these materials in their intrinsic form at room temperature. The time of flight transient measurement technique was effective and provided a very direct approach in the investigation of transport properties(4-6). Using the time of flight technique, the observation of the drift/diffusion of carriers across a sample led to the extraction of the electrical transport properties. This device-oriented measurement technique is very useful, particularly for materials of high resistivity and low carrier mobility. This research project

examines the carrier transport properties (diffusion length, effective carrier lifetime and resistivity) in two of the wide bandgap materials, GaN and diamond.

Two methods were used to generate electron-hole pairs in GaN and diamond for this project. Optical beam induced current (OBIC) and electron beam induced current (EBIC) time of flight transient measurements techniques were utilized to obtain the transport properties. These techniques basically consist of measuring the current transient response to the drift and diffusion of carriers created by a short-duration pulse of radiation. When voltages are applied across the high resistivity materials with non-injecting contacts, a high field region is created, with little dark current flow. The measurement of the transit time across the high field region led to the determination of the carrier lifetime. These methods differ from other experimental techniques (Hall effect technique, Haynes-Shockley technique, and Many-Rakavy transient space charge limited currents technique) because they are based on a femto-second laser (OBIC) which produced a fast transient electron beam probe created from a high speed, laser pulsed photocathode (L-EBIC) or from an electron beam thermal pulsing source (T-EBIC).

1.2 Background

There are many similarities between the electron beam induced current (EBIC) time of flight technique and other charge injection transient techniques. Both space-charge limited (SCL) current measurements and EBIC rely on the analysis of the shape of the transient response from injected or created charge carriers. The basis for the technique was originally developed by Gudden in the 1920's[7,8], Hecht in the 30's[9] and refined later by Hofstadter in 1949[10] and Van Heerden in 1957[11]. The basic time of flight method was developed by Spear in 1962[12,13].

The drift velocity of minority carriers in narrow bandgap semiconductors was determined by the Haynes-Shockley[14,15] experiments in the early 1950's. There, the

requirement for local space-charge neutrality during carrier transit necessitates the use of extrinsic material. At high electric field strengths, pulsed bias techniques were required to prevent sample heating[16]. Although these techniques are similar to the EBIC time of flight method, the two techniques should not be confused. The Haynes-Shockley technique permits characterization of only minority carriers in low resistivity materials. In high resistivity materials, the EBIC time of flight method can be used to measure the transport properties of both carrier types on the same sample.

The analysis of transient SCL currents relies on injecting carriers at one end of a sample, with long injected pulse lengths, compared to the time the injected carriers take to transverse the length of the sample (transit time)[17,18]. The carriers in EBIC are generated by external excitation in times much less than the carrier transit time, and the number of generated carriers can be controlled so that space-charge effects are negligible.

Two methods were considered to generate electron-hole pairs, they were optical beam induced current (OBIC) and electron beam induced current (EBIC) time of flight transient measurement techniques. In the OBIC system, the majority of the carriers are generated within the absorption depth of the material (usually less than 5 micron). Experimentally, this absorption depth is one of the limiting factors that influence the carrier lifetime, because of the higher recombination velocity near the surface. As a result, carrier lifetimes obtained from the OBIC technique could be considerably shorter.

Another problem consists of employing a short duration pulsed optical source in the required spectral range, with an electron beam excitation pulse time much less than the transit time of the material in question. Here, free carrier lifetimes are the limiting factor, requiring short drift regions that results in a limitation on the size of the samples that can be used in the system. Also as the pulse width decreases, the number of photons per pulse becomes too small for the production of sufficient number of charge carriers suitable for measurements with wide band electronic equipment. Therefore, in utilizing the OBIC system to obtain transport properties all these conditions must be considered.

The second method of excitation (EBIC) involves the use of high energy fast particles, such as electrons. The process of carrier generation is completely different from optical excitation, in that, a photoemission source and a pulse thermal source is used to generate an electron beam. This electron beam interacts with the sample generating free carriers. The location and number of free carriers can be varied by altering the acceleration of the electron beam.

The main advantages of electron beam excitation over optical excitation are:

1. Generation of higher electron-hole pair rates per eV [19,20].
2. Penetration depth into the material can be varied by adjusting the primary electron beam energy[21].
3. Materials with low dark currents (near insulators) are desirable.
4. Electron and hole drift transport properties can be measured with the same structure by reversing the bias or injection point.

The main disadvantages of EBIC excitation lie in the fact that the experiment has to be carried out in a vacuum, 10^{-4} Torr or better, the elimination of space charge effects, and the high overhead cost required to purchase and maintain the equipment needed for this method.

In this research project a combination of both OBIC and EBIC techniques would be utilized, with considerations made concerning their limitations, to obtain the diffusion length, carrier lifetime and verify the high resistivity of GaN and diamond.

Chapter 2

Theory

2.1 Background Information
2.2 Optical Beam Induced Current
    2.2.1 Transport Equations
    2.2.2 Photoinduced Current
    2.2.3 Trapping Limitations
2.3 Electron Beam Induced Current
    2.3.1 Transport Equations
    3.3.2 Space Charge Limitations

2.0 Theory

This chapter deals with the theory needed to understand and extract the required transport properties for both the OBIC and EBIC systems. The chapter is divided into three sections. The first section deals with the background theory needed to understand the use of the Beam Induced Current in the materials. The section starts from the development of the continuity equation and the recombination processes used in the transport study performed here.

The second section deals with the Optical Beam Induced Current (OBIC) measurements. In this section, the theory on the OBIC is described. In the first segment of the OBIC section the equations for optical absorption are discussed. This is followed by a discussion of the photoinduced current and how it is applied to obtain the carrier lifetime. In the last segment of this section the trapping limitations that hamper the determination of the carrier transport properties are discussed.

The last section of the chapter deals with the Electron Beam Induced Current (EBIC) measurements. The fundamental theory behind the experimental EBIC approach is described. The equations that are required to obtain the diffusion lengths and carrier lifetimes are developed. This is followed by a discussion of the most destructive limitation that hampers the determination of the carrier transport properties. This limitation is space charge effects and both space charge from deep traps, as well as from the drifting carriers are discussed.

2.1 Background Information

The research project was designed around the generation of excess carriers within a sample to obtain the transport properties. The theory developed here will begin with the one dimension continuity equation for excess carriers in a transient analysis. Considering the excess electron concentration, the continuity equation in x-direction can be written as:

$$\frac{d\Delta n(x,t)}{dt} = \frac{1}{e}\frac{dJ_n}{dx} + (G_n - R_n) \qquad 2.1$$

where Δn is the excess electron concentration, J_n is the electron current density, G_n is the generation rate and R_n is the recombination rate. The current density can be written as:

$$J_n = e\mu_n nE + eD_n \frac{dn}{dx} \qquad 2.2$$

where μ_n is the mobility, E is the electrical field, e is the electronic charge and D_n is the diffusion coefficient. Substituting equation 2.2 into 2.1 gives:

$$\frac{d\Delta n(x,t)}{dt} = n(x,t)\mu_n \frac{dE}{dx} + \mu_n E \frac{dn(x,t)}{dx} + D_n \frac{d^2 n(x,t)}{dx^2} + G_n - R_n \qquad 2.3$$

Along with the continuity equation, Poisson's equation with appropriate boundary conditions must be satisfied to obtain a solution for the transport properties of the materials. Poisson's equation is given as:

$$\frac{dE}{dx} = \frac{\rho_s}{\varepsilon_s} \qquad 2.4$$

where ρ_S is the space charge density and ε_S is the semiconductor dielectric permittivity.

When light or an electron beam impinges upon a semiconducting material and electron-hole pairs are generated, the time it takes for the excess carriers to recombine is referred to as the recombination lifetime τ_r. This recombination process can occur at the surface known as surface recombination velocity (s_r) and within the material. Therefore both processes must be addressed. The recombination rate for a slightly p-type material, in the absence of any traps i.e. ($\Delta n = \Delta p$), can be expressed as[22]:

$$R = \frac{\Delta n}{\tau_r} \qquad 2.5$$

where

$$\tau_r = \left[\tau_{SRH} + \tau_{rad} + \tau_{Auger}\right] \qquad 2.6$$

and τ_{SRH} is the multi-phonon or Shockley Read-Hall recombination lifetime.

This lifetime represents the electron-hole pair recombination with deep level impurities and can be expressed as[23]:

$$\tau_{SRH} = \frac{\tau_p(n_o + n_1 + \Delta n) + \tau_n(p_o + p_1 + \Delta p)}{p_o + n_o + \Delta n} \qquad 2.7$$

and

$$n_1 = n_i \exp\left(\frac{E_T - E_i}{kT}\right) \quad , \quad p_1 = n_i \exp\left(-\frac{E_T - E_i}{kT}\right) \qquad 2.8$$

and

$$\tau_n = \frac{1}{\sigma_n v_{th} N_T} \quad , \quad \tau_p = \frac{1}{\sigma_p v_{th} N_T} \qquad 2.9$$

where E_T is the impurity energy level, E_i is the intrinsic energy level, N_T is the impurity concentration, σ_n and σ_p are the electron and hole capture cross sections respectively. The energy given off by this process is through lattice vibrations or phonons. This lifetime is dominant whenever impurities or defects are present in the material and are particularly important for indirect bandgap material. τ_{rad} is the radiative lifetime, where electron-hole pair recombination occurs from band-to-band giving off energy through photons and is defined as(24):

$$\tau_{rad} = \frac{1}{\left[B(p_o + n_o + \Delta n)\right]} \qquad 2.10$$

where B is the radiative recombination coefficient. This lifetime is dominant for direct bandgap materials. τ_{Auger} is the Auger recombination lifetime and is a three carrier process where the energy is transferred to a third carrier and can be described by(25):

$$\tau_{Auger} = \frac{1}{\left[C_p\left(p_o^2 + 2p_o\Delta n + \Delta n^2\right) + C_n\left(n_o^2 + 2n_o\Delta n + \Delta n^2\right)\right]} \qquad 2.11$$

where C_p and C_n are the Auger recombination coefficients. This lifetime is observed when there are a large number of majority carriers or excess minority carriers in both direct or indirect bandgap materials. Also for high injection or doping levels and in narrow bandgap materials this lifetime is the dominant recombination process.

The recombination lifetime for high resistivity slightly p-type materials can be simplified for both low level injection and high level injection processes. For low level injection ($\Delta n << p_o$) equation 2.6 can be re-written as:

$$\tau_r = \tau_{SRH} + \frac{1}{Bp_o} + \frac{1}{C_p P_o^2} \quad 2.12$$

and for high level injection ($\Delta n >> p_o$)

$$\tau_r = \tau_{SRH} + \frac{1}{B\Delta n} + \frac{1}{(C_p + C_n)\Delta n^2} \quad 2.13$$

The surface recombination velocity is expressed as:

$$s_r = \frac{R_s}{\Delta n_s} \quad 2.14$$

where the subscript "s" refers to the quantity at the surface and R_S is the surface SRH recombination rate which is similar to the bulk SRH recombination rate. These recombination rates can be expressed as:

$$R = \frac{\sigma_n \sigma_p \upsilon_{th} N_T (pn - n_i^2)}{\sigma_n (n + n_1) + \sigma_p (p + p_1)} = \frac{pn - n_i^2}{\tau_p (n + n_1) + \tau_n (p + p_1)} \quad 2.15$$

$$R_s = \frac{\sigma_{ns} \sigma_{ps} \upsilon_{th} N_{iT} (p_s n_s - n_i^2)}{\sigma_{ns} (n_s + n_{1s}) + \sigma_{ps} (p_s + p_{1s})} = \frac{s_n s_p (p_s n_s - n_i^2)}{s_n (n_s + n_{1s}) + s_p (p_s + p_{1s})} \quad 2.16$$

where

$$s_n = \sigma_{ns} v_{th} N_{it} \qquad , \qquad s_p = \sigma_{ps} v_{th} N_{it} \qquad 2.17$$

and p_S and n_S are the hole and electron concentration/cm^2 at the surface respectively, and N_{it} is the interface density given as[26]:

$$N_{iT} = kTD_{iT} \qquad 2.18$$

where D_{iT} is the interface trap density. Combining the last five equations, the surface recombination velocity becomes:

$$s_r = \frac{s_n s_p (p_{so} + n_{so} + \Delta n_s)}{s_n (n_{so} + n_{is} + \Delta n_s) + s_p (p_{so} + p_{is} + \Delta p_s)} \qquad 2.19$$

therefore, for the low level injection:

$$s_r = s_n \qquad 2.20$$

and for the high level injection:

$$s_r = \frac{s_n s_p}{s_n + s_p} \qquad 2.21$$

2.2 Optical Beam Induced Current

When a photon interacts with a material, one of three processes occurs, absorption, spontaneous emission or stimulated emission. For the two energy level model (E_1 and E_2) of an atom, any transition between these states involves the emission or absorption of a photon with energy $h\nu_{12} = E_2 - E_1$ where ν_{12} is the photon frequency. The difference $E_2 - E_1$ can be referred to as the bandgap of the material, E_g. Figure 2.1 shows the three basic processes possible for the transition between two energy levels, where E_1 is the ground state (at room temperature most of the atoms are here) and E_2 is the excited state.

When an incident photon with energy equal to the bandgap interacts with the material, then the electron in the energy state E_1 absorbs the photon and is excited to energy state E_2, as shown in Figure 2.1 (a). This change in energy state is referred to as the absorption process. However, this state is unstable and after some time, without external stimulation, the electron returns to the ground state giving off a photon of energy $h\nu_{12}$. This is referred to as the spontaneous emission process, Figure 2.1 (b). If the electron at E_2 collides with another photon with energy $h\nu_{12}$, the result is the release of another photon with the same energy $h\nu_{12}$. This process is called stimulated emission and is shown in Figure 2.1 (c). The dominant operating process for the generation of free carriers in the OBIC experiment is by absorption.

2.2.1 Optical Absorption

The optical absorption process of a photon by the material in the OBIC measurement system, can be used to obtain the carrier lifetime and diffusion length. After the excess electron-hole pairs have been generated, the incident optical source is suddenly

turned off. With the source eliminated a measurement is made of the excess carrier decay rates, from which the recombination properties can be determined.

As the semiconductor material absorbs the photon with energy equal to the energy band, electron-hole pairs are generated with energies $h\nu = E_g$. When the material absorbs photon energy greater than E_g, not only are electron-hole pairs created, but excess energy is given off as heat $(h\nu - E_g)$. These processes are referred to as intrinsic transitions or band-to-band transitions. If however the photon has energy less than the bandgap energy, then the photon absorbs only if available energy states are present in the bandgap, due to doping, impurities or defects. This process is called extrinsic transition. All three of these transitions are shown in Figure 2.2. For materials with relatively high resistivity and low background concentration, that are highly sensitive at the operating wavelengths, the dominant absorption process is by intrinsic transition.

When the material is excited with energy $h\nu > E_g$, some of the photon flux traveling through is absorbed, as shown in Figure 2.3. Here, w is the thickness of the wafer, D is the minority carrier diffusion coefficient, τ is the minority carrier lifetime, L is the minority carrier diffusion length, s_1 and s_2 are the recombination velocities at the front and back surfaces, and R is the reflectivity given by:

$$R = \frac{(n_o - n_1)^2 + k_1^2}{(n_o + n_1)^2 + k_1^2} \tag{2.22}$$

and is related to the transmission coefficient by:

$$T = \frac{1 - R^2 \exp\left(\frac{-4\pi w}{\lambda}\right)}{1 - R^2 \exp\left(\frac{-8\pi w}{\lambda}\right)} \tag{2.23}$$

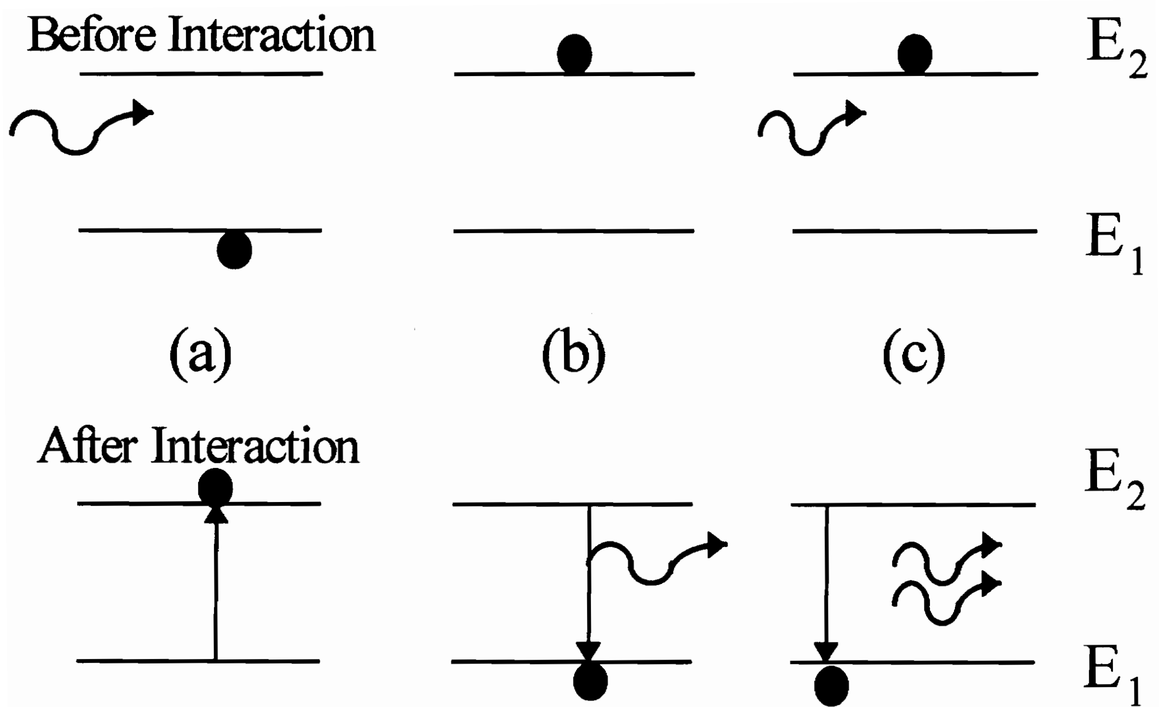

Figure 2.1. Basic Transition Process for Photon Interaction with Material.

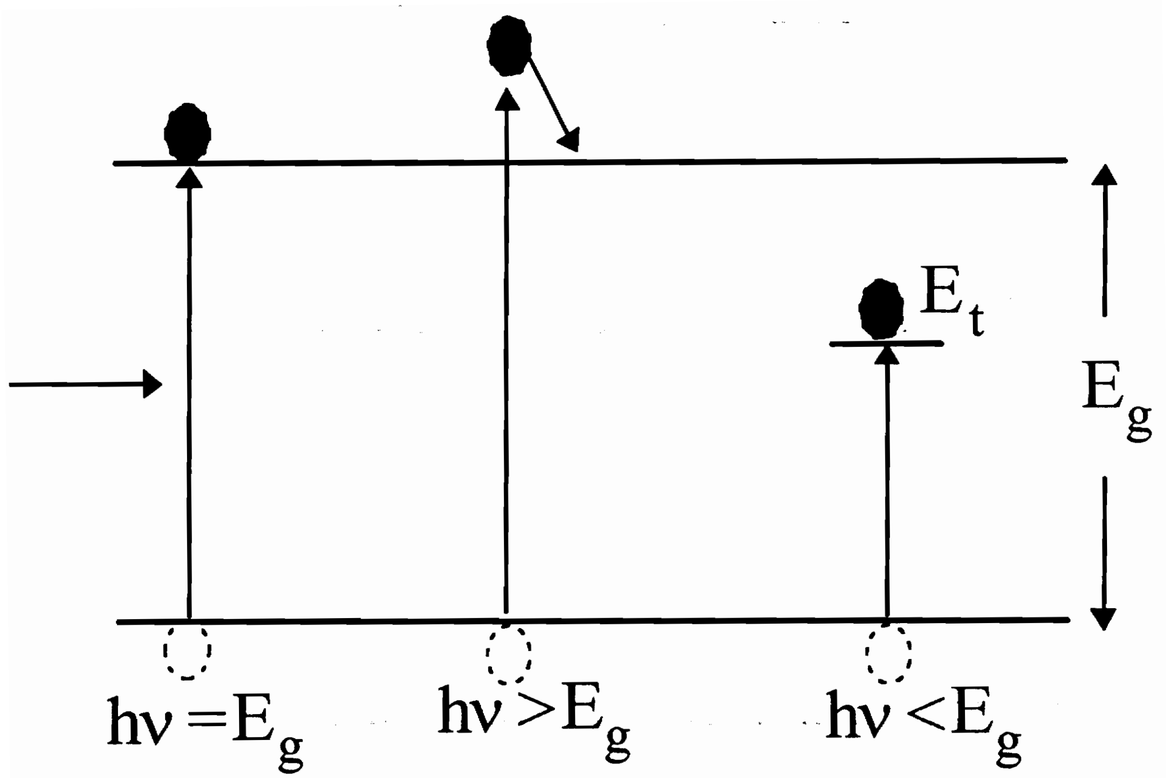

Figure 2.2. Intrinsic and Extrinsic Transition.

where k_1 is the absorption constant, λ is the wavelength and n is the refractive index. This absorption is proportional to the intensity of the flux, and is given by $\alpha\,\Phi(x)\Delta x$, where Δx is an infinitely thin section where the photons are absorbed, and α is the absorption coefficient, which is a function of hν in units of cm^{-1}

$$\alpha = \frac{4\pi k_1}{\lambda} \qquad 2.24$$

The continuity of photon flux passing through an infinitely thin section, as shown in Figure 2.3, can be written as:

$$\Phi(x+\Delta x) - \Phi(x) = \frac{d\Phi(x)}{dx}\Delta x = -\alpha\,\Phi(x)\Delta x \qquad 2.25$$

therefore

$$\frac{d\Phi(x)}{dx} = -\alpha\,\Phi(x) \qquad 2.26$$

where the decrease in intensity of the photon flux is due to absorption and is represented by the negative sign. At the front surface (x = 0), the boundary condition is given by $\Phi(x) = \Phi_O$, and the solution to equation 2.26 is:

$$\Phi(x) = \Phi_o \exp(-\alpha\, x) \qquad 2.27$$

and at the back surface where x = w, the portion of the flux that exits is:

$$\Phi(w) = \Phi_o \exp(-\alpha\, w) \qquad 2.28$$

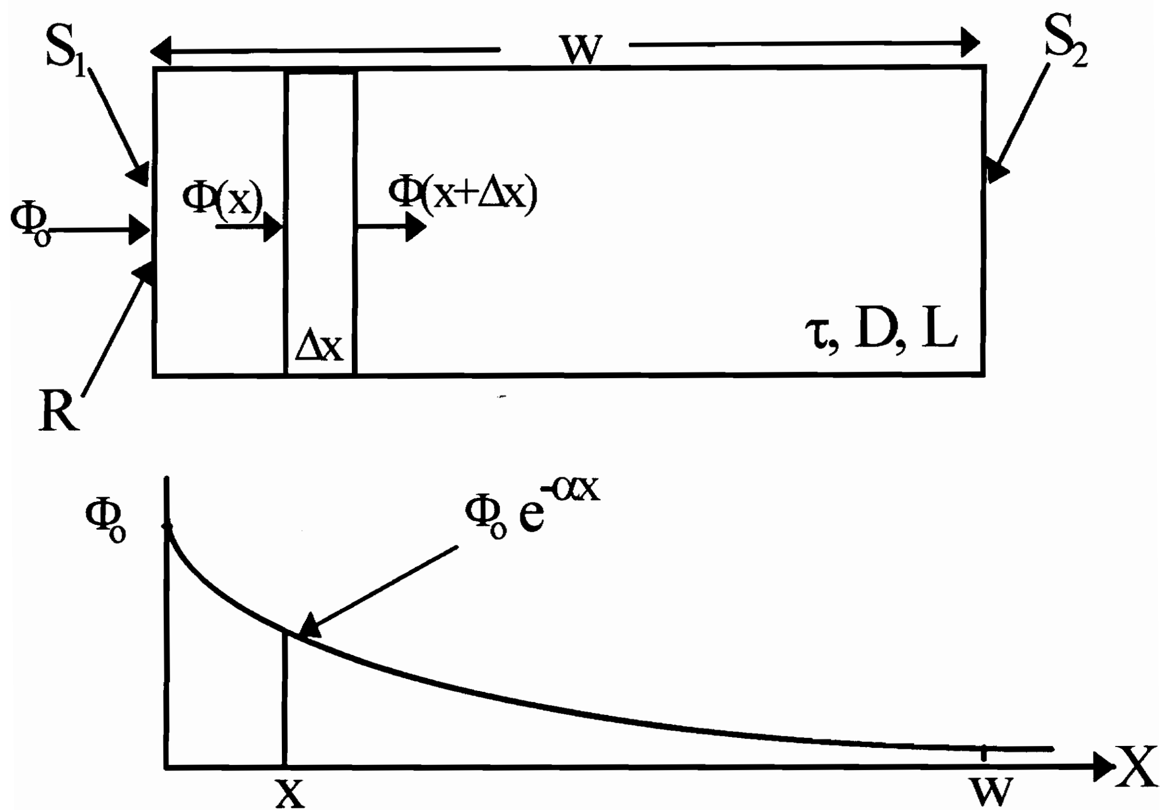

Figure 2.3. Distribution of Photoexcited Carriers in Material.

where the absorption coefficient decreases rapidly as it approaches the value of the cutoff wavelength λ_C, which is given as:

$$\lambda_c = \frac{1.24}{E_g} \quad \mu m \qquad 2.29$$

because the band-to-band absorption decreases rapidly for $h\nu > E_g$.

2.2.2 Photoinduced Currents

For the materials to produce carrier generated currents from optical excitation, they must first absorb the photons and then transport the excess carriers to the ohmic contact where they are collected. When this occurs the result is an increase in the conductivity of the material. This increase in conductivity is a direct result of an increase in the number of carriers within the material. The equation for conductivity is:

$$\sigma = e(\mu_n n + \mu_p p) \qquad 2.30$$

which is a function of the carrier concentrations $n = n_O + \Delta n$ and $p = p_O + \Delta p$. Therefore, to obtain the induced current from the material, the number of excess carriers must first be determined.

For the one dimension transient case the continuity equation for the excess minority carrier concentration $\Delta n(x)$ in the absence of an applied field is:

$$\frac{d\Delta n(x,t)}{dt} = D_n \frac{d^2 n(x,t)}{dx^2} + G_n(x,t) - \frac{\Delta n(x.t)}{\tau} \qquad 2.31$$

where the recombination rate R = $-\Delta n(x, t)/\tau$. However, the carrier decay is to be monitored with the optical source turned off ($G(x, t) = 0$) and with boundary conditions:

$$\frac{d\Delta n(x,t)}{dx} = s_1 \frac{\Delta n(0,t)}{D} \qquad \text{at } x = 0 \tag{2.32}$$

$$\frac{d\Delta n(x,t)}{dx} = -s_1 \frac{\Delta n(w,t)}{D} \qquad \text{at } x = w \tag{2.33}$$

Therefore the general solution subject to these boundary conditions is:

$$\Delta n(x,t) = \sum_{m=1}^{\infty} \Delta n(x,0)\exp\left(-\frac{t}{\tau_m}\right) \tag{2.34}$$

where $\Delta n(x, o)$ is the number of carriers generated in a unit volume at time zero for a given incident photon flux, and τ_m is the excess carrier decay time constant. For optical excitation the carrier-carrier scattering is dominated because of high level injection and this leads to a reduction in the drift mobility.

The excess carrier decay is comprise of the combination of a sum of exponential, for which the dominant mode decay is given by τ_{eff} (effective lifetime) and is a function of the bulk recombination lifetime:

$$\frac{1}{\tau_{eff}} = \frac{1}{\tau} + D\beta_1^2 \tag{2.35}$$

where β_1 is the first root of

$$\tan(\beta w) = \frac{\beta(s_1 + s_2)D}{(\beta^2 D^2 - s_1 s_2)} \qquad 2.36$$

and

$$D = \frac{D_p D_n (n + p)}{(nD_n + pD_p)} \qquad 2.37$$

the ambipolar diffusion coefficient and w is the thickness of the material. The equation for the effective lifetime is valid as long as $w << (Dt)^{1/2}$, and can be written as:

$$\frac{1}{\tau_{eff}} = \frac{1}{\tau} + \frac{1}{\tau_s} \qquad 2.38$$

where τ_S is the surface recombination velocity and there are two cases of interest. The first case is for low surface recombination velocity ($s_1 = s_2 = s \rightarrow 0$), therefore:

$$\tau_s = \frac{w}{2s} \qquad 2.39$$

and the second case is for high surface recombination velocity ($s_1 = s_2 = s \rightarrow \infty$), therefore:

$$\tau_s = \frac{w^2}{\pi^2 D} \qquad 2.40$$

Hence by measuring the transient response of the carriers and curve fitting the decay portion of the curve, the effective carrier lifetime can be obtained. The true lifetime is always greater than the measured lifetime because of the relationships between s, w and τ, or if more than bulk recombination process is present[27]. This multiple recombination process is possible, if the material has many different impurities, with different concentrations and capture cross sections. Also, if more than one recombination process is present or high level injection occurs (as in the OBIC case of this project), the decay may not be purely exponential, because the lifetimes are now functions of the excess carrier concentrations. Details of these processes can be found in the discussion by Blakemore[28].

The resultant photocurrent from the material can be found from the current density equation (2.2) and the area of the contacts:

$$I_{ph} = JA = \left(J_{diff} + J_{drif}\right)A = \left(eD_n \frac{d\Delta n(x)}{dx} + \sigma_n E\right)A \qquad 2.41$$

where E is an applied electric field across the sample. Substituting the conductivity (equation 2.30) into the expression in equation 2.41 gives:

$$I_{ph} = \left(eD_n \frac{d\Delta n(x)}{dx} + e\mu_n \Delta n(x) E\right)A = \left(eD_n \frac{d\Delta n(x)}{dx} + e\Delta n(x) v_d\right)A \qquad 2.42$$

where v_d is the drift velocity of the carriers. The photoinduced current is a function of the electric field, excess carrier concentration and drift velocity.

Therefore in the absence of the electric field (diffusion current), the photoinduced current can be expressed as:

$$I_{ph} = \left(eD_n \frac{d\Delta n(x)}{dx} \right) A \approx I_o \exp\left(- t/_{\tau_m} \right) \qquad 2.43$$

which is only a function of generated carriers and excess carrier decay time.

In the OBIC measuring system the dominant generation process is the band-to-band absorption. The recombination processes that are present are: SRH recombination because of the impurities in the materials, as well as, the Auger recombination because of the high injection rate produced from the optical absorption of the material. The main scattering process is the carrier to carrier scatting because of the high carrier densities produced from irradiation of the material. Therefore for any given photoinduced current the excess carrier lifetime can be extracted by curve fitting the decay portion of the transient response (equation 2.43).

2.2.3 Trapping Limitations

For high level injection the effective recombination transient decay is not a simple exponential. The additional trapping centers that capture and release the carriers must be considered. If an excess electron-hole pair is release in the material, then instead of directly recombining, the carrier is captured by an impurity site and then after some time released (for example by thermal or photoelectric excitation), then the carrier is considered to be a trapped. If however, it directly recombines with an opposite polarity charge, then it is considered a recombination site. Figure 2.4 shows the difference between a trapping center and a recombination center.

The types of capture that most likely occur in this experiment are coulomb attraction (center with electric charge of the opposite sign), neutral center and coulomb repulsion (center with electric charge of same sign), with the dominant process being coulomb attraction. A more detail review of capture process can be found elsewhere[29]. The published data on this subject are quite varied, but they seem to indicate that the coulomb attraction process can be expressed as:

$$\sigma = k_1 T^{-n} \qquad 0 \le n \le 3.5 \tag{2.44}$$

where k_1 is a constant and n = 0 is for deep traps.

The σ is a strong function of E in two ways[30], the first is by reducing the potential barrier effect and is called the Poole-Frenkel effect:

$$\sigma = k_2 E^{-3/2} \tag{2.45}$$

This is only important when the potential barrier is lowered by the field by at least an order of kT. The second is heating effect of the carriers by the electric field and is called the Lax theory[31]:

$$\sigma = k_3 \left(T_{lattice} / T_{carrier} \right)^2 \tag{2.46}$$

where $T_{lattice}$ and $T_{carrier}$ are the lattice and carrier temperatures, respectively.

The σ is related to the mean free drift time before trapping by:

$$\tau^+ = \frac{1}{N_T \sigma v} \tag{2.47}$$

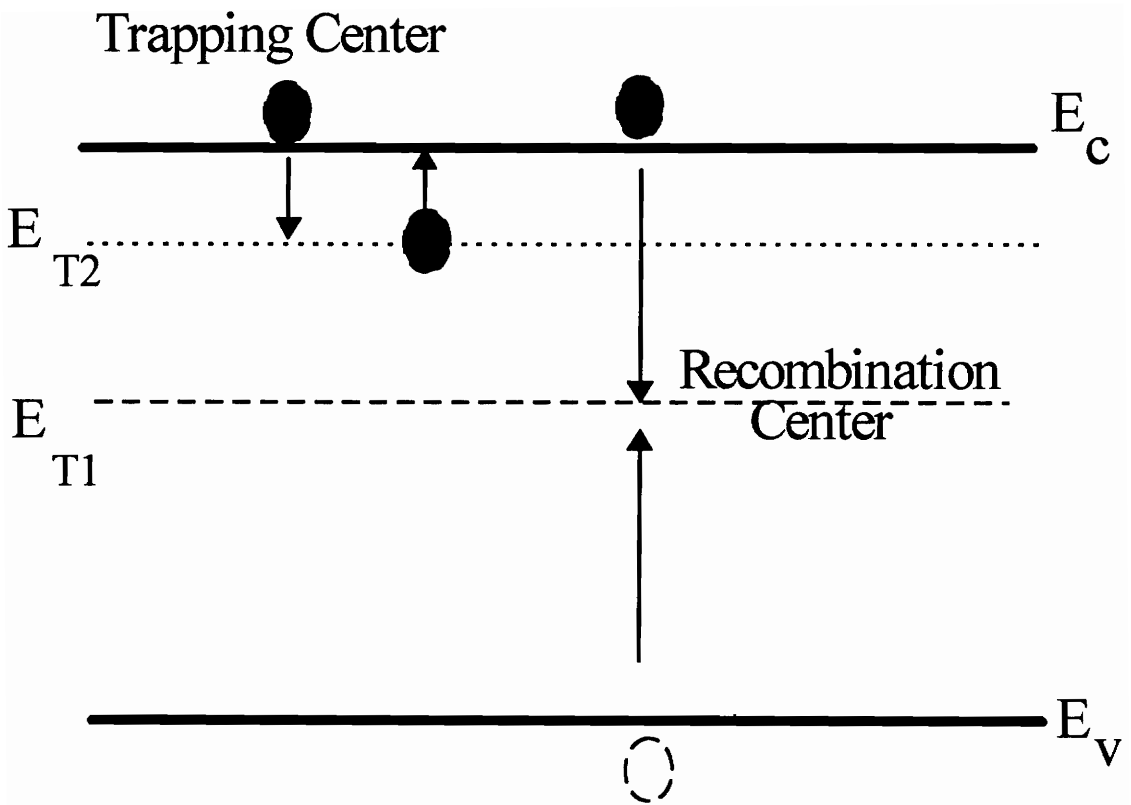

Figure 2.4. Trapping and Recombination Centers.

where N_T is the effective concentration of the trapping centers and ν is the carrier velocity. The carriers are released to the relevant band mostly by thermal energy and electric field effects. For a coulomb attractive trap, the probability per unit time for thermal release is:

$$\frac{1}{\tau_D} = \gamma \exp\left(-\frac{E_T}{kT}\right) \qquad 2.48$$

where τ_D is the mean de-trapping time, E_T is the trapping energy and γ is the escape frequency. The de-trapping process is strongly dependent on temperature. At any given temperature range only one trapping center plays a dominant role. The product of the mean free drift time before trapping to the mean free de-trapping time is given by(32):

$$\frac{\tau^+}{\tau_D} = \frac{N_c}{N_T} \exp\left(-\frac{E_T}{kT}\right) \qquad 2.49$$

where N_C is the density of states in the conduction band.

When the injected carriers interact with the trapping centers, the transient output waveform is due to the transit time T_R, the mean free drift time τ^+, and the mean de-trapping time τ_D. Two cases of trapping are of special interest to this research project. The first is single level trapping and no de-trapping and the other is single level trapping and de-trapping. In the first case, the carriers are not released to the bands, therefore the free carrier concentration N is a simple exponential decay and can be expressed as:

$$N = N_o \exp\left(-\frac{t}{\tau^+}\right) \qquad 2.50$$

where N_O is the number of created free carriers. For electrons injected close to one contact with a constant velocity, the current expression in equation 2.41 can be written as[33,34]:

$$I(t) = I_o \exp\left(-\frac{t}{\tau^+}\right) \qquad \text{for } t \le T_R \qquad 2.51$$

$$I(t) = 0 \qquad \text{for } t > T_R \qquad 2.52$$

Figure 2.5 shows one of the effects of carriers being trapped in the material before reaching the collecting contact ($T_R / \tau^+ > 1$). The figure shows the exponential decay due to traps producing a sharp break at $t = T_R$. If the slope of the exponential is plotted on semi-log paper, the mean free drift time can be extracted.

The second case is trapping with de-trapping, and there are two conditions under which they may occur. The first results in a reduction in mobility because most of the carriers are trapped initially near the contact where they were generated ($\tau^+ << T_R$). Therefore many trapping and de-trapping events occur before the carriers reach the collecting contact. In the second condition, the carriers travel a great distance before they are trapped ($0.1\ T_R < \tau^+ < T_R$), resulting in a fast rise time of the output pulse. After some distance one or more trapping/de-trapping events occur ($\tau_D > \tau^+$) and the response slows down with a step at $t = T_R$[34].

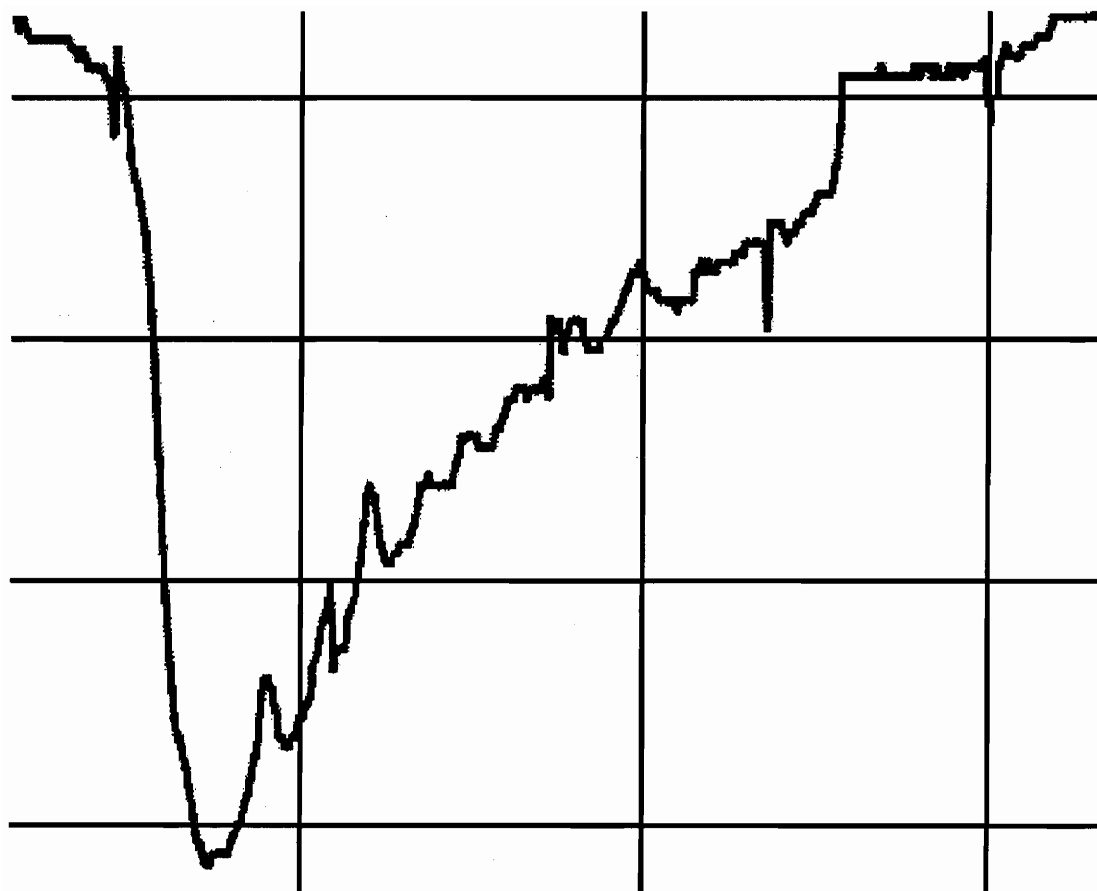

Figure 2.5. Effect of Carrier Trapping in Material.

2.3 Electron Beam Induced Current

The Electron Beam Induced Current (EBIC) measurement system is quite similar in theory, as well as experimentally, to the OBIC system. So the theory developed in the OBIC section can be applied to EBIC with a few minor changes. In the OBIC system the generation of electron-hole pairs was achieved by the absorption of optical power by the material. In the EBIC, the generation of these electron-hole pairs is achieved by the interaction of an electron beam with the material under a vacuum.

The interaction results in a volume of electron-hole pairs generated at some distance within the material. This depth, where the volume is formed, is referred to as the electronic range and is the first to be developed in this section. The other parameters developed are the number of electron-hole pairs generated for a single electron interaction, and the generation rate or volume of electron-hole pairs generated per second. The final portion of this section is devoted to the equations surrounding the photoinduced current for diffusion and the carrier lifetime. Also some reference is made to the main limiting conditions that affect the measurement of the transport properties by the EBIC system. Further discussion on the drift velocity, drift mobility and trapping limitations can be found in Appendix A.

2.3.1 Transport Equations

When the electron beam interacts with the material under test, the kilovolt electron loses energy during penetration by scattering from valence and core electrons. The result is a small deviation of the electron from its original direction. This deviation can be regarded as a continuous slowing down of the electron. Also, the electron may undergo scattering with a small loss of energy from nuclei within the material and so result in a

large angular change from the original trajectory. This condition leads to the focused electron beam being spread out within the material leaving a trail of low energy secondary electrons and holes along the path between large angle scattering events. The depth the electron would penetrate if it underwent no large angle scattering is called the electronic range. This results in the generation of electron-hole pairs mostly on the beam axis.

The original work performed on the penetration depth of an electron into a material was by Everhart and Hall in 1971[35]. They used Gruen[36] findings of the depth-dose curve in air and expanded it for the use in solids. Gruen discovered two important points. The first was the range energy relationship of $R_g=4.57E_B^{1.75}$ μg/cm², where E_B is the energy in keV of the incident electron beam (from 5 keV to 25 keV), and secondly, by normalizing the penetration distance to the R_g the depth-dose curve is invariant. Everhart's and Hall's showed that an empirical form can be written for the electronic range, such that:

$$R_e = kE_B^{\alpha} \qquad 2.53$$

where k is a constant that is a function of the atomic number and density of the material, and α is a constant that varies with the atomic number. The expression for k can be expressed as:

$$k = \frac{9.40x10^{-12} I^2 A}{Z\rho} \quad \text{g/cm}^2 \qquad 2.54$$

where A is the atomic weight in grams, I is an empirical expression related to the atomic number (Z) and given as:

$$I = \left(9.76 + 58.8Z^{-1.19}\right)Z \qquad 2.55$$

and ρ is the density of the material. The constant α was found to be slightly higher than 1.75 for Z < 10, approximately equal to 1.75 for 10 < Z < 40, and between 1.44 and 1.6 for Z > 30[37,38]. All of these values are valid for an energy range of 1 keV to 25 keV[39]. Substituting equations 2.54 and 2.55 into equation 2.53 gives:

$$R_e = \left(\frac{2.41x10^{-11}}{\rho}\right)E^{1.75} \qquad \text{cm} \qquad 2.56$$

where ρ is in (g/cm³) and E is in (eV).

The number of electron-hole pairs generated within the material is a function of the backscattering at the surface, the ratio of incident energy to electron-hole pair energy, depth of penetration into the material and the radial spread. As the electron beam penetrates the MUT, it defocuses with diameter d >> R_e. The spreading at its periphery is negligible and the one dimensional depth-dose function given by Everhart and Hall is:

$$g(z) = \int g(r,z)dr = 0.6 + 6.21z - 12.4z^2 + 5.69z^3 \qquad 2.57$$

where z is expressed in units of R_e, and the number of electron-hole pairs generated per incident electron is given as:

$$N_{eh} = \langle g \rangle (1-f)\left[\frac{E}{E_{eh}}\right] \qquad 2.58$$

where <g> is the normalized distribution of g(z) to R_e, f is the fraction of the electron energy that is reflected at the surface, which was estimated by Feibiger and Muller to be half the backscattered coefficient[40]. The quantity E_{eh} is the electron-hole pair energy required to be formed by the incident electron and is a constant that is independent of beam energy and type of incident energy.

Klein in 1968 showed that it is related to the bandgap energy of the material[41] (for diamond with energy 5.5 eV the E_{eh} number was between 15.5 eV and 18 eV) and can be expressed as :

$$E_{eh} = 3.2E_g \tag{2.59}$$

Substituting these expressions into equation 2.58, the results give the number of electron-hole pair generated by an induced electron as:

$$N_{eh} = \left(0.6 + 6.21z - 12.4z^2 + 5.69z^3\right)\left(1 - 0.5\alpha\right)\left[\frac{E}{3.2E_g}\right] \tag{2.60}$$

which can be rewritten in terms of the mean energy of the backscattered electrons (E_{bs}), the backscattering coefficient (α) and the average energy required to create one electron-hole pair ($E_{eh} \approx 3.2E_g$) as[42]:

$$N_{eh} = \left(\frac{E}{E_{eh}}\right)\left[1 - \left(\frac{\alpha E_{bs}}{E}\right)\right] \tag{2.61}$$

When an electron penetrates the material, knowledge of the generated rate of electron-hole pairs in a volume per second is required to predict the induced current produced from this electron. This generation rate is a function of the atomic number Z, the number of electron-hole pairs generated N_{eh}, the depth of penetration into the material R_e, electron beam of energy E and the incident electron beam current I_b. For atomic numbers less than 15 the volume is approximated as a pear shape, for atomic numbers between 15 and 40 the shape can be approximated as a sphere, and for atomic numbers

greater than 40 the shape is hemi-spherical. From this information the electron-hole pair generation rate G can be expressed as[43]:

$$G(r,z) = \left[\frac{N_{eh}\, I_b}{e\ Volume} \right] \qquad 2.62$$

For the samples used in this research project the volume of electron-hole pairs was approximated as a sphere of $\{(4/3)\pi(R_e/2)^3\}$. Then electron-hole pair generation rate G is:

$$G = \left[\frac{N_{eh}\, I_b}{e\ (4/3)\pi\ (R_e/2)^3} \right] = \left[\frac{8.5 \times 10^{50}\, p^3 I_b}{E_{eh}\, E^{4.25}} \right] \quad cm^{-3} s^{-1} \qquad 2.63$$

where backscattering is neglected. Graphs of the electron range and generation rates versus electron energy are shown in Figures 2.6 and 2.7 respectively.

The interaction of the electron beam with the semiconductor sample can take place in a variety of geometries. Figure 2.8 shows two geometries considered in this project. Changes in the electron induced current (I_{ph}) collected by the contact can be effected by moving the beam in the x-direction in Figure 2.8(a), and in the y-direction for Figure 2.8(b). Also, changes in the depth of penetration can be achieved by changing the beam energy I_p in both Figure 2.8(a & b) respectively.

For the measurement of the diffusion current, the geometry in Figure 2.8 (b) was used. This geometry assumes that the surface recombination rate is infinite, and the concentration and density of the recombination centers are uniform within the material. Therefore the equilibrium minority carrier density (n_o), the diffusion length (L_n), and the lifetime (τ) are all constant within the material. Also, assuming that the electron beam is

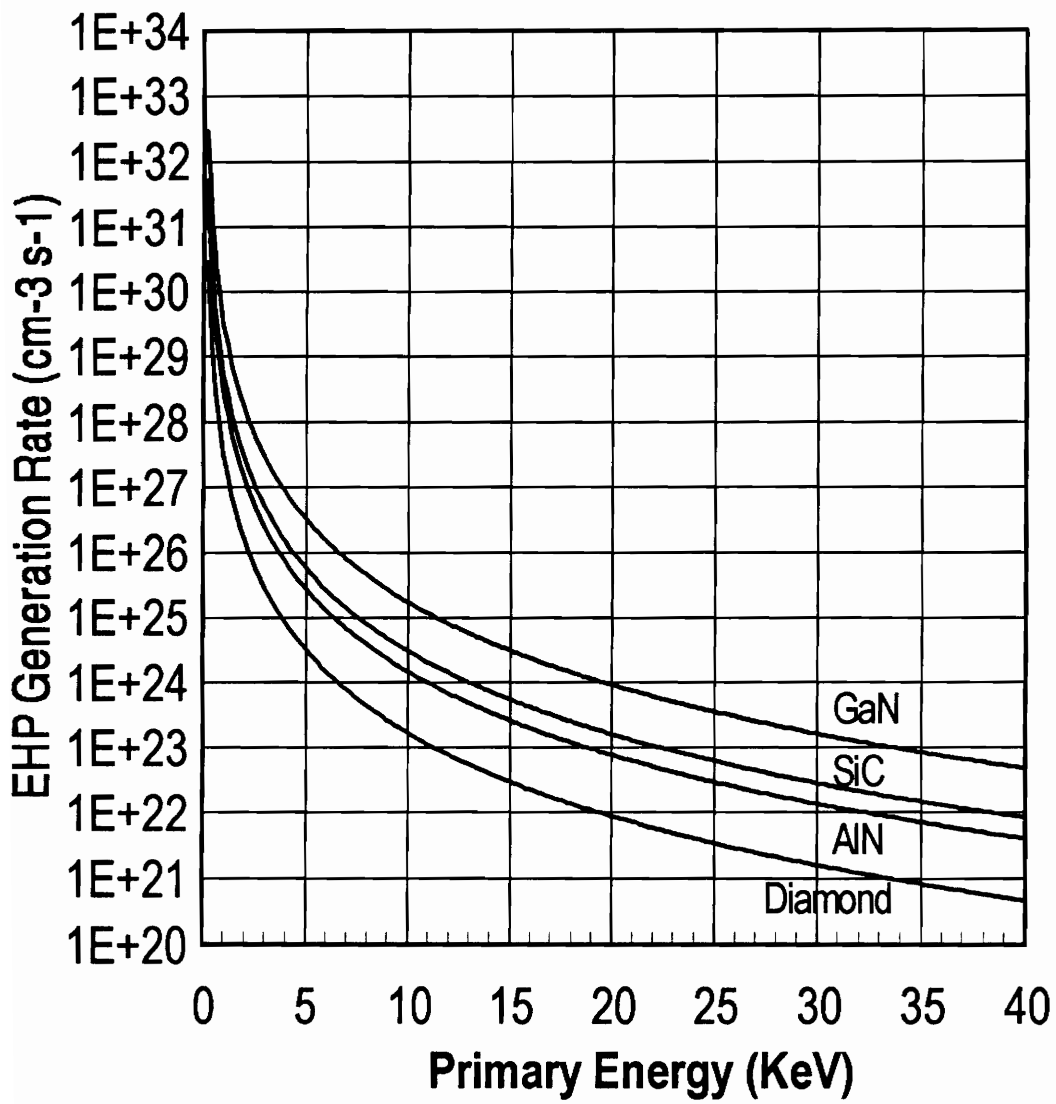

Figure 2.6. Electron-Hole Pair Generation Rates.

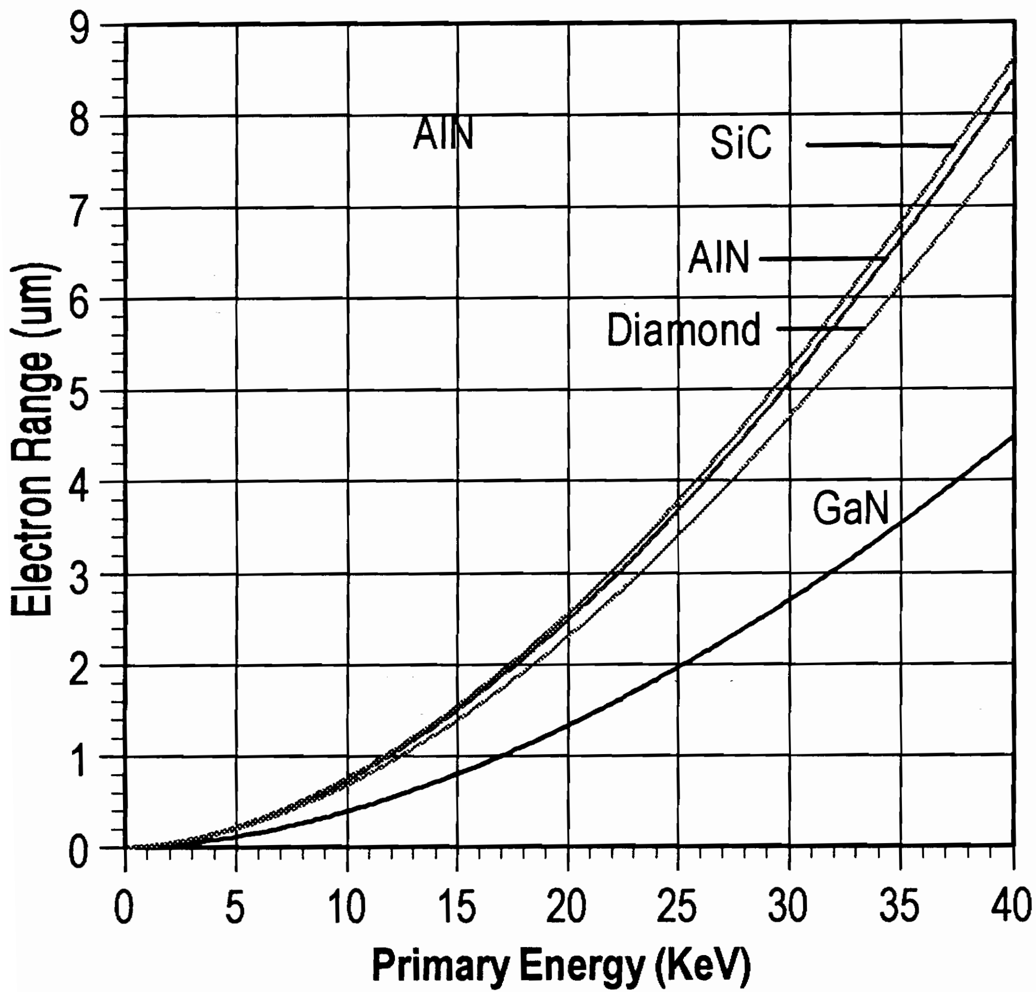

Figure 2.7. Electron Range for Various Wide Bandgap Materials.

incident to the surface at a distance (d) from the collection point to the injection point. Then the steady state density of excess minority carriers at some point P(x,y,z) within the material is given by[44]:

$$\Delta n = \frac{G}{4\pi D}\left[\frac{\exp\left(-r_1/L_n\right)}{r_1} - \frac{\exp\left(-r_2/L_n\right)}{r_2}\right] \qquad 2.64$$

where

$$r_1 = \left[x^2 + y^2 + (z - R_e)^2\right]^{1/2} \qquad 2.65$$

$$r_2 = \left[x^2 + y^2 + (z + R_e)^2\right]^{1/2} \qquad 2.66$$

So the induced current flowing from the collecting contact is given by:

$$I_{ph} = eD\int_{d}^{+\infty}\int_{-\infty}^{+\infty}\frac{\partial \Delta n}{\partial z}\Big|_{z=0} dxdy \qquad 2.67$$

where $L_n << d$, $R_e L_n << d^2$ and $R_e << d$ have been assumed. The solution for the induced diffusion current is given by[45]:

$$I_{ph} \approx A\frac{\exp(-d/L_n)}{d^{3/2}} \qquad 2.68$$

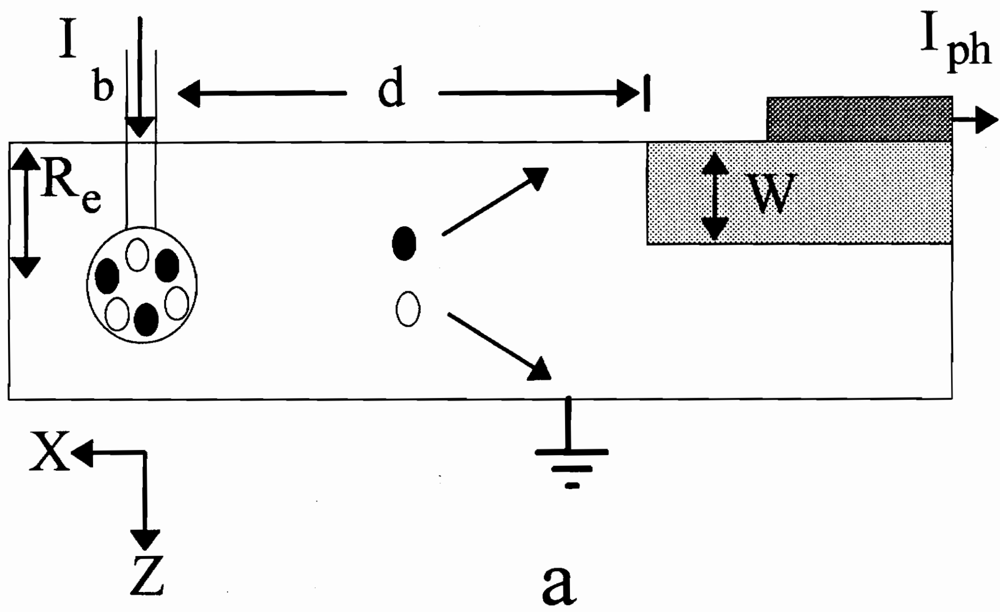

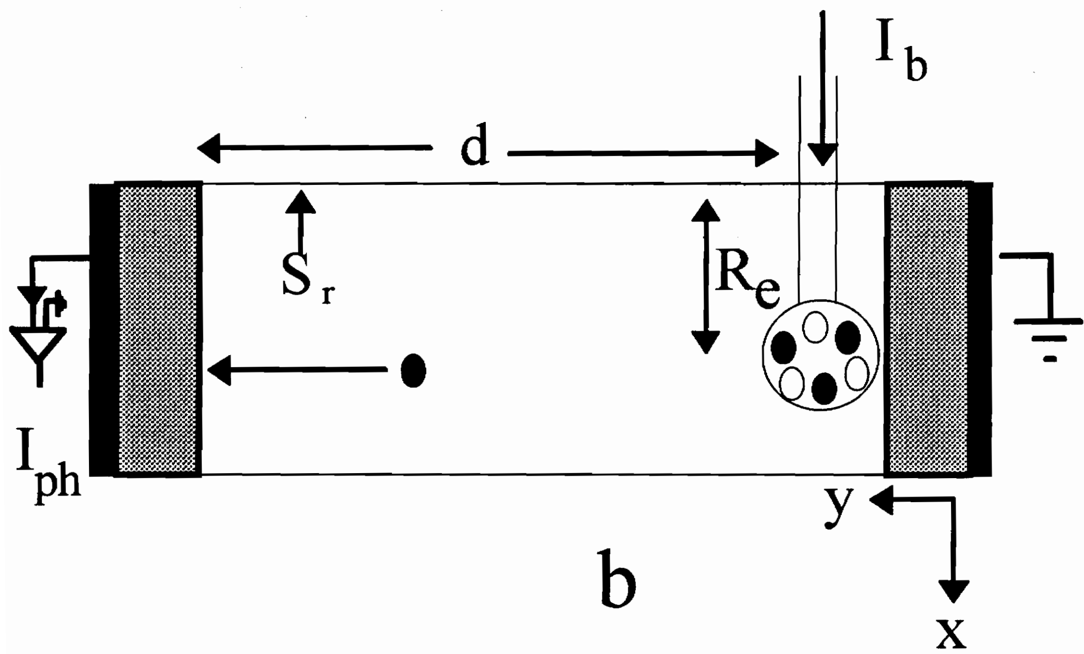

Figure 2.8. Two Geometries of Electron Beam Interaction with Sample.

where $A = \left[eG'R_e L_n^{1/2} \Big/ \sqrt{2\pi} \right]$ is a constant, R_e is the depth of the electron-hole pair volume and L_n is the diffusion length. Substituting the constant A into the electron induced diffusion current equation gives:

$$I_{ph} = \left[\frac{eG'R_e L_n^{1/2}}{\sqrt{2\pi}\, d^{3/2}} \right] \exp\left(-\frac{d}{L_n} \right) \qquad 2.69$$

where $G' = (N_{eh} I_b)/e$, and provided that $S_r >> D_n/L_n$.

Consequently, an electron beam creates electron-hole pairs a distance d from the edge and some of the minority carriers diffuse to the junction to be collected. Hence, the induced diffusion current (I_{ph}) decreases with an increase in d, due to the bulk and surface recombination. Therefore, the distance the carriers traveled was kept as small as possible in order to obtain the diffusion current. The surface recombination effects would be significantly reduced if the beam penetration depth could be increased. This can be accomplished by adjusting the acceleration voltage.

Shown in Figure 2.9 and 2.10 are the steady state or diffusion currents plotted as a function of the primary electron beam energy. These plots are based on the theoretical analysis, for 5 μm and 25 μm from the contact, for GaN and diamond respectively. All of these charts show that the induced current increases with increase in the primary beam current. Also, the closer the electron beam is to the measuring contact the larger the induced current, because carriers lost to diffusion is greatly reduced with a decrease in the distance the carriers' travels. Figure 2.11 and 2.12 shows the effect of increasing diffusion current with a decrease in the distance from the measuring contact for primary currents of 100 pA and 10 μA.

Along with determining the diffusion length from the steady state electron induced diffusion current, the minority carrier lifetime can be extract from the transient analysis

using a stationary pulsed beam. Under transient conditions, the one dimensional continuity current equation for excess electron concentration $\Delta n(x)$ given in equation 2.31, has the same solution for the EBIC measurement. If the carrier decay is monitored after the electron pulse, G = 0, the general solution is given by:

$$\Delta n(x,t) = \sum_{m=1}^{\infty} \Delta n(x,0) \exp\left(-\frac{t}{\tau_m}\right) \qquad 2.70$$

where $\Delta n(x, o)$ is the number of carriers generated in a unit volume at time zero for a given incident electron beam energy, and τ_m is the effective excess carrier decay time constant. The term τ_m can be obtained by fitting the decaying portion of the transient response to the above equation.

As can be seen from the time of flight technique for both OBIC and EBIC, the two are very similar except for the method of electron hole pair generation. The measurement of the transport properties relies on a well defined pulse of generated carriers and all affects must be made to maintain this pulse. Any tendency to broaden the sheet of carriers must be avoided, especially when dealing with the contacts. The result of non-ohmic contacts leads to injection of excess charge carriers into the material during and after the transit of the generated electron hole pairs. Therefore to obtain accurate carrier transport properties excess charge carriers must be avoided and space charge limitations must be addressed.

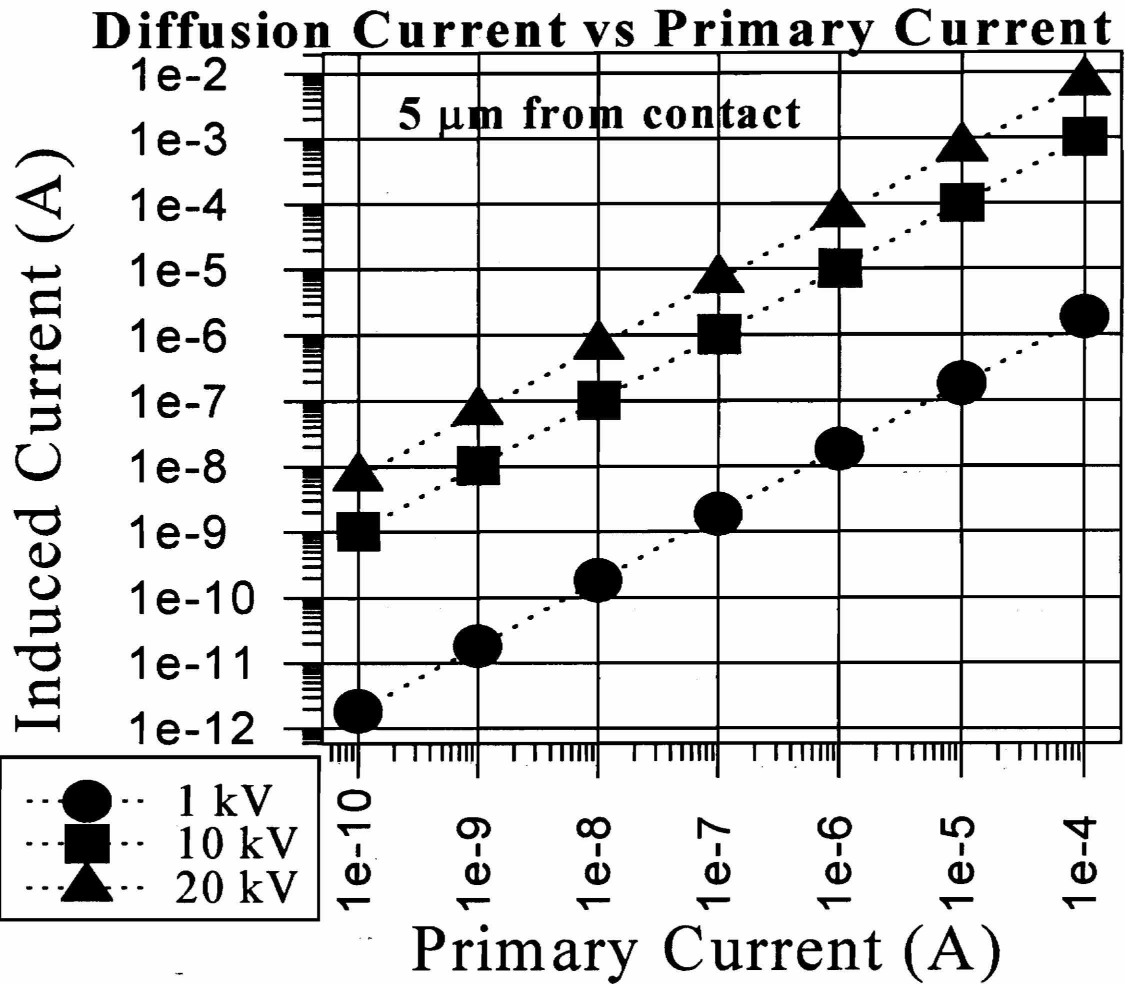

(a) GaN

Figure 2.9. Theoretical Induced Diffusion Currents 5 μm from Contact.

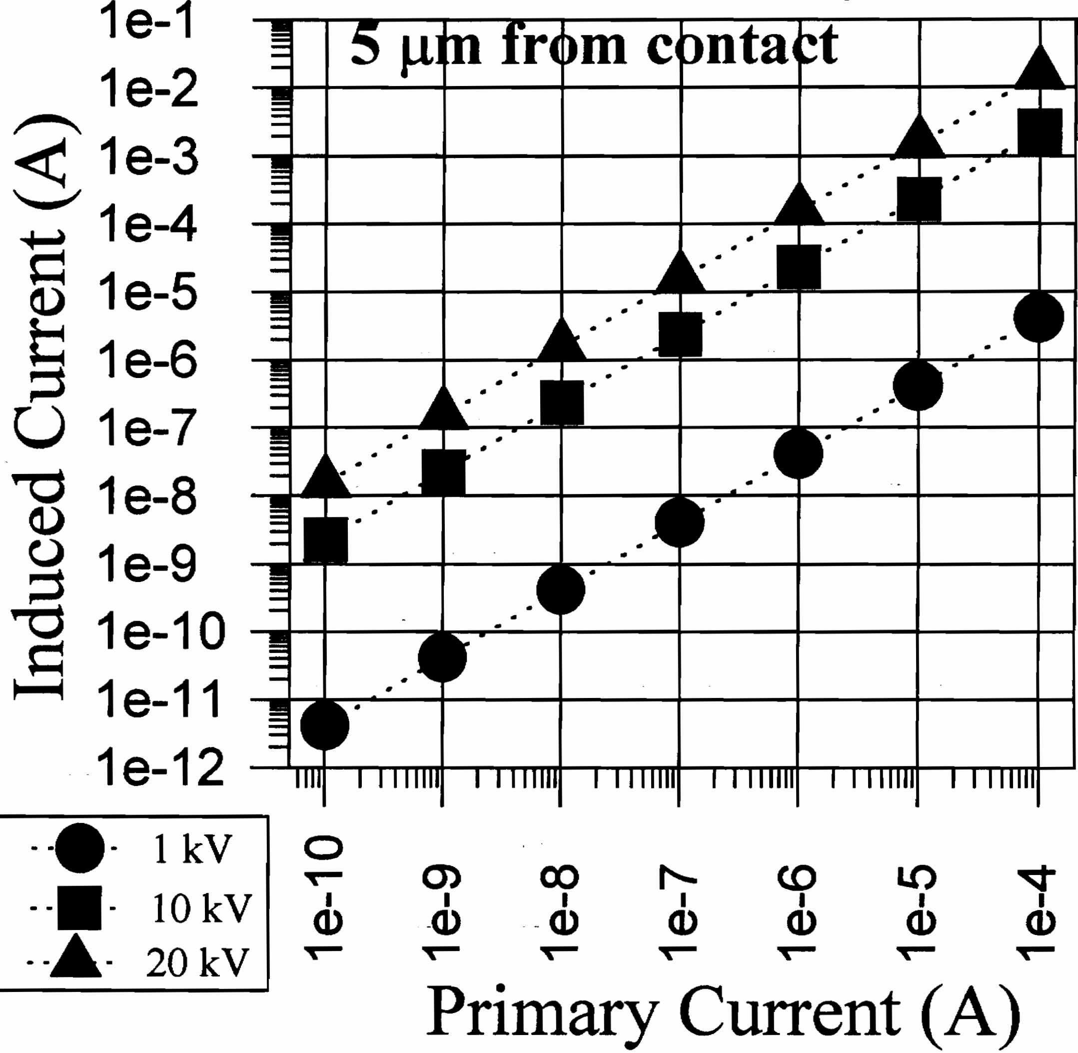

(b) Diamond

Figure 2.9. Theoretical Induced Diffusion Currents 5 μm from Contact.

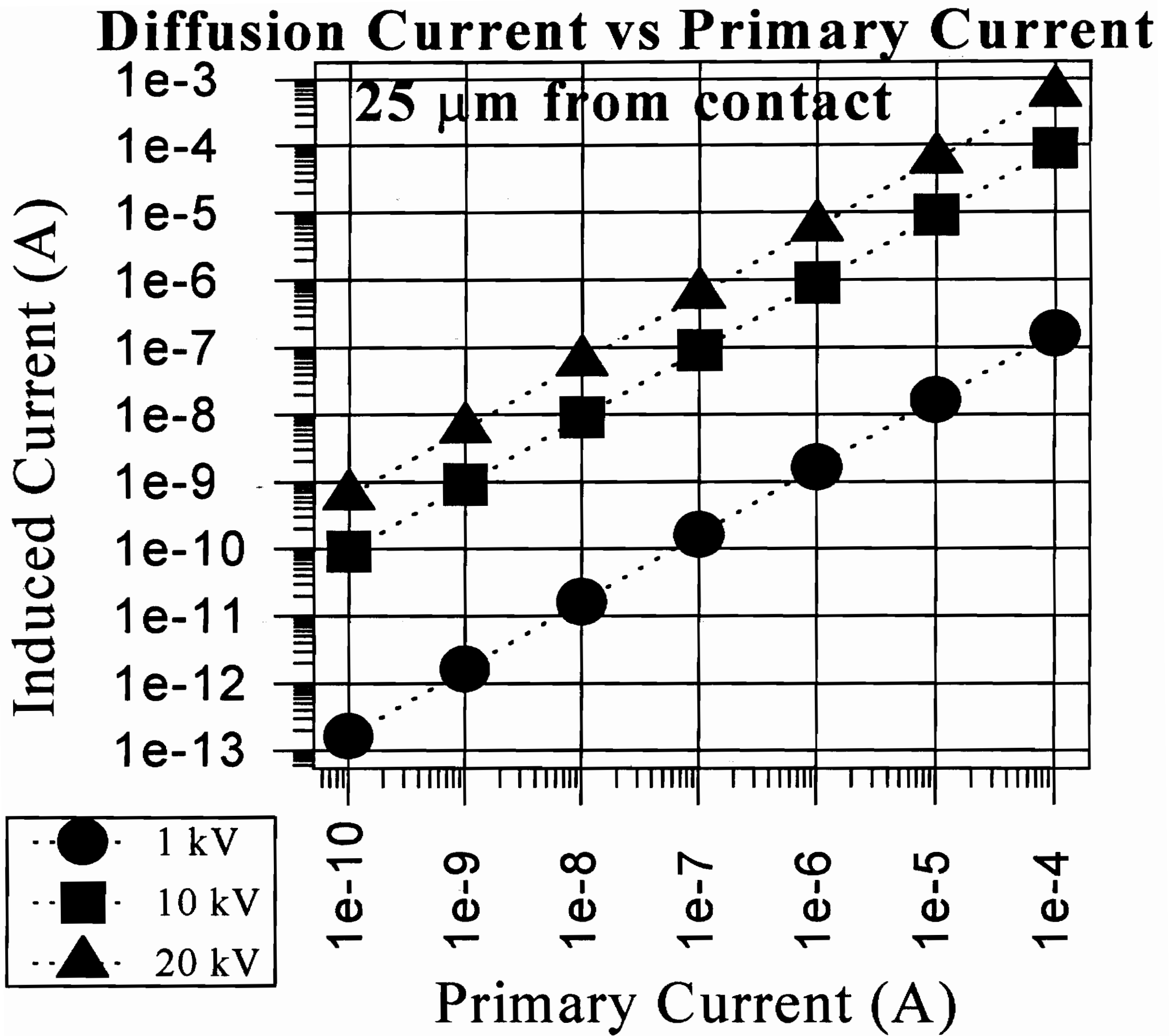

(a) GaN

Figure 2.10. Theoretical Induced Diffusion Currents 5 μm from Contact.

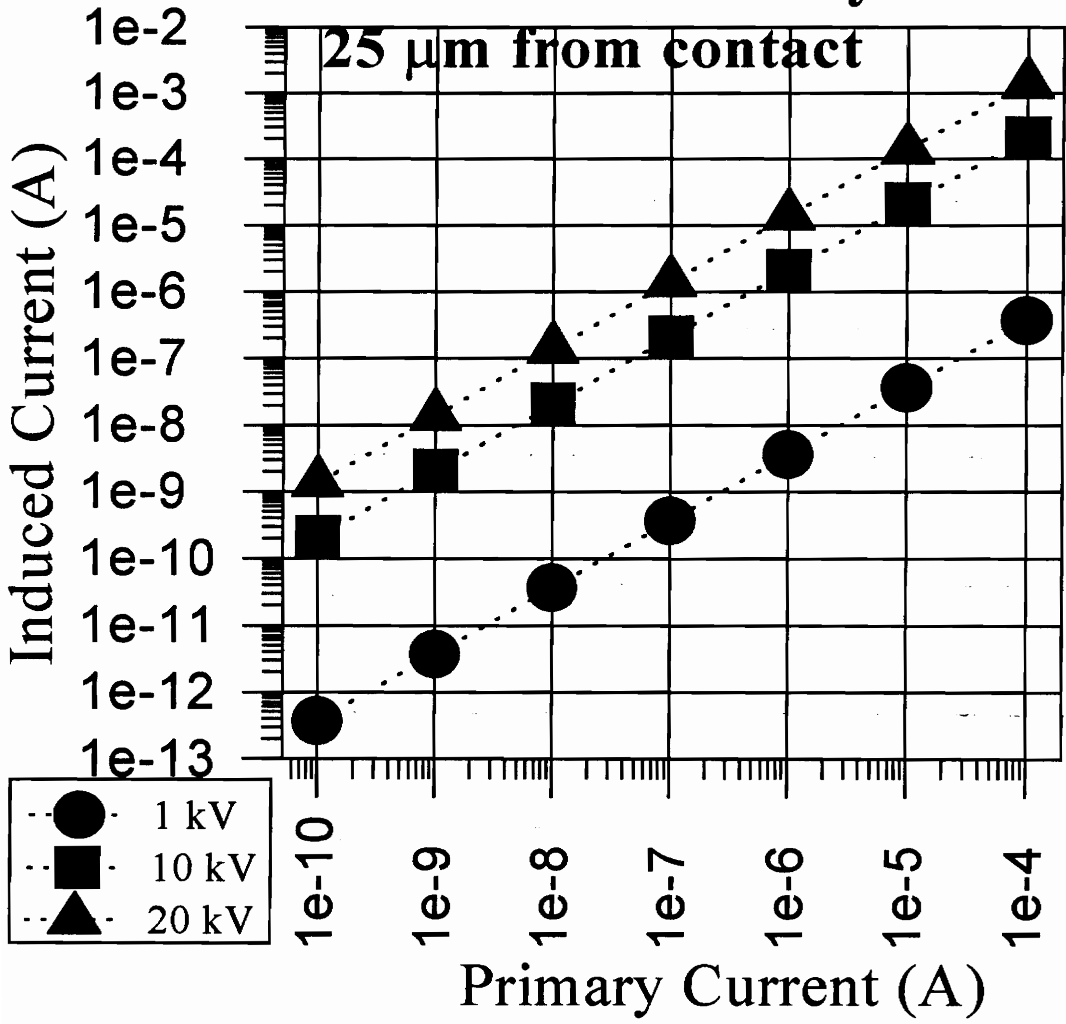

(b) Diamond

Figure 2.10. Theoretical Induced Diffusion Currents 5 μm from Contact.

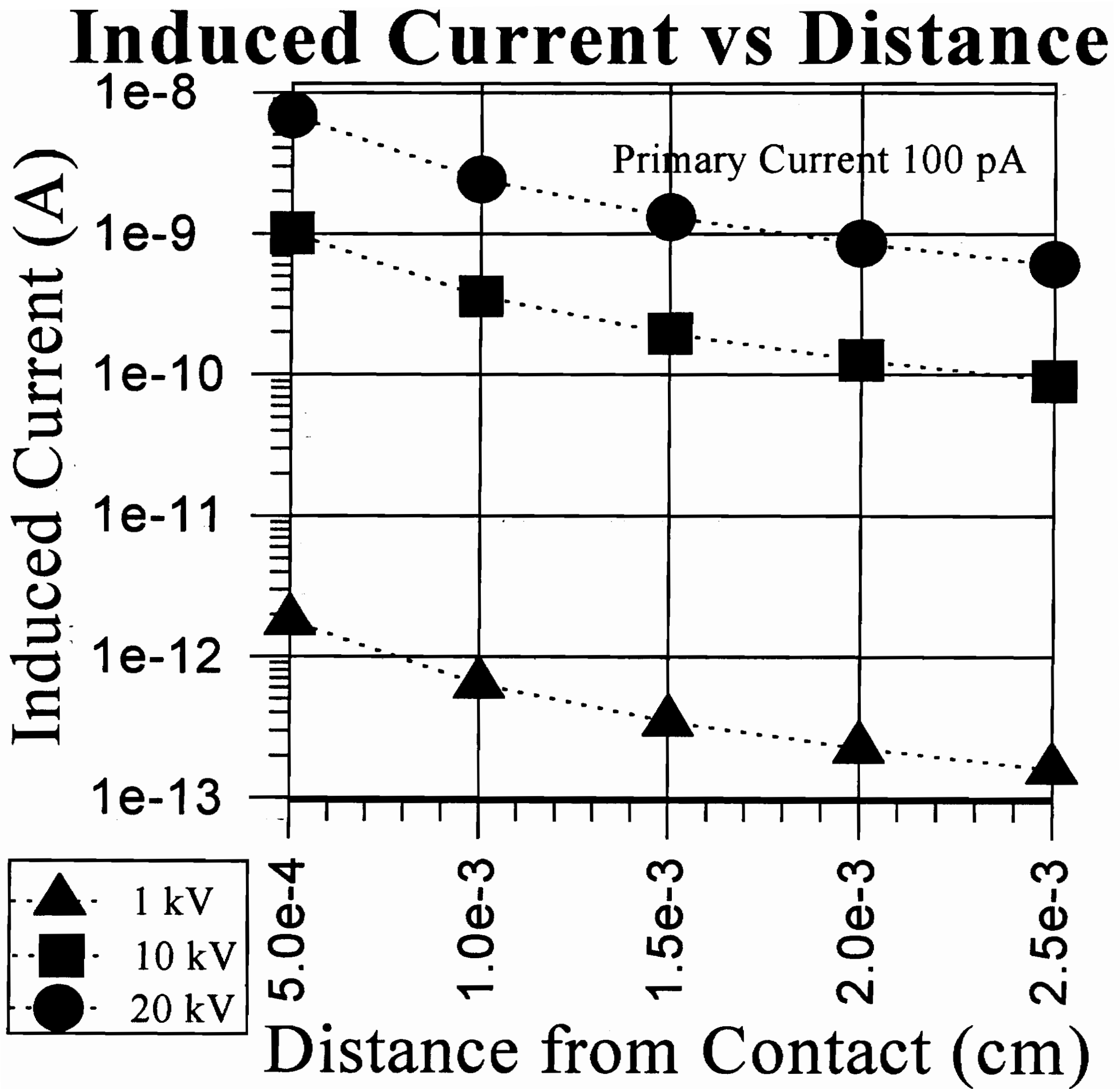

(a) GaN

Figure 2.11. Theoretical Induced Diffusion Currents for 100 pA Primary Current.

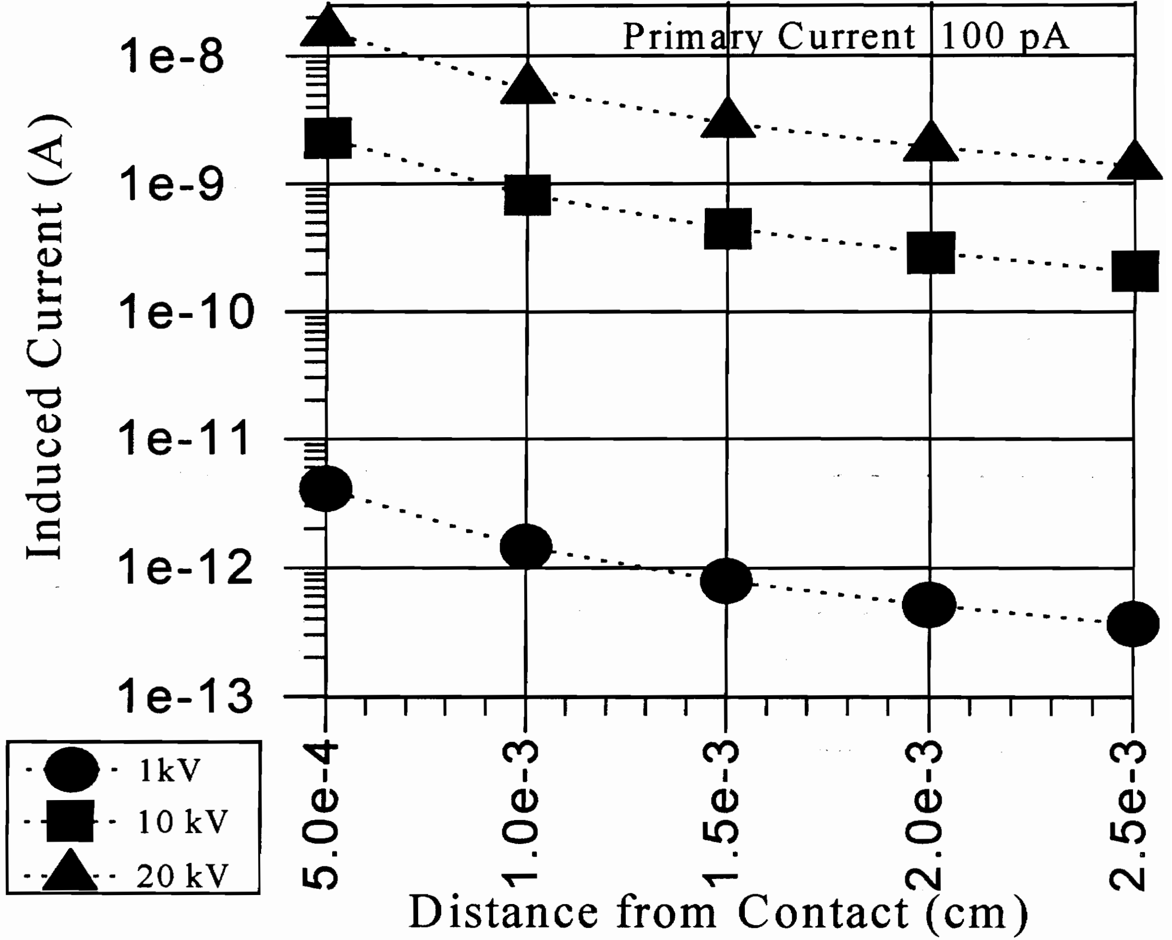

(b) Diamond

Figure 2.11. Theoretical Induced Diffusion Currents for 100 pA Primary Current.

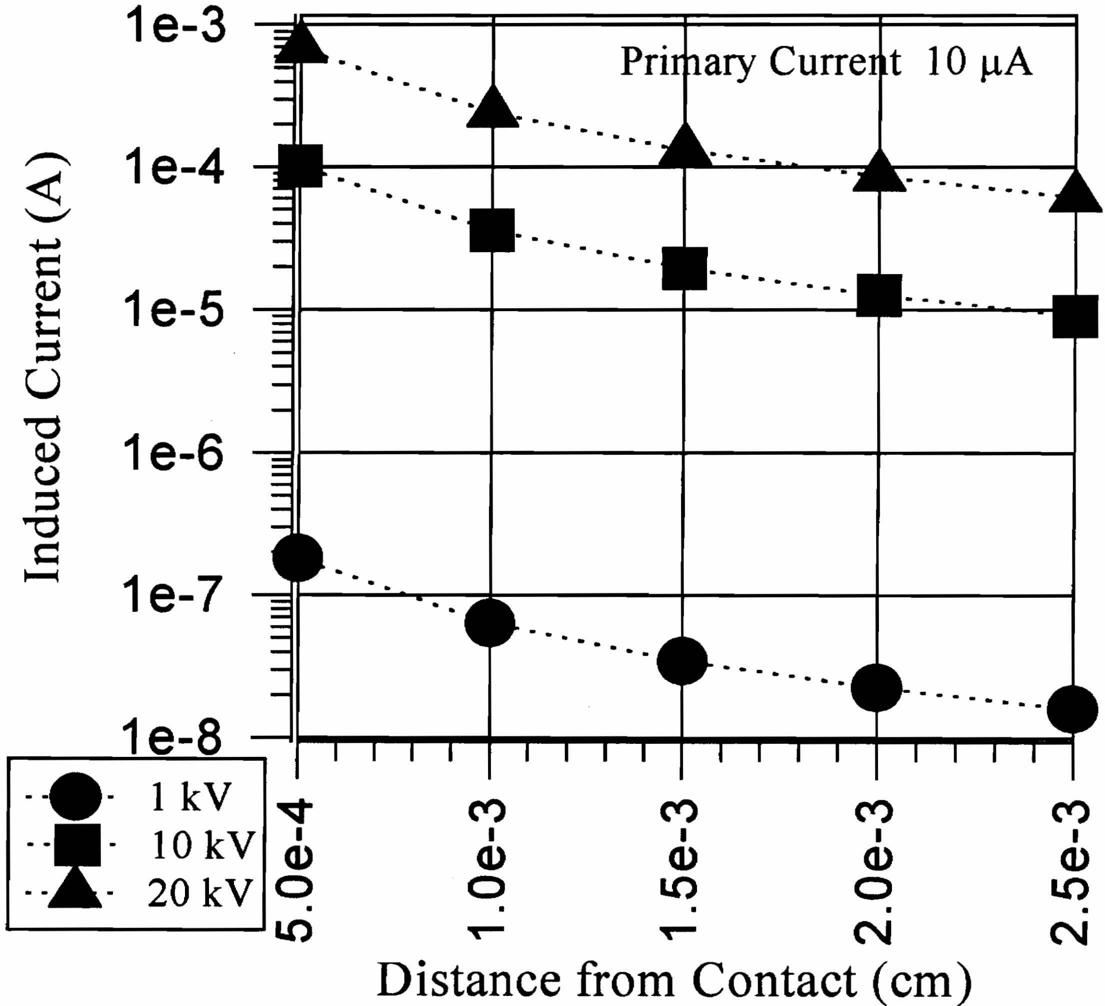

(a) GaN

Figure 2.12. Theoretical Induced Diffusion Currents for 10 μA Primary Current.

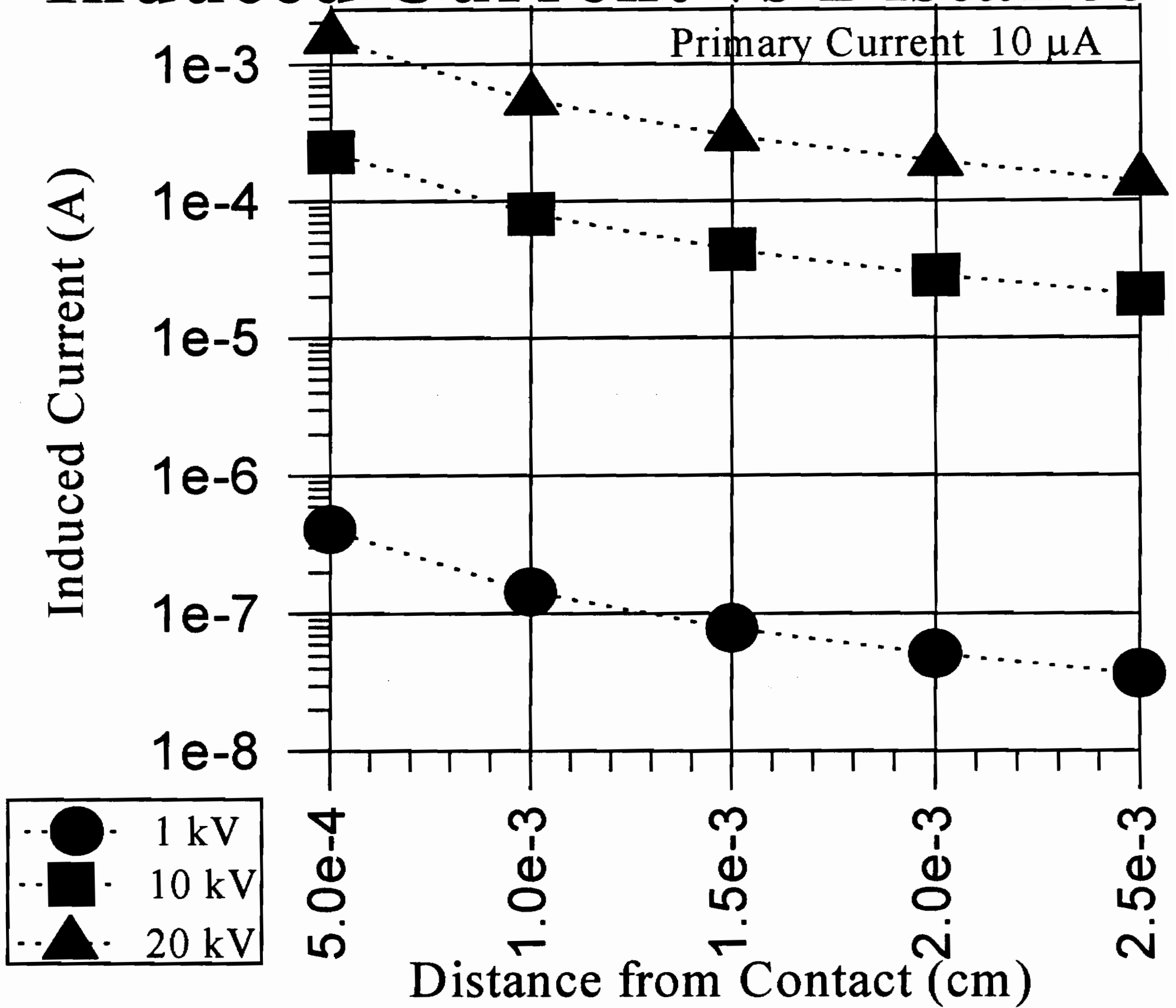

(b) Diamond

Figure 2.12. Theoretical Induced Diffusion Currents for 10 μA Primary Current.

2.3.2 Space Charge Limitations

The main problem encountered during EBIC time of flight transient measurements pertains to space charge effects which are of importance in detecting the transport properties. There are two kinds of space charge effects. The first is connected with the presence of deep trapping centers in the volume and particularly near the surface of the specimen. The gradual build up of charge in such centers during successive transits will modify the internal field, so the assumption of an essentially uniform field is no longer valid. Experimentally, one observes slow polarization effects in which the transit signal gradually diminishes in size during the first few seconds after switching on the excitation pulses. Occasionally the signal disappears completely and in this case the resultant field has become extremely small in part or all the sample. To eliminate disturbing effects of this kind, two precautions are essential: first, the density of generated carriers should be kept as low as is consistent with the sensitivity of the detecting equipment. This can be accomplished by varying the acceleration voltage, thus decreasing the depth of penetration into the sample and in so doing reduces the volume of electron-hole pairs generated. Secondly, space charge neutralization techniques should be used, such as grounding all connections, reducing all noise in the connections and pulsing the sample bias voltage and/or the electron beam.

The second effect is connected with the space charge of the drifting carriers themselves. If N is increased sufficiently the self field, given as:

$$E_{self} = \left(\frac{4 \pi N e}{\varepsilon A} \right) \qquad 2.71$$

can be made to approach the value of the applied field $E_a = V_a/d$. The fields leading and lagging the generated volume of electron-hole pairs will be altered, which would result in a change in the observed signal. For the concentrations used in this research project, the

self fields were significantly small to not disturb the applied field and further consideration can be found in Appendix A. The prominent change in the electron transit signal is the cusp approximately at [(x) T_R] as shown in Figure 2.13.

The physical reason for this pulse shape is: electrons near the leading edge of the generated cloud experience the larger field and "run away" from the slower moving carriers. Therefore, the current will increase until the extraction of the faster carriers' results in a drop beyond the cusp. The position of the cusp (x) in terms of the transit time depends somewhat on the ratio of applied to self field (E_a / E_{self}). If N is kept reasonably constant during the experiment, the cusp forms a useful feature for the accurate measurement of transit time. However, if N is increased, the effective space charge neutralization techniques between excitation pulses become most important and must be applied[46]. This effect can be eliminated by applying a few procedures, the first is to contain the electron beam to a small spot size upon impact with the sample and this can be achieved by the use of apertures, strong magnetic fields in the alignment of the electron beam column. The second is by varying the acceleration voltage, as discussed before, to decrease the number of electron hole pairs generated. Thirdly, by pulsing both the sample and the electron beam, therefore creating a longer time between excitation pulses.

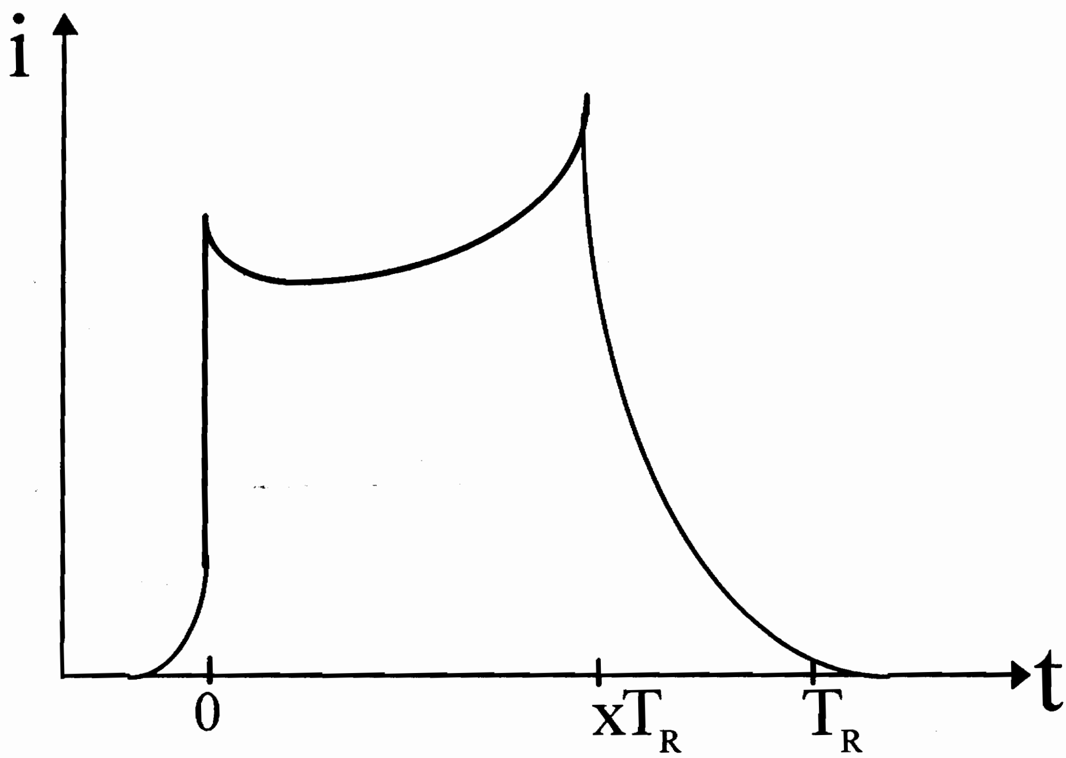

Figure 2.13. Space Charge Effects due to Drifting of the Carriers.

Chapter 3

Scanning Electron Microscope

3.1 Background Information
- 3.1.1 History
- 3.1.2 Operational Overview

3.2 SEM Breakdown
- 3.2.1 Electron Optical System
- 3.2.2 Electron Beam/Specimen Interaction
- 3.2.3 Secondary Electron Detector
- 3.2.4 Vacuum System

3.0 Scanning Electron Microscope

In this chapter, the scanning electron microscope (SEM) is described. The chapter opens with a brief history and overview of the development of the SEM from its origin. This is followed by four sections describing the electron optical system, the electron beam/specimen interaction, the secondary electron detector, and the vacuum system. The electron optical system is designed to control the electron beam from the electron gun to the specimen chamber. The electron beam/specimen interaction explains the reaction of the electron penetration into the material under test (MUT) and the creation of secondary electrons. The section on secondary electron detector describes how the secondary electrons are used to create an image on the monitor. In the last part of this section the types of vacuum systems used in the SEM are discussed.

3.1 Background Information

3.1.1 History

This section provides a brief history and overview of the Scanning Electron Microscope (SEM) from its origin to its present form, before discussing the basics of the SEM. The door was opened for the development of the SEM in 1590 by the Janssens, manufactures of eyeglasses, by the invention of the compound light microscope. Objects were magnified up to 30 times their original size. The next step was the development of the simple lens microscope by Antonie van Leeuwenhoek in the following century. This microscope magnified objects up to 300 times the original size. In 1873 Abbe and Helmholz showed independently that the wavelength of the energy source used provided the resolution limit of an image. De Broglie in 1924 showed that electron properties behaved like waves, and Bush in 1926 demonstrated that electron paths could be deflected by an applied magnetic lens similar to light deflection by optical lens. With magnification

up to 1000 times by the 20th century, observations could be made of 0.2 mm apart spacing. In 1932 Knoll and Ruska developed the first electron microscope in Germany. This microscope took advantage of the much shorter wavelengths of electronics. The magnification from this microscope increased visibility by another thousand fold. By 1935 the resolution of the electron microscope was much superior to that of the light microscope. Metropolitian Vickers, in 1937, developed a prototype of an electron microscope, and in 1938 Van Ardenne constructed the first SEM. After several iterations the first commercial SEM was available in 1963 by RCA Laboratories. By the late 60's the SEM had become standard instrumentation in the electronic industry, where it is often used in assembly line areas to control the quality of microcircuity, as well as, in research and development.

3.1.2 Operational Overview

The SEM provides an image that appears to have three dimensions. The microscope uses a 2 to 3 nm spot of electrons to scan across the surface of the specimen and generate secondary electrons that are detected by a sensor. The secondary electrons are described further in section 3.2.2. The electron wavelength λ_e depends on the electron velocity or the accelerating voltage V

$$\lambda_e = \frac{h}{mv} = \frac{h}{\sqrt{2qmV}} = \frac{12.2}{\sqrt{V}} \ \mathring{A} \qquad 3.1$$

Therefore the resolution of the SEM is much higher than that of the conventional light microscopes because of the high range of voltages used (kV) in accelerating the electrons. The resultant image is produced over time as the electron spot transverse over the entire specimen. However the actual resolution achieved during observation of a specimen is

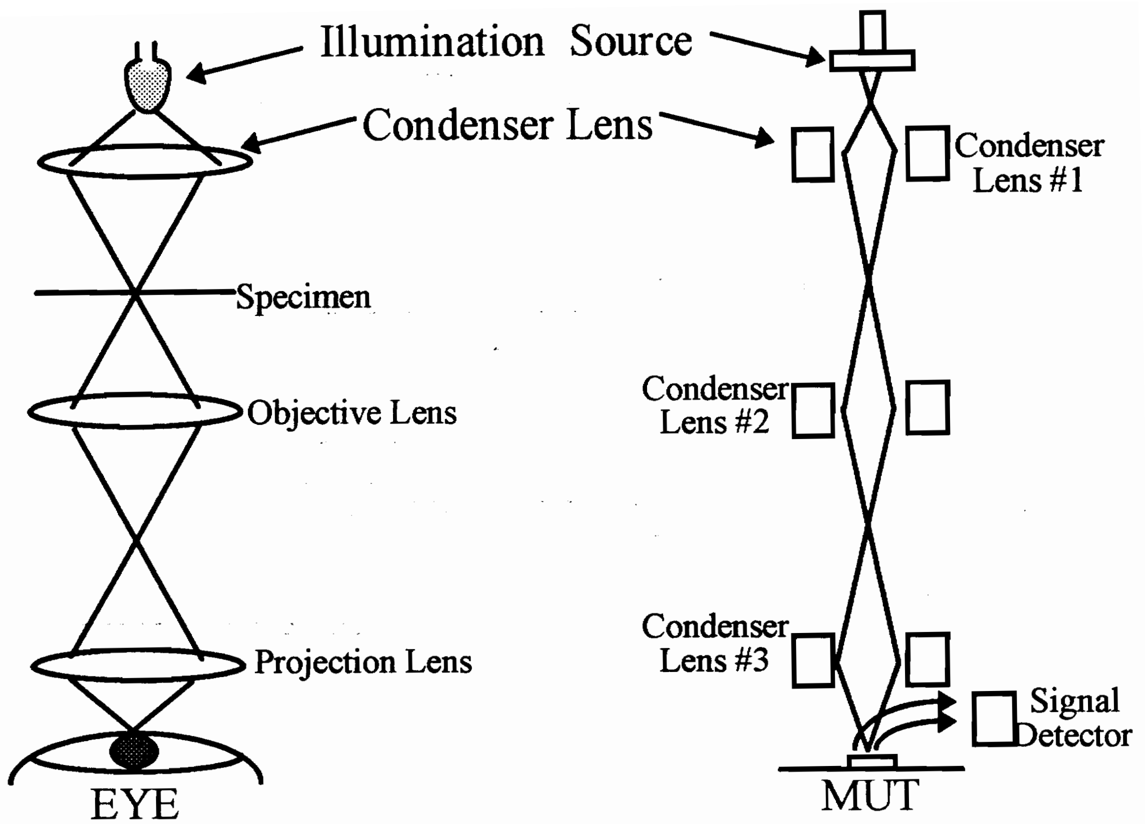

Figure 3.1. Comparison between Light Microscope and SEM.

not as confined as expected because the volume of the electron-hole pair cloud generated may be larger due to dispersion of the electron beam upon interaction with the specimen.

Figure 3.1 shows the comparison between the light microscope and the SEM. In the SEM the electronic condenser lens does not form an image like the conventional light microscopes. The lenses of the SEM are used to provide a demagnified, focused spot of electrons that is scanned over the surface of the material under test (MUT). When the electrons strike the surface of the MUT, low energy (secondary) electrons from the uppermost layers are released. Some of these electrons are collected and converted into pixels that can be seen on the cathode ray tube monitor (Figure 3.2). Wherever an electron strikes the MUT, secondary electrons are generated. For each generated secondary electron produced, a pixel is displayed on the monitor. The number of secondary electrons generated from the MUT is directly proportional to the brightness of the pixels. Since the electron beam is scanned rapidly over the MUT, the result is a blend of continuos-time images composed of many density levels of shades of gray.

As shown in Figure 3.2, the SEM can be subdivided into four areas; the electron optical system, the specimen chamber, the secondary electron detector and the vacuum system. The electron optical system is used to focus and control the electron beam. The specimen chamber is needed to hold the MUT with respect to the electron beam. The secondary electron detector is used to gather the electrons released from the MUT and generate a display on the monitor. The use of the vacuum system is to remove air molecules that may hamper the passage of the high energy electrons down the column, as well as to allow the low energy secondary electrons to reach to the detector.

3.2 SEM Breakdown

This section describes the breakdown of the SEM four most important systems, the electron optical system, the electron beam/specimen interaction, the secondary

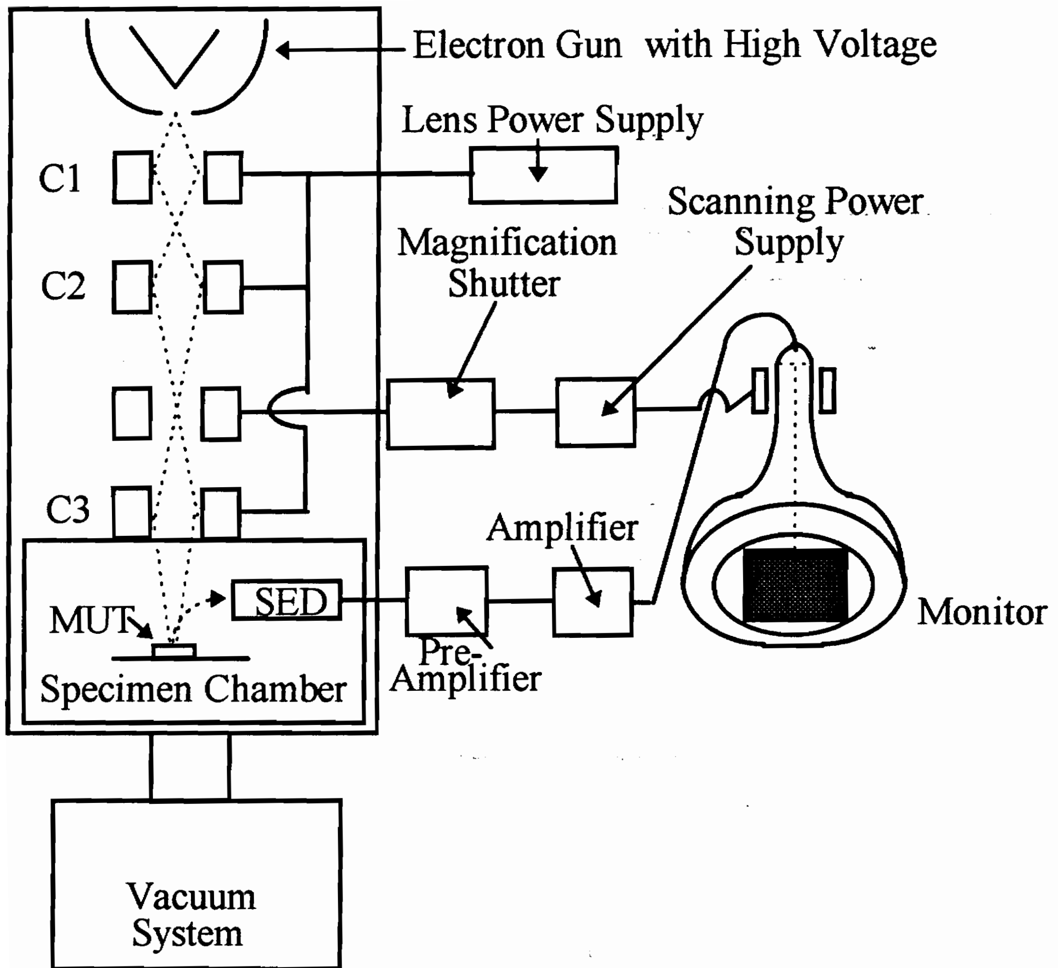

Figure 3.2. SEM Basic Component Configuration.

electron detector and the vacuum system. In each area the key components are discussed in order to give a better understanding of the overall operation of the SEM. The electron optical system describes how an electron beam after generation arrives to the MUT. The electron beam/specimen interaction section describes how the electron upon impact with the specimen, produces secondary electrons for detection. The secondary electron detector section describes how an image is created from the secondary electrons. The final portion of this section talk about the vacuum system used in most SEM.

3.2.1 Electron Optical System

In the electron optical system, the electromagnetic lenses, deflection coils, and stigmators are used to control and refine the electron beam after they leave the electron source and before they reach the MUT. The thermionic source, is made up of a V-shaped tungsten filament that is heated to release electrons. These electrons are accelerated in the direction of the anode due to high negative potential applied to the shield, as shown in Figure 3.3.

After leaving the bias shield, the initial focus spot of the electrons is approximately 50 μm in diameter. The electrons are then demagnified to less than 2 nm by passing through the three condenser lenses. At high magnification, to obtain good resolution, small spot sizes are necessary. The condenser lens (C1) demagnifies the 50 μm focused spot of electrons formed in the electron source.

The focal length of the lens is controlled by the current flowing through C1, an increase in the current results in a decrease in the focal length and the focused spot of the electrons. A shorter focal length in C1 lens creates a wide divergence of the electrons leaving the lens. This increase in divergence leads to some of the electrons being lost before they enter the next condenser lens (C2). Therefore the overall effect of increasing the strength of C1 is to decrease the spot size, but with a loss of beam electrons. The

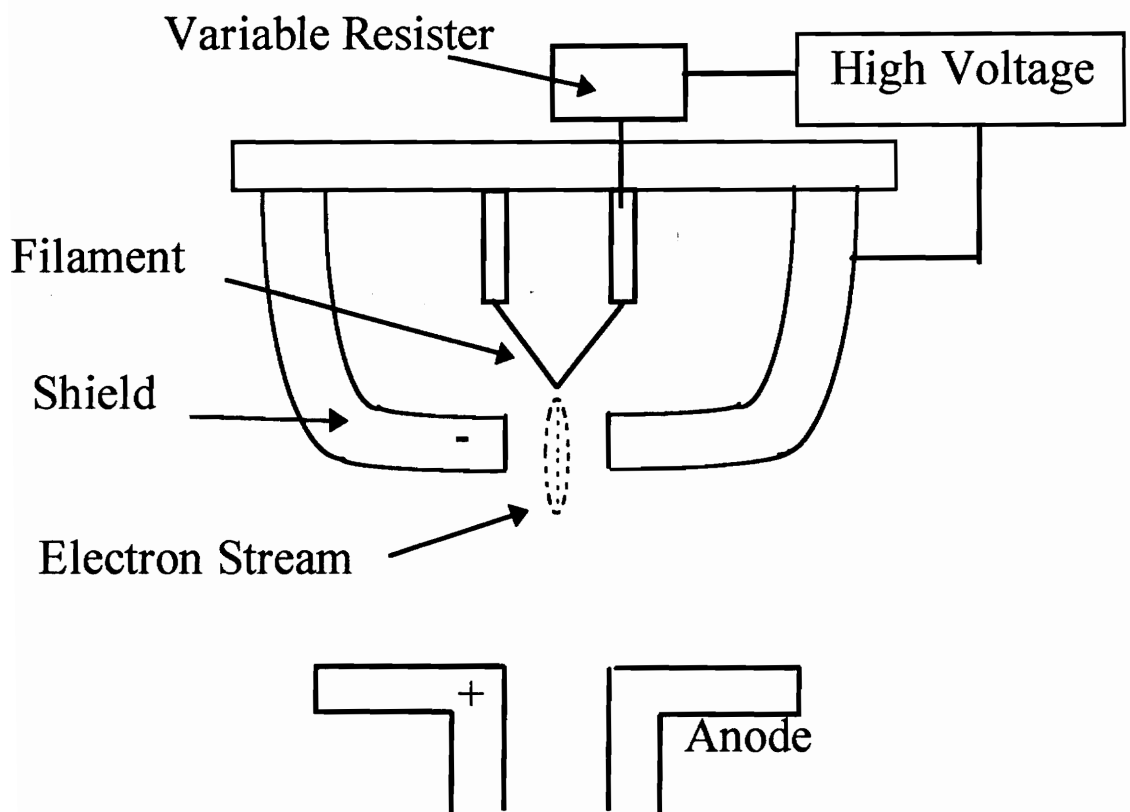

Figure 3.3. Anode/Cathode Configuration of the Thermionic Source.

result is an improvement in resolution, but the overall signal (number of secondary electrons) coming from the MUT is reduced. This reduction is due to fewer beam electrons hitting the MUT. Apertures are placed in the lenses to help prevent spherical aberration and reduce the spot size by eliminating the more peripheral electrons. All the other condenser lenses behave the same and enclose apertures.

The final condenser lens(C3) is the strongest of all the lenses and performs the task of final demagnification of the electron spot. This C3 is used mainly to adjust the spot size without a loss of beam electrons, and therefore gives the focus of the image seen on the monitor. This condenser lens is made up of deflection coils and stigmator. The deflection coils are connected to the scan generator to raster the electron spot across the MUT. In the raster mode the spot is moved in a straight line across and down the MUT. The resulting magnification can be varied by changing the length of the beam scanning over the MUT and is given by:

$$\text{Magnification} = \frac{\text{Length Displayed on Screen}}{\text{Length Scanned on Sample}} \qquad 3.2$$

The stigmator is used to control any distortions in the roundness of the spot formed by the electron beam as it moves over the MUT. They consist of 6 to 8 small electromagnetic coils inside the lens bore of C3. If the beam spot is not round, the image will appear on the monitor smeared in one direction or astigmated. The major cause of astigmatism is aperture contamination. Stigmators, however correct for this distortion by applying the appropriate electromagnetic field to compensate. The C3 usually has externally adjustable apertures in varied sizes. The apertures range from 50 to 600 μm, where the smaller apertures are used to generate smaller, less energetic spots for secondary electron generation and better imaging. The larger apertures are used to generate larger spots with greater numbers of electrons, which results in more energy, and are used primarily in elemental analysis.

Apertures in C3 also affect the depth of field and help diminish spherical aberration. The depth of field is given by:

$$D_{fi} = \frac{\lambda}{NA^2} \qquad 3.3$$

where λ is the wavelength of the illumination and NA is the numerical aperture. The depth of field refers to the depth in the MUT that appears to be focus. Depth of field is also affected by the working distance, (distance the MUT is situated from C3) it increases as working distance increases. However, increasing the working distance leads to a decrease in resolution. The resolution is the ability of the SEM to image two closely placed objects as two entities rather than one object. The better the resolution the smaller the beam spot size and the higher the electron energy. The maximum allowable spot size is given by[47]:

$$\text{Max.Spot Size} = \frac{100\mu\,\text{m}}{\text{Magnification}} \qquad 3.4$$

If the beam spot size is greater than the maximum spot size, then the secondary electrons will be generated from a region outside that shown on the monitor. This would result in an un-sharp image, because extraneous information would be present in the display spot. The final lens may be used to decrease the beam spot size and thus focus the image. If a satisfactory focus cannot be achieved by the final lens, then increasing the strength of the other condenser lenses will result in a reduced spot size.

Therefore smaller apertures not only give better resolutions because of decreased spherical aberration and spot size, but they also increase the depth of field. Unfortunately these gains are at the expense of a reduced signal coming from the MUT, since fewer electrons are present in the impinging beam. The relationship between aperture size and image quality can be seen in Table 3.1.

Table 3.1

Aperture Dimension	Resolution	Depth of Field	Signal Strength
30 (mm)	Best	Deep	Weak
200 (mm)	↓	↓	↓
400 (mm)			
600 (mm)	Worst	Shallow	Strong

3.2.2 Electron Beam/Specimen Interaction

When an electron with acceleration energy of 1 kV to 25 kV strikes the MUT, they create a number of emanations. Depending on the speed of the electrons, as well as, the density of the MUT, the electron beam may penetrate to variable depth into the MUT. The initial point of entry may be at a 2 nm diameter spot; however upon impact the electrons scatter randomly throughout the MUT until their energy is dissipated by interaction with atoms. The electrons lose energy by elastic scattering (change of direction with little or no loss of energy) and inelastic scattering (little or no change in direction with energy loss).

In the case of elastic scattering, the electrons interact with nuclei of atoms in the MUT. This is more probable in high atomic number materials, especially at low beam energies. Inelastic scattering is caused mainly by scattering due to interaction with the valence and core electrons. The results of these scattering events are a broadening of the electron beam within the MUT. The resulting generated volume is a function of the electron beam energy and the atomic number (Z) of the MUT. Secondary electrons, backscattered electrons, electron-hole pairs, Auger electrons, characteristic and continuum X-rays, and photons of various energies are produced.

For low Z materials most of the electron beam penetrates deeply into the material and is absorbed. For high Z materials there is considerable scattering near the surface,

leading to a large volume of backscattered electrons. The shape of the electron distribution within the MUT depends on the atomic number. For Z equal to or less than 15 the distribution takes the form of a teardrop, as shown in Figure 3.4. For values of Z between 15 and 40 the shape becomes more spherical, and for Z greater than 40 the shape is hemispherical, as observed by Everhart[48].

The depth of electron penetration (R_e) defines the average total distance the electron travels from the surface along a trajectory and can be expressed as equation 2.62 or as:

$$R_e = \frac{4.28x10^{-6} E^{1.75}}{\rho} \text{cm} \qquad 3.5$$

where ρ is the sample density (g/cm^3) and E is the electron energy (keV). This equation is sufficiently accurate for the 5 keV < E < 200 keV range, which is the standard range of operation in SEMs. A more accurate expression is provided by Everhart and Hoff[35].

For the case where the electron changes direction without losing velocity or energies (elastic scattering), and because the electron either collides with or passes close to the nucleus of an atom, the result is a release of backscattered electrons. These high energy electrons may interact with an atom in the MUT before exiting and so doing generate secondary electrons some distance away from the initial point of entry. Also, if the backscattered electrons strike the sides of the specimen chamber, they can produce extraneous secondary electrons that are summed with the secondary electrons from the MUT to produce noise and a final image, as shown in Figure 3.5.

The true signal in Figure 3.5 is represented by SE1 and SE2. They are the secondary electrons that originate some distance away from the focused spot. The SE2 signal represents spreading of the beam as it interacts with the MUT. BS1 and BS2 are the backscattered electrons striking the SEM and producing noise in the form of SE3.

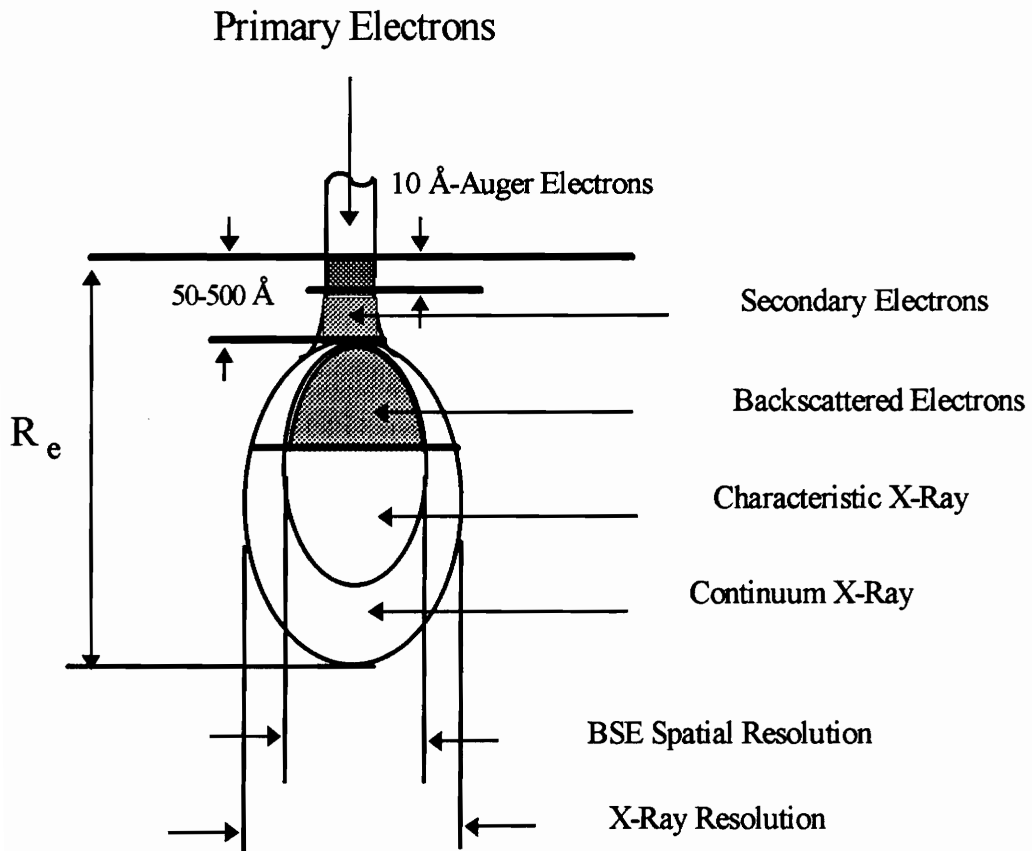

Figure 3.4. Volume created from Interaction of Electron Beam and Specimen.

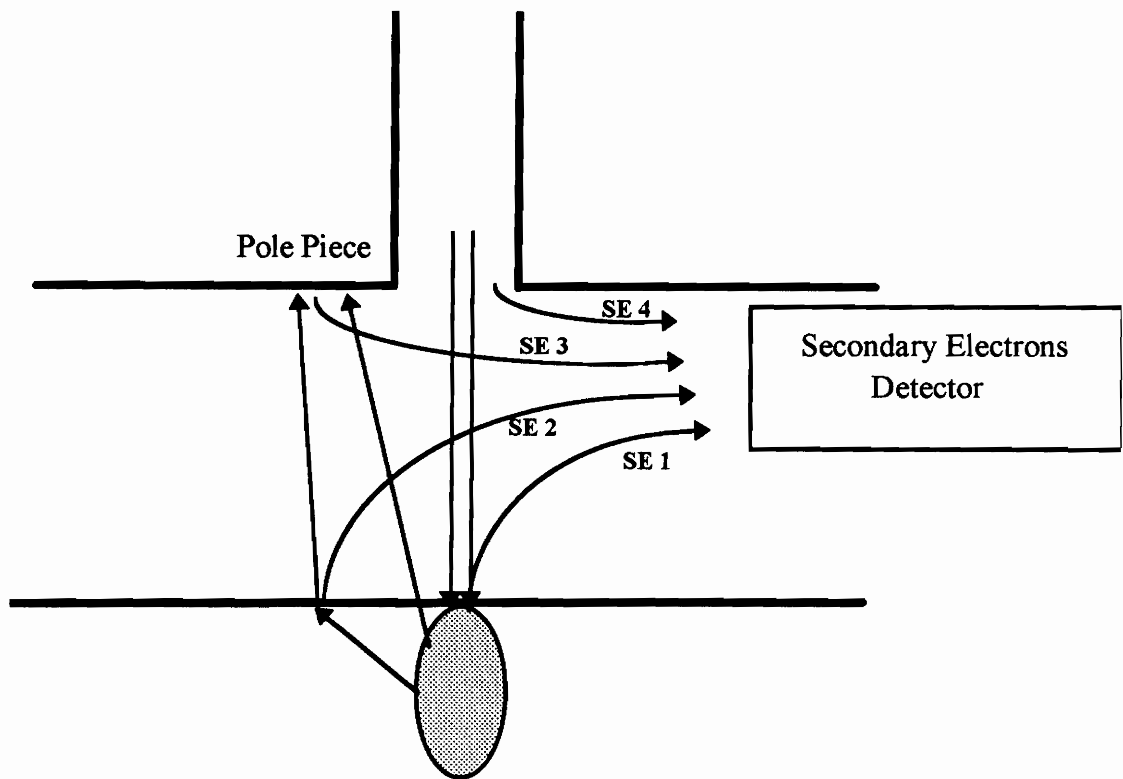

Figure 3.5. Generation of Secondary Electrons.

SE4 is due to secondary electrons generated by the primary beam interacting with part of the SEM lenses and results in noise in the detected signal.

For the inelastic scattering case, where some of the electrons interact with the atoms of the MUT, low energy secondary electrons can also be produced. These secondary electrons have energy ranges of 0 to 50 eV leading to an assist of the three-dimensional images seen on the monitor. Occasionally, tightly bound, inner shell electrons will interact with the electron beam. This will effect the ejection of the inner shell electrons by ionizing the atom until the outer orbital electrons fill the inner void. The resulting energy is dissipated as characteristic X-rays and Auger electron, which are detected by specialized X-ray or electron spectrometers.

3.2.3 Secondary Electron Detector

The low energy secondary electrons leave the MUT from many different angles. These secondary electrons are attracted to the positive Secondary Electron Detector (SED) because they are weakly negative and the SED contains a Faraday Cup maintain at -100 to 300 Volts. Once the electrons arrive at the cage, they are attracted by a much stronger detector at the end. This detector is thinly coated usually with aluminum and maintained at 12 kVolts. The electrons, on impact with the aluminum, penetrate through and strike a phosphorescent material giving off a short bust if light. This light then collides with a photocathode on the end of a photomultiplier, generating electrons. The photoelectrons enter the photomultiplier and travels through a series of electrodes that increases the number of electrons (Figure 3.6).

The secondary electron yield can be increased by increasing the electrode voltage, leading to higher gain. On the SEM front panel, adjustments to the gain or contrast leads to changes in the gain of the photomultiplier and increasing the contrast of the image is the same as increasing the photomultiplier gain. The highlights are increased more than the

shadow areas leading to an increase in brightness of the lighter areas over the darker areas. The small levels of voltage generated by the photomultiplier is amplified by the pre-amplifier/amplifier component of the SEM. When the pre-amplifier output is increase, the overall brightness of the image is increased.

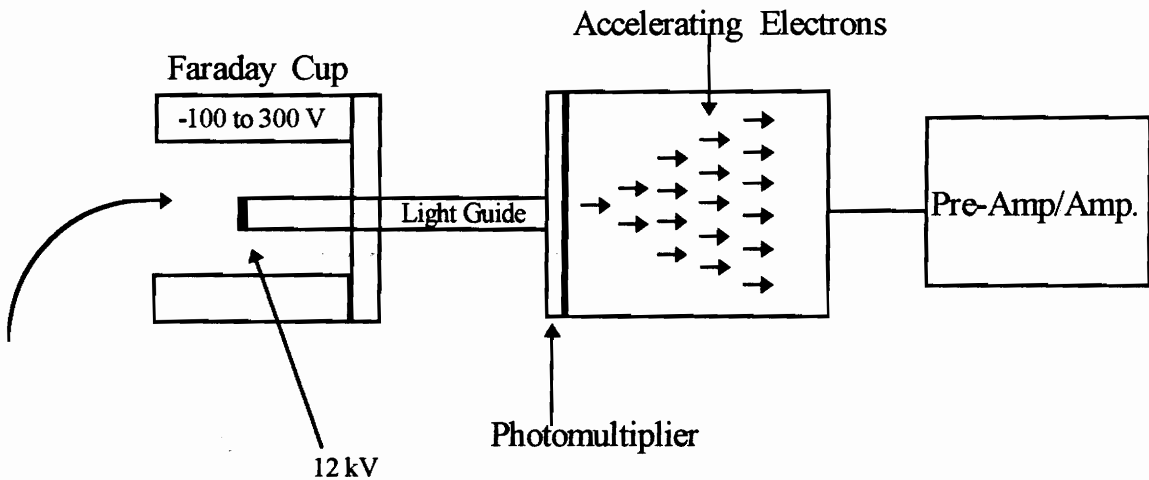

Figure 3.6. Secondary Electron Detector.

3.2.4 Vacuum System

The vacuum system is an assembly of pumps, switches, and valves that are involved in evacuating air primarily from the pathway of the electron beam, but also from other selective areas of the SEM. It is though of as a plumbing system designed to connect the vacuum pumps to the SEM selective areas. Their are three main reasons that a vacuum is needed in the SEM; One is to increase the mean free path of an electron or the distance an electron must travel without encountering an interfering gas molecule. The second reason is to prevent high voltage discharge between the filament/shield and

anode. Discharges of this kind usually results in damage to the filament. Also, all filaments are extremely sensitive to oxidation and must be protected. The third reason is to remove contaminating gases, especially water vapor and organisms present in laboratories, that are broken down under high energy electron bombardment. For they can result in the generation of corrosive radicals that combine with the MUT and destroy the structure.

The majority of the SEMs obtain vacuum conditions by using a two pump system, a rotary pump followed by a diffusion pump. The rotary pump usually operates first to reduced the pressure to the 10^0 to 10^{-1} Pa range (1 Pa = 7.52 x 10^{-3} Torr) and the diffusion pump is incorporated to increase the vacuum further to the 10^{-3} to 10^{-4} Pa range. Figure 3.7 shows the vacuum system of a typical SEM, where V1-3 are valves, LV1 is the air admittance valve, and IG is the ionization gage.

The rotary or roughing pump used a rotating cylinder, with sliding spring-mounted vanes, mounted off center inside a larger cylindrical space. As the rotor turns clockwise from position A to B, an enlarged space is created with lowered pressure that draws air into B. As the rotor continues turning, space B is sealed off and becomes smaller as the rotor moves the gas into space C. Space C gas is compressed to the extent that the spring loaded valve is forced open and the gas leaves the system.

Diffusion pumps however, contain no moving parts but are still able to complete the pumping started by the rotary pump. The diffusion pump is made up of a series of stacked towers with highly polished umbrella-like caps. The towers are enclosed within a water cooled cylinder that is connected to the electron microscope at one end. Oils in the bottom housing are boiled and pressurized vapor is forced up the towers. They are then deflected downward by the multistage jet assembly. In this process the oil molecules are traveling at supersonic speeds, so any air molecules that have diffused into the pump will be taken to the bottom of the chamber. At the bottom of the chamber the air particles will

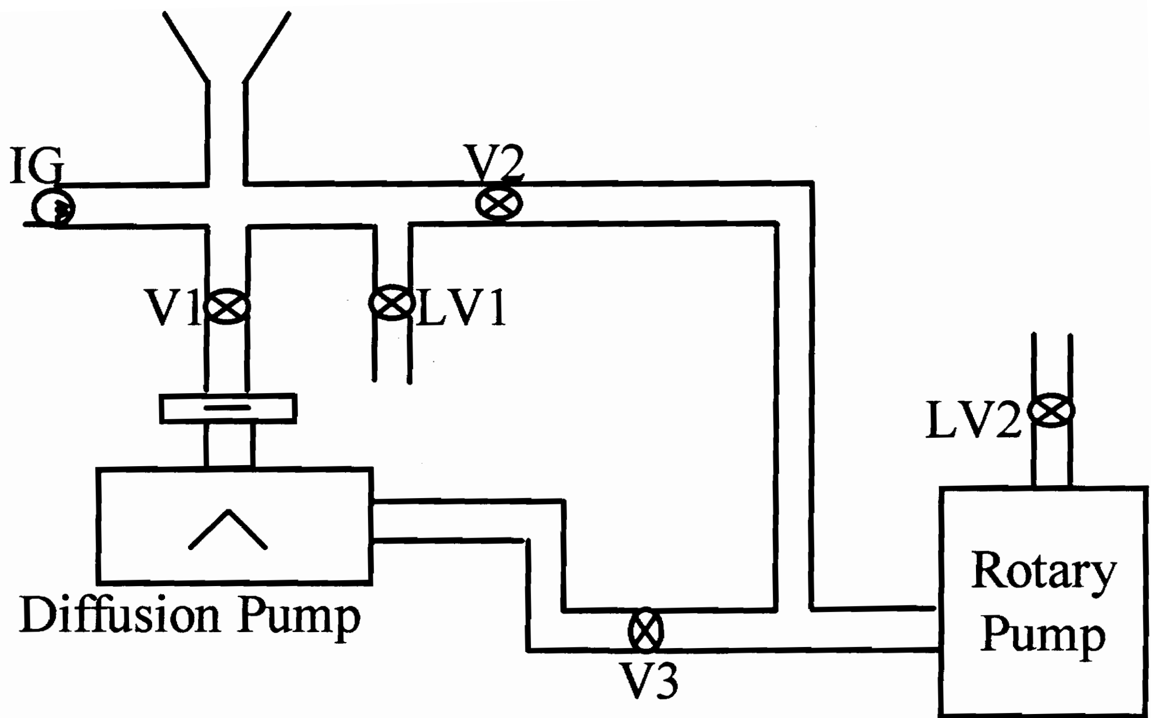

Figure 3.7. Vacuum System of SEM.

be removed by the suction of the connected rotary pump. The hot oil vapors that strike the sides of the pump housing, condense on the water-cooled surface. The oil then flows back to the bottom of the pump where the cycle is repeated. The number of umbrellas in the multistage jet assembly determines the number of stages in the diffusion pump, with each stage capable of lowering the pressure by nearly one Pascal. In a typical three-stage diffusion pump where the vacuum system had previously been roughed to 10^{-1} Pa, the final vacuum would be in the 10^{-4} Pa range.

Chapter 4

Experimental Preparation

4.1 Component Development
- 4.1.1 Faraday Cup
- 4.1.2 Test Fixtures
- 4.1.3 Photocathodes

4.2 Material Preparation
- 4.2.1 Silicon Samples
- 4.2.2 Gallium Arsenide Samples
- 4.2.3 Diamond & Gallium Nitride Samples

4.3 Spot Size
- 4.3.1 Electron Beam Spot Size
- 4.3.2 Optical Beam Spot Size

4.0 Experimental preparation

Before the experiment could be performed, certain components and materials had to be prepared. These components were the Faraday Cup, test fixtures and the photocathodes. The Faraday Cup was needed to measure the incident electron beam current onto the material under test (MUT). This required the development of a component capable of trapping the electrons energy within, without interfering with the MUT. The resultant component developed was a Faraday Cup. The characterization of the OBIC and EBIC systems required the construction of test fixtures. These test fixtures were built to hold the MUT in place during testing. For the L-EBIC system, the development of the photoemission source required the fabrication of photocathodes. These photocathodes provided the electron beam for the L-EBIC system.

Another factor considered before the experiments could begin was the preparation of the samples. Contacts had to be made to the samples and then assembly into various designed test fixtures. Also, before the materials could be probed, the spot size of both the electron beam and the optical beam needed to be found. This was accomplished by the use of the knife edge experiment.

This chapter is divided into three parts. The first part deals with the component development. The Faraday Cup, test fixtures and photocathodes are discussed in this section. The second area deals with the material preparation. The section discusses what materials and devices are used to characterize the different systems. The last area of the chapter discus the spot size analysis used to determine the electron and optical beam spot sizes.

4.1 Component development

4.1.1 Faraday Cup

In order to measure the incident electron beam current, a faraday cup was designed and built to entrap all the electron energy. The purpose of the faraday cup was to monitor the electron energy at all times in the specimen chamber of the scanning electron microscope (SEM). An ordinary SEM specimen stub, 15 mm in diameter, was transformed into the faraday cup (Figure 4.1). The stub surface was drilled with a 5 mm (dia.) hole and then covered with a 6 mm (dia.) disk. The disk had a 1 mm hole in the center where the incident electron beam would enter. A marker was also placed onto the surface of the stub to help identify the location of the faraday cup.

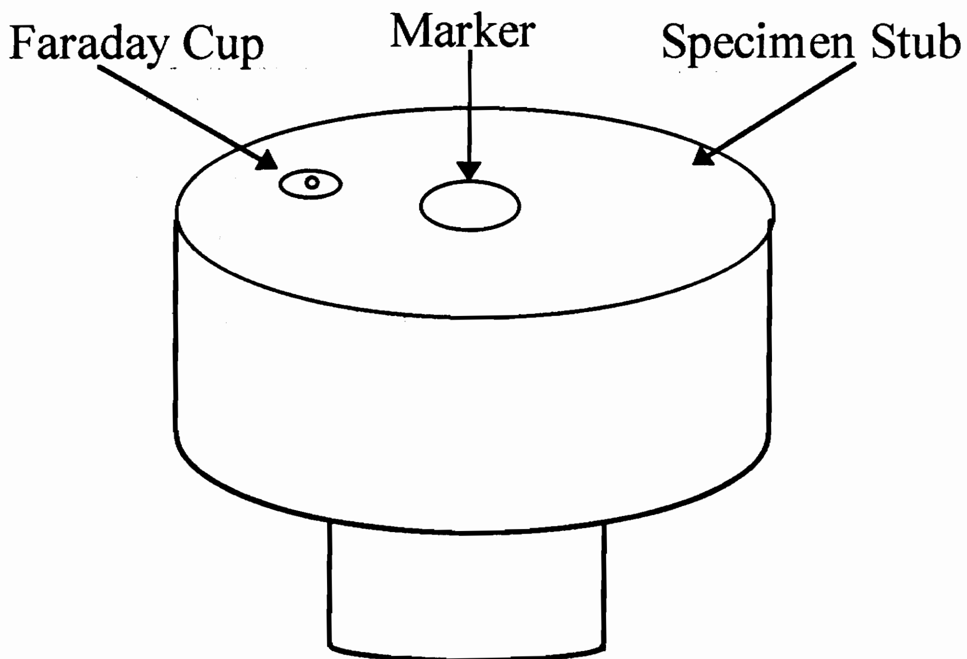

Figure 4.1. Faraday Cup.

4.1.2 Test Fixtures

Due to the different experiments that were performed in this project(OBIC and EBIC), the characterization of the different experimental procedures required the use of known materials such as Silicon (Si) and Gallium Arsenide (GaAs) to calibrate the systems. These materials required the fabrication of special test fixtures. Figure 4.2 shows the test fixture used for the OBIC experiments. Here, the samples could be placed in either of two configurations vertically or horizontally. Both configurations could be obtain from the same test fixture, by tilting the XYZ-translation. The test fixture and the lens were placed on the same horizontal rail for easier alignment. The probe tip, with its XYZ-translation was also connected to the sample stage. The separate probe tip XYZ-translation gave an added advantage for aligning to the sample after the optical beam was at the appropriate location.

The test fixture for the EBIC experiments can be seen in Figure 4.3. In this case there is no probe tip, because both sides of the sample are in direct contact with the SMA connectors. This fixture eliminated most of the problems of noise associated with the contacting probe found in the OBIC system. The EBIC test fixture was made in two configurations, vertical and horizontal. Because the test fixtures had to fit inside the specimen chamber with the faraday cup, they were made quite rigid and small.

For the diamond and GaN samples no separate test fixture was needed because they were assembled and bonded to pins on arrival. Coaxial-cables were used to connect pins from the carrier to the modified SEM and then to the high speed sampling oscilloscope. Figure 4.4 shows the configuration used in the experiments. The carriers were held in place in the specimen chamber of the SEM by cables ties next to the faraday cup. In this setup both the MUT and the faraday can be probed at the same time by moving the translations connected to the specimen chamber.

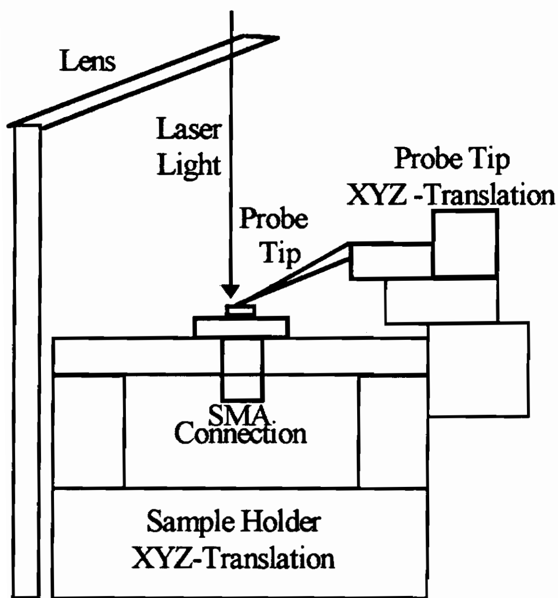

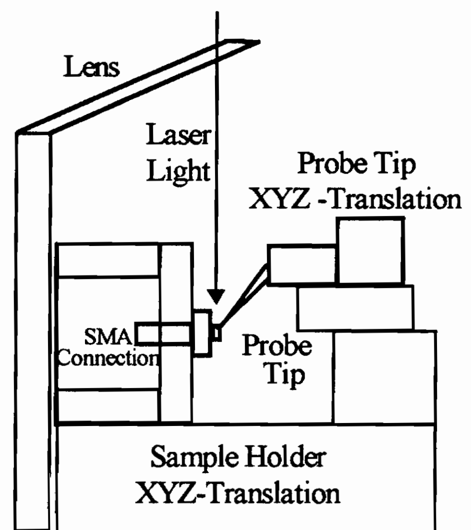

Figure 4.2. Test Fixture for OBIC Experiments.

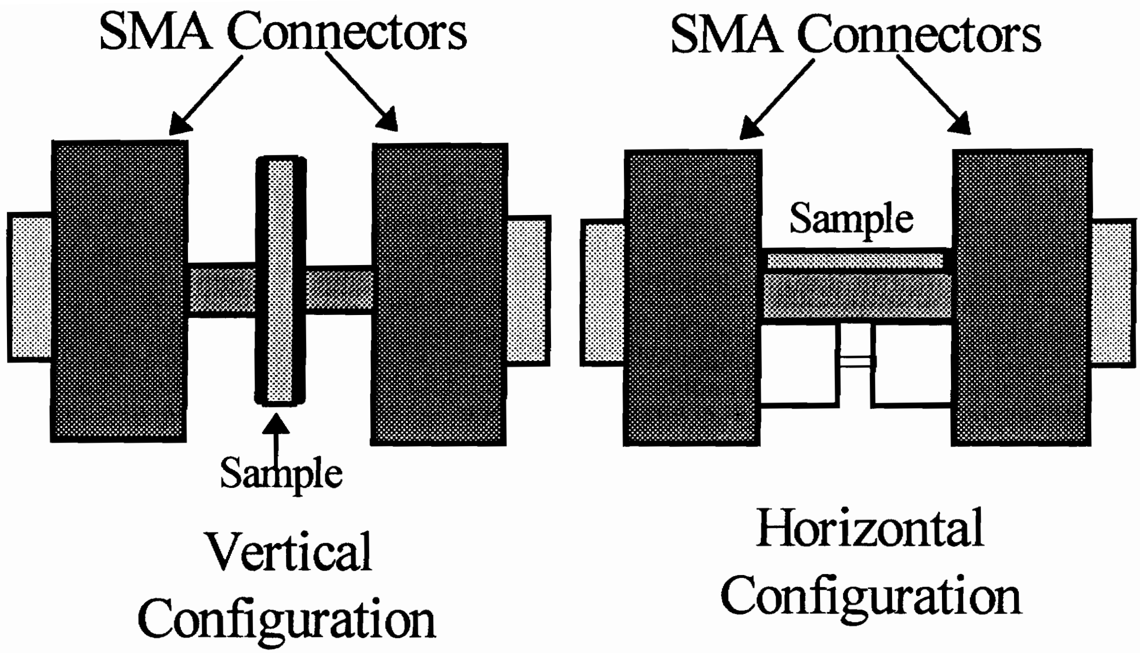

Figure 4.3. Test Fixture for EBIC Experiments.

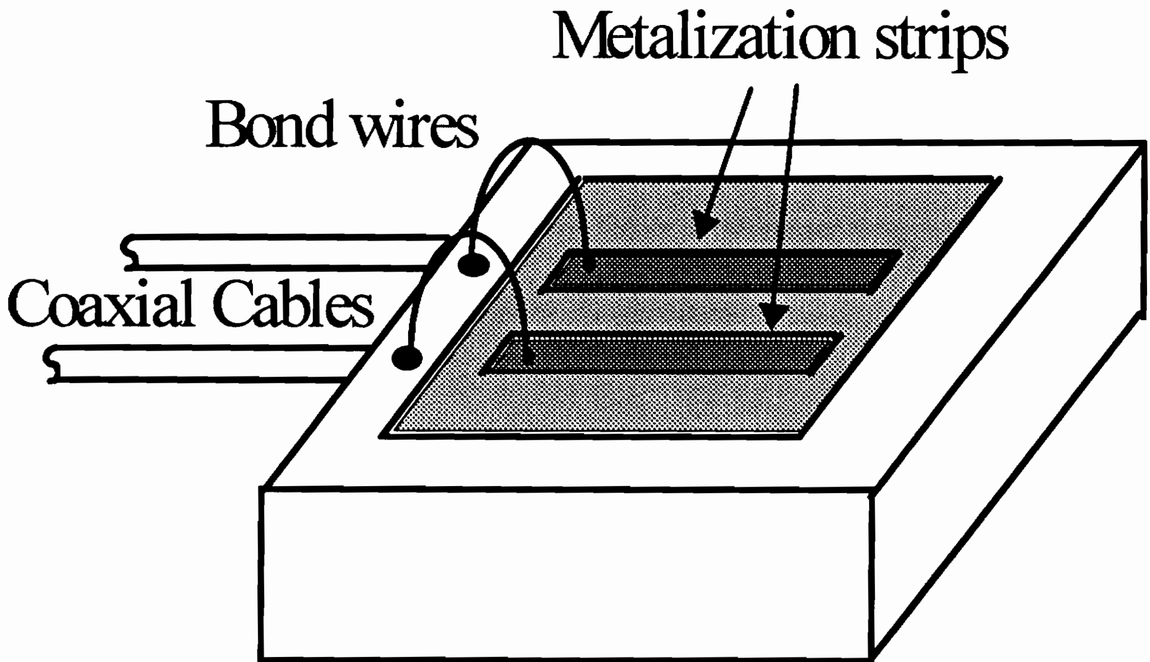

Figure 4.4. Diamond & GaN test Fixture.

4.1.3 Photocathodes

The unique aspect of the L-EBIC system was the incorporation of the photoemission based cathode into the modified SEM. The photocathode worked similar to the conventional thermionic emission cathodes except photons were used to excite electron emission. The photocathode was made from one inch diameter quartz plates, some roughed on the back, with metal deposited on the front. The photocathode was placed face down into the vacuum of the SEM and its back exposed to the focused ultraviolet light from the laser. Photons enter the photocathode and interact with the metal substrate interface producing free electrons inside the SEM. Details of the photocathode electron gun can be found in paper by Scott[(20)]. It was believed that photoemission current in the tens of nA would be adequate to be resolved with the measurement system being used[(20)].

Three types of metallization on the photocathodes were used in this experiment, in hopes of achieving the photoemission current in excess of 50 nA (limit achieved by Scott[(20)]). These photocathodes were: gold (Au), lanthanum Boride (Lab_6) and calcium fluoride (CaF_2). These three materials were found to be most suited for photocathode application[(20)] because of their low work functions (4.9 eV for Au, 2.6 eV for Lab_6 and 4.5 eV for CaF_2) which was necessary to maintain high emission current for ultraviolet wavelengths and high tolerance to vacuum contaminants. The tolerance to vacuum contaminants, such as hydrocarbons from residual gases, was achieved by using a multilayer configuration. This multilayer configuration was either Lab_6\Au or CaF_2\Au combination. The final metallization layer of Au was used because of its high resistance to oxidation and surface contamination, while the Lab_6 and CaF_2 ceramics were used for their high photoelectron generation rates[(49)]. In the multilayer configuration photocathode, majority of the photoelectrons were believed to be generated in the Lab_6 or CaF_2 layer and the remainder generated in the Au layer.

The one dimensional solution to Poisson's equation leads to the current voltage characteristics for the photocathode[20]:

$$\frac{d^2V}{dx^2} = -\frac{\rho(x)}{\varepsilon_o} \qquad 4.1$$

where V is the potential, ρ(x) is the spatially dependent charge density, ε is the permittivity and x is the spatial variable. Scott predicts the solution for three regions:

saturation region:

$$J_c = J_e \qquad \frac{dV}{dx} > 0, \qquad 4.2$$

exponential region:

$$J_c = J_e \exp\left(\frac{eV_a}{KT}\right) \qquad \frac{dV}{dx} < 0 \qquad 4.3$$

and space charge limited region:

$$J_c = \left\{\frac{4}{9}\varepsilon_o\left(\sqrt{2e/m}\right)\left[(V_a)^{3/2}/d^2\right]\right\} \qquad \frac{dV}{dx} = 0 \qquad 4.4$$

where J_c is the collected current density, J_e is the emitted current density, and V_a is the applied potential.

The photocathodes' metallizations were processed in three groups. Some of the quartz substrates were first roughened with 600 grid sandpaper in hopes of reducing reflection losses. The first group was made of Au thermally evaporated onto quartz of various thicknesses, starting from 180 Å. Other photocathodes were first deposited with

LaB_6 (group two) or with CaF_2 (group three) by electron beam evaporation and then thermally evaporated with Au. The thickness of metallization deposited for this group of photocathodes started from 180/180 Å.

The photocathodes were tested for their current response in an anode/cathode configuration. A negative voltage was applied to the photocathode and an ammeter connected to the anode as shown in Figure 4.5. The adjustable spacing between the anode and cathode was first set to 15 mm. The voltage was varied from 0 Volts to -100 Volts and the ammeter recorded the photoemission current. Factors affecting the photocathode current were: incident ultraviolet power, distance of separation between the anode and cathode, the focal distance of the lens to the cathode, the thickness/type of the metallization on the substrates, the acceleration voltage applied to the cathode, and if the quartz substrate was roughened or not.

The results of the photocathode test showed that an increase in ultraviolet power leads to an increase in photoemissiom current as shown in Figure 4.6. Also observed was the relationship between wavelength and photoemission current, as the wavelength increased the photoemission current decreased (Figure 4.7). This showed that as the wavelength moved away from the minimum energy needed for an electron to escape from the surface of the Au (work function of Au), the single photon emission process was replaced by photon-impact hot electrons, and electrons generated by multiphoton emission near the Au/vacuum interface. These results are quit similar to those found by Scott.

For an anode/cathode spacing of 15 mm and lens to cathode spacing of 7.5 mm on a roughened quartz cathode, gold nuggets that had 3 % antimony were used. These settings were used on samples # 1 & 3 and the results can be seen in Table 4.1. After decreasing the anode/cathode distance to 4 mm with 2 mW power, the photocathodes (samples # 4 & 5) were tested again and the results can be seen in Table 4.1. By varying the metallization thickness of gold from 180 Å to 355 Å with intermediate thickness at 263 Å and 300Å, the resultant photoemission current increased from 2.0 nA to 2.4 nA and then decreased to 1.37 nA. This indicated that optimum thickness of gold required to

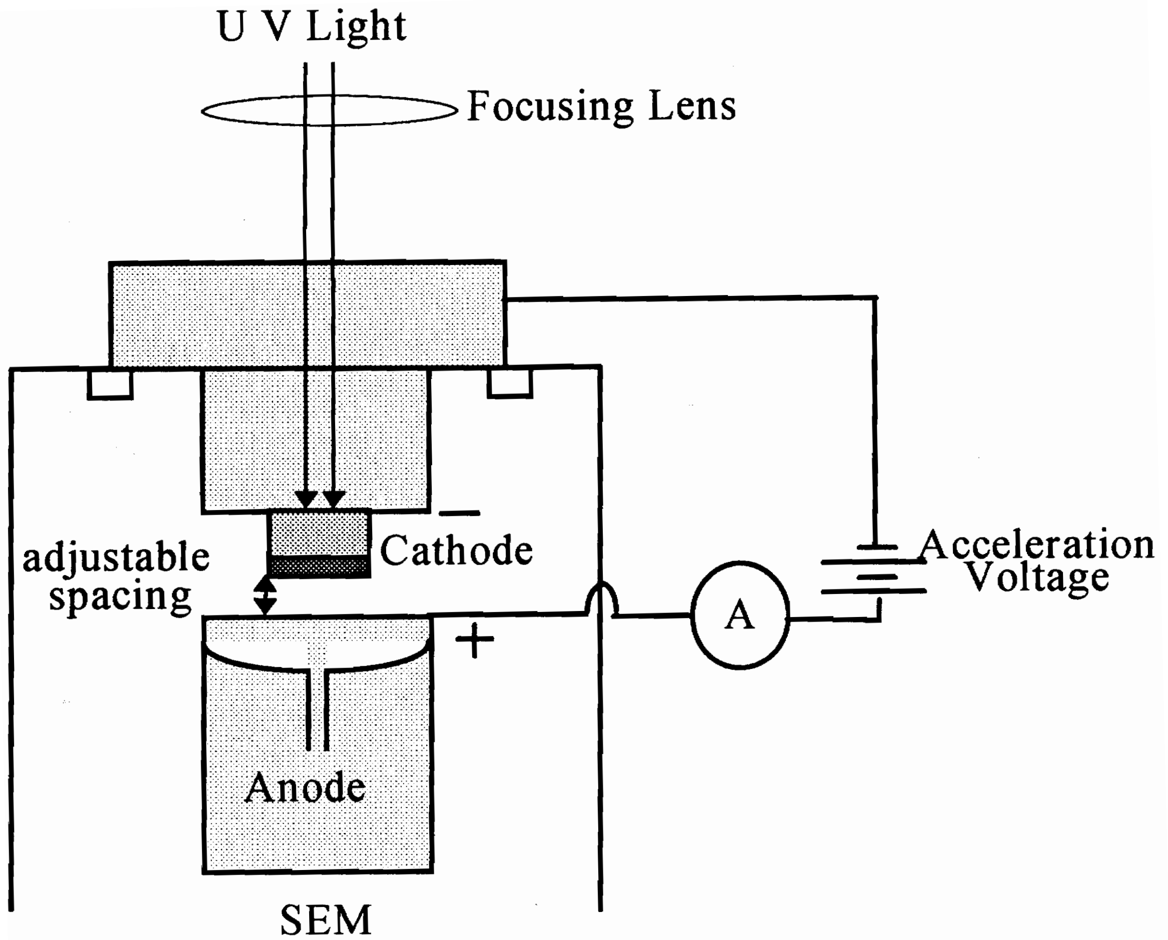

Figure 4.5. Photocathode Test Setup.

generate electrons due to the absorption of ultraviolet light was between 180 Å and 300 Å. The 263 Å photocathode gave a current of 2.4 nA with a lifetime of up to 4 hrs. Here, there was only a 7 % drop off. Consequently the next generation of photocathodes were grown with Au metallization between 180 Å and 263 Å. Figure 4.8 and 4.9 shows the photoemission current for the 355 Å gold photocathode and the 400/250 Å CaF_2\Au photocathode. The ultraviolet power for the 355 Å gold photocathode was 1.4 mW, 0.4 mW and 0.35 mW and for the 400/250 Å CaF_2\Au photocathode it was 1.4 mW, 1.2 mW and 0.8 mW. From these figures, the three regions of the photoemission current can clearly be seen. The space charge region was located on the positive portion of the curve, followed by the exponential and saturation regions.

The roughing material was changed because of the uneven surface of the quartz produced by the 600 grid sandpaper. In its place, 50 μm grit size silicon carbide was used. Along with the new roughened quartz, the ultraviolet power was increased to over 3 mW by re-tuning the harmonic generator, and pure gold nuggets were used. These changes were made in hopes of increasing the photoemission current. The results for the group three photocathodes (CaF_2\Au) were almost ten fold over all other photocathodes, giving photoemission current of 18.8 nA. This was also confirmed by measuring the internal surface resistance of the best of the three groups of photocathodes. The results can be seen in Table 4.2. The 400/250 Å CaF_2\Au photocathode was used for the photoemission current versus wavelength study since it demonstrated the lowest internal surface resistance of all the photocathodes. The results of the study is visible in Figure 4.7.

Before further testing was performed, the setup was closely examined in the hope of improving the performance of the photocathodes. The efficiency of the quartz substrates to ultraviolet light was found to be 87.88 % transmission without roughen and this efficiency drop to less that 50 % when roughened. Improvements in the coupling efficiency of the harmonic generator from 0.1 % to 2 % lead to an increase in ultraviolet

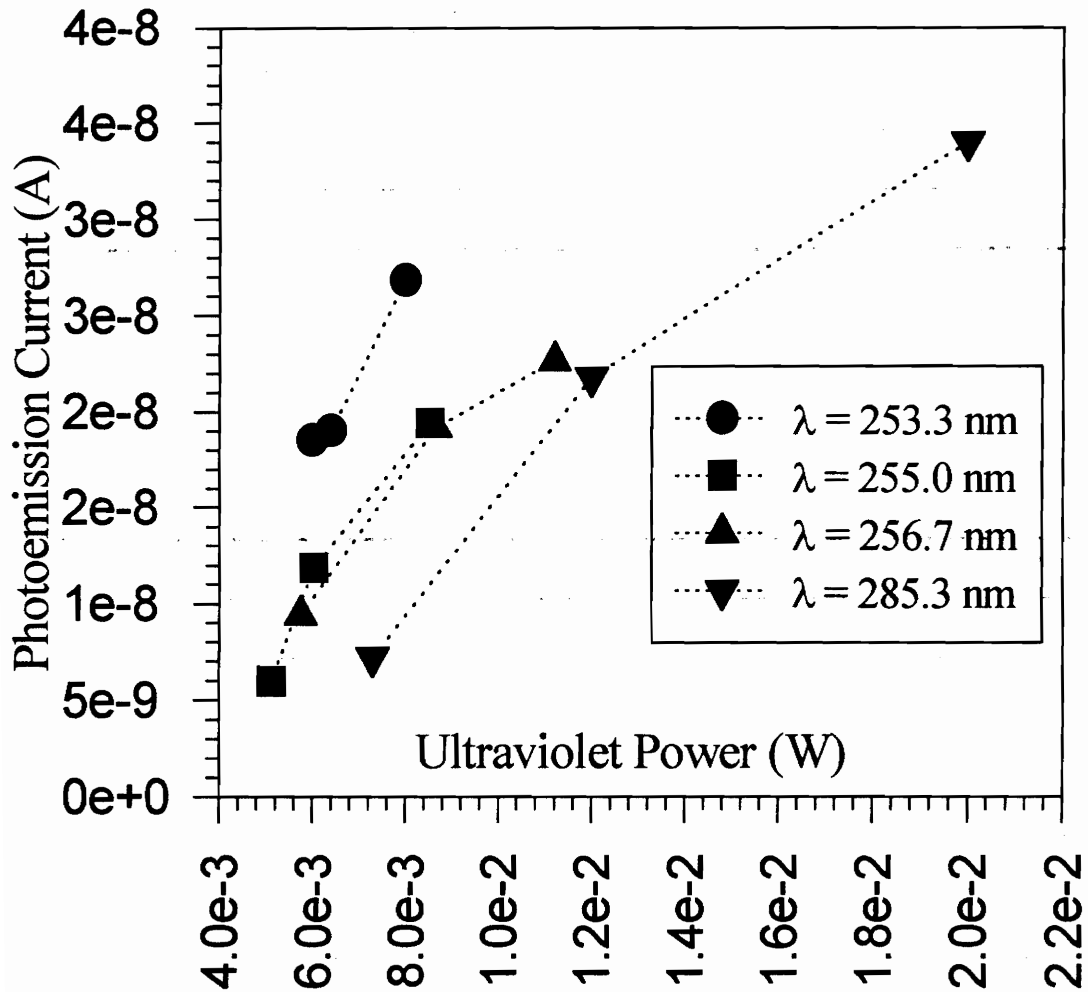

Figure 4.6. Photoemission Current versus Ultraviolet Power.

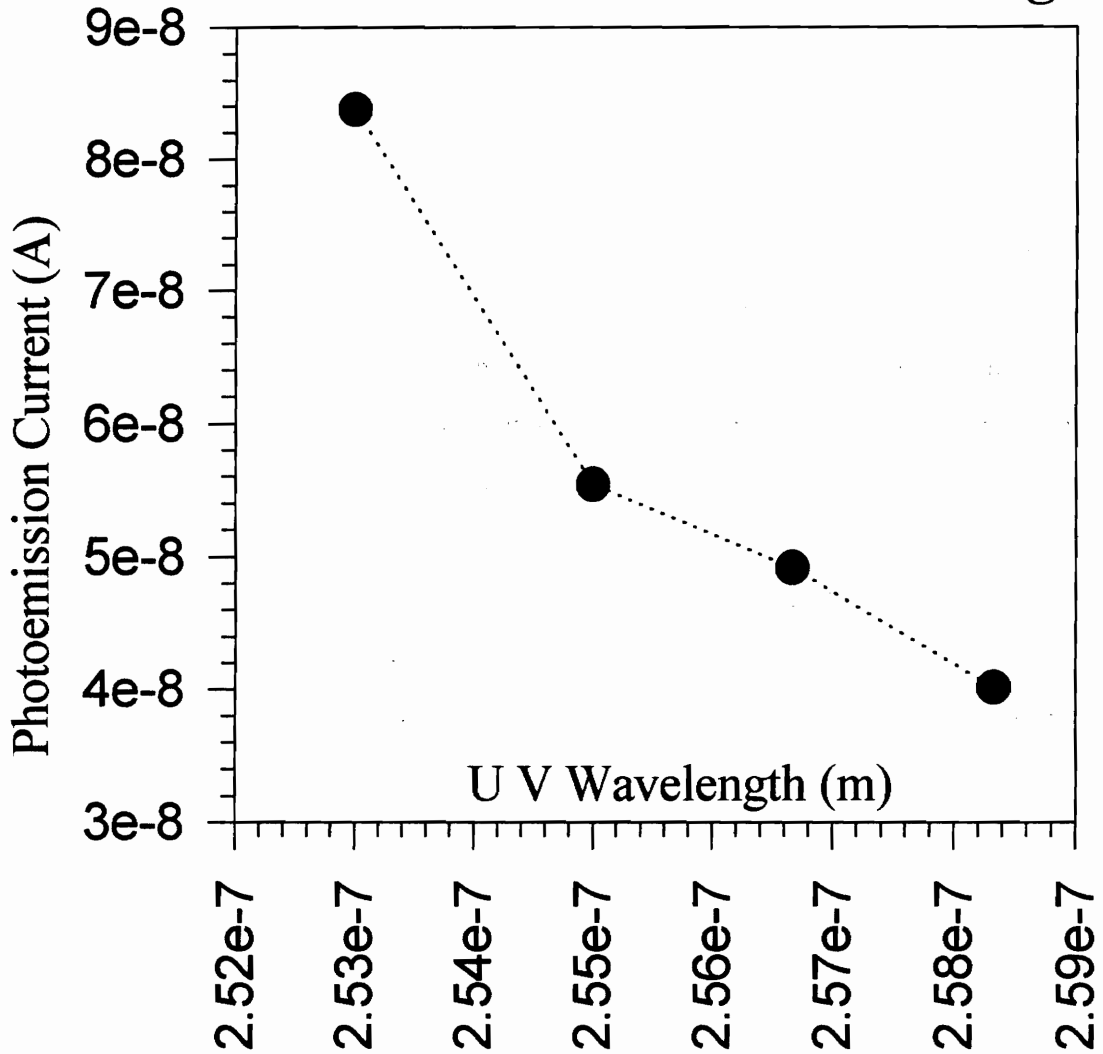

Figure 4.7. Photoemission Current versus Wavelengths.

Table 4.1

Sample	Metallization	Thickness (Å)	UV Power (mW)	Photoemission Current (nA)
# 1	Au	180	2	1.0
# 3	Lab_6\Au	180/180	2	1.79
# 4	Au	180	2	2.0
# 5	Lab_6\Au	180/180	2	2.2
# 6	Au	300	2	1.9
# 7	Au	263	2	2.4
# 8	Au	355	1.4	1.37
# 9	CaF_2\Au	400/250	1.4	2.38

Table 4.2

Metallization Type	Thickness in (Å)	Internal Surface Resistance
Au	180	24 Ω
Au	263	31 Ω
Au	355	7.5 Ω
Lab_6\Au	180/180	28 Ω
Lab_6\Au	200/200	20 Ω
CaF_2\Au	200/250	22 Ω
CaF_2\Au	400/250	0.2 Ω

power of more than 20 mW. Also, the ultraviolet focusing lens to the photocathodes was increased to 15 cm, to better place the focal point of the ultraviolet light within a few Armstrong's of the metal/vacuum interface.

The ideal acceleration voltage needed for application with the photocathodes, was obtained by sweeping the photoemission current versus acceleration voltage. The results indicated that an acceleration voltage of 10 kV provided the best results. From this information, the acceleration voltage was set to 10 kV and the samples tested. The results can be seen in Table 4.3. From Table 4.3 the best photocathode was the CaF_2\Au of 400/200 Å, which produced photoemission currents in excess of 150 nA. However, some problems were encountered with the longevity of the photocathodes. The reason for this is not quite known yet, but one explanation could be the increased power was producing a faster rate of hydrocarbon generation in the vacuum. These hydrocarbons eventually build up on the front surface of the photocathode resulting in a decrease in photoemission current. One test that seemed to confirmed this thought was moving the focus spot to another location. The result was an increase in the photoemission current back to its original value. Figure 4.9 shows the photoemission current for the 400/250 Å CaF_2\Au photocathode. The overall results of the photocathode characterization showed:

- Un-roughen quartz substrates led to better performance of the photocathodes than roughen.
- The optimum thickness for the various photocathodes was: Au of thickness 200 Å, Lab_6\Au of thickness 200/200 Å and CaF_2\Au of thickness 400/200 Å, of which CaF_2\Au was the best.
- Preferred acceleration voltage was at 10 kV.
- Focal length of 15 cm was best for extraction of photoemission current from the photocathodes.
- The distance of separation between anode and cathode was adjusted to 4 mm.
- Higher UV power to the photocathode resulted in greater photoemission current.
- The overall highest photoemission current was in excess of 200 nA.

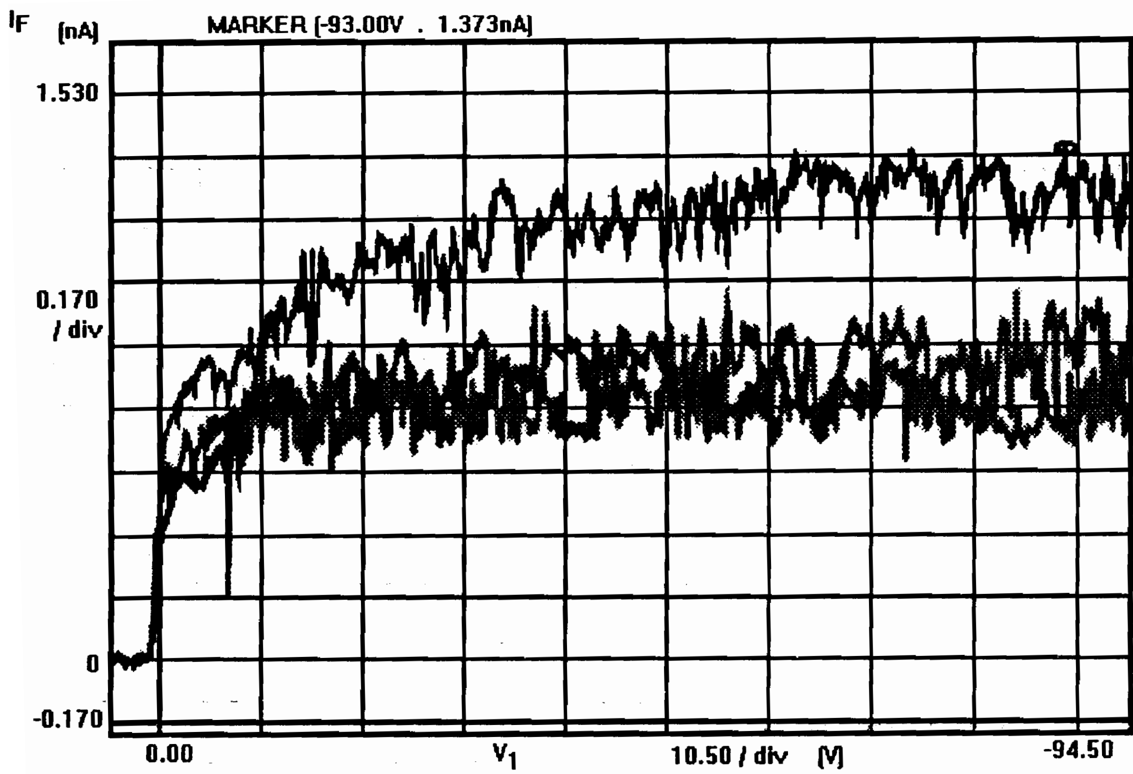

Figure 4.8. Photoemission Current for 355 Å Gold Photocathode.

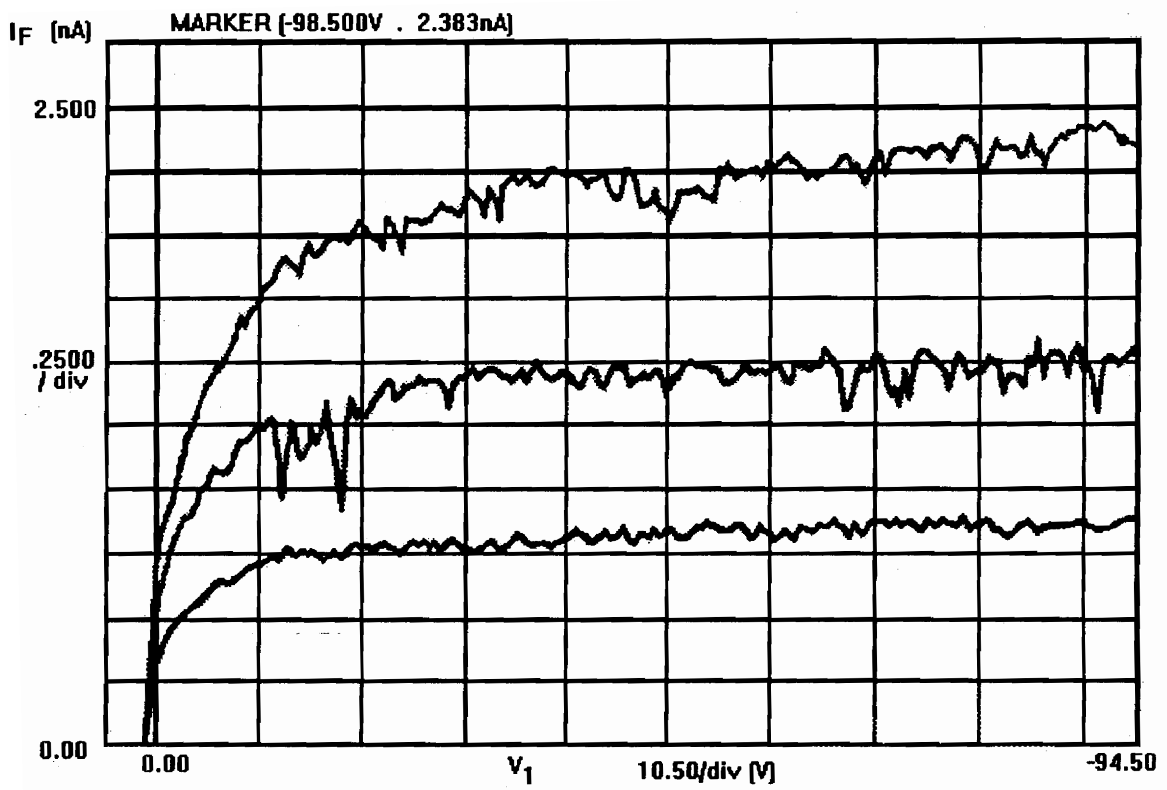

Figure 4.9. Photoemission Current for 400/250 Å CaF_2\Au Photocathode.

Table 4.3

Sample	Metallization	Thickness (Å)	UV Power (mW)	Photoemission Current (nA)
# A	CaF_2\Au	400/100	20	50
# A.1	CaF_2\Au	400/100	30	54
# C	CaF_2\Au	400/50	20	42
#C.1	CaF_2\Au	400/50	30	48
# B	Lab_6\Au	180/180	30	90
# B.1	Lab_6\Au	200/200	30	95
# D	CaF_2\Au	400/173	30	98
# E	CaF_2\Au	400/200	25	105
#E.1	CaF_2\Au	400/200	30	154

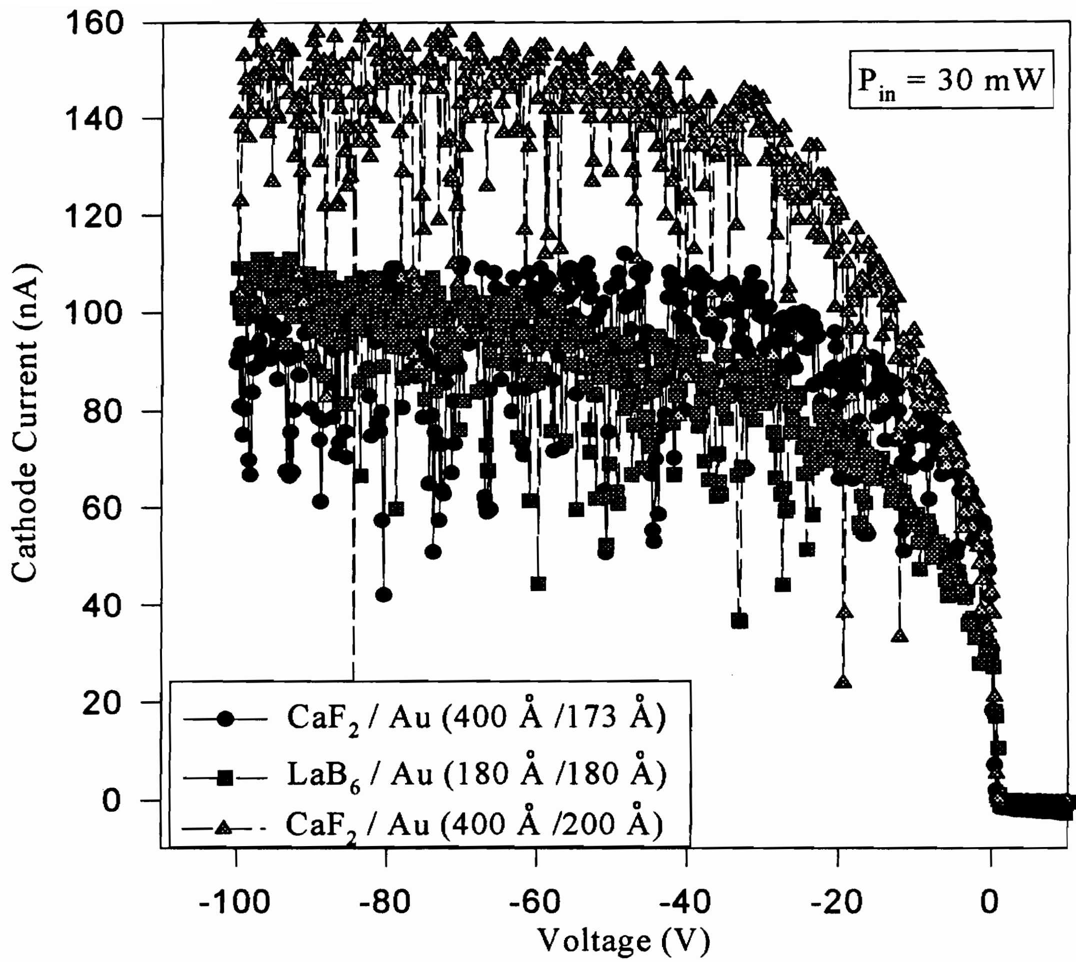

Figure 4.10. Photocathode current voltage characteristics.

Figure 4.10 shows an accumulation of some of the results for the best photocathodes developed: the CaF_2\Au of thickness 400/173 Å with a photoemission current of 98 nA, the Lab_6\Au of thickness 180/180 Å with a photoemission current of 90 nA, and the CaF_2\Au of thickness 400/200 Å with a photoemission current of 154 nA. Here the incident ultraviolet power was 30 mW.

From all of the testing performed on the photocathodes, the overall results were an order of magnitude higher than that reported by Scott[(20)]. The 400/200 Å thick was then incorporated into the L-EBIC wide bandgap measuring system.

4.2 Material Preparation

In order to obtain the carrier transport properties of GaN and diamond, the experimental system was first tested using two known materials: silicon (Si) and gallium arsenide (GaAs). These materials were chosen because of their availability to the project, and because their carrier transport properties have been well documented. All the Si and GaAs wafers were supplied by Howard University, Solid State Group. They were prepared for characterizing the system by fabricating three types of devices from the wafers. The devices made were: p-n junctions, metal/insulator/semiconductor (MIS) devices and double ohmic devices.

All of these devices were fabricated using a mask made at Virginia Polytechnic and State University's Microelectronics Laboratory. The mask was fabricated using a YAG Laser Trimming System model 25, with various dots, lines and spacing ranging from 10 μm to 500 μm. All of these devices were then tested for their current voltage characteristics in various test fixtures. After satisfactory results were obtained from these crude devices, the system was used to test the two wide bandgap materials (GaN and diamond).

4.2.1 Silicon Samples

The Si wafer supplied were compensated (100) and (111) types, with resistivity between 10^9 and 10^{10} Ω-cm for the (100) type and 3 x 10^4 Ω-cm for the (111) type. The thickness of both wafers was 300 μm and with only one side polished. The expected dark current from any device fabricated from this wafer was to be within 0.52 nA-1.57 nA range. The induced current, as a first order approximation, is equal to the electron beam current times the number of electron-hole pairs generated. Since the electron beam current was at least 200 nA, from section 4.1.3, and if for the worse case one electron creates one electron-hole pair, then the induced current is at least two orders of magnitude greater than the dark current. Therefore, the fabricated devices should detect the electron beam induced current generated from the excess carriers within the material, because the theoretical dark current was at least two orders of magnitude lower than the theoretical expected induced current.

The first device fabricated from this wafer was the double ohmic contact device. This device was made by depositing 10 μm aluminum (Al) pads on both faces, with each pad being 1 kÅ thick. A layout of this device can be seen in Figure 4.11, where it is mounted in the vertical test fixture. The wafer was diced into various sizes ranging from 1 x 1 mm to 5 x 5 mm square samples, depending on the test fixtures to be used. The samples were prepared for the photolithography process by first heating them in a solution of H_2SO_4 to remove any old photoresist or organic material. They were then heated in a solution of HNO_3 to dissolve any metals on the surface. This was followed by a brief dip in dilute HF to etch away the top layer that may contain inherent impurities, then rinse in H_2O and dried.

The photolithography process used to create the contact pads were a lift-off process. In this process the wafer was placed under the mask and the Al metallization deposited. The main problem with this device was the difficulty encountered in

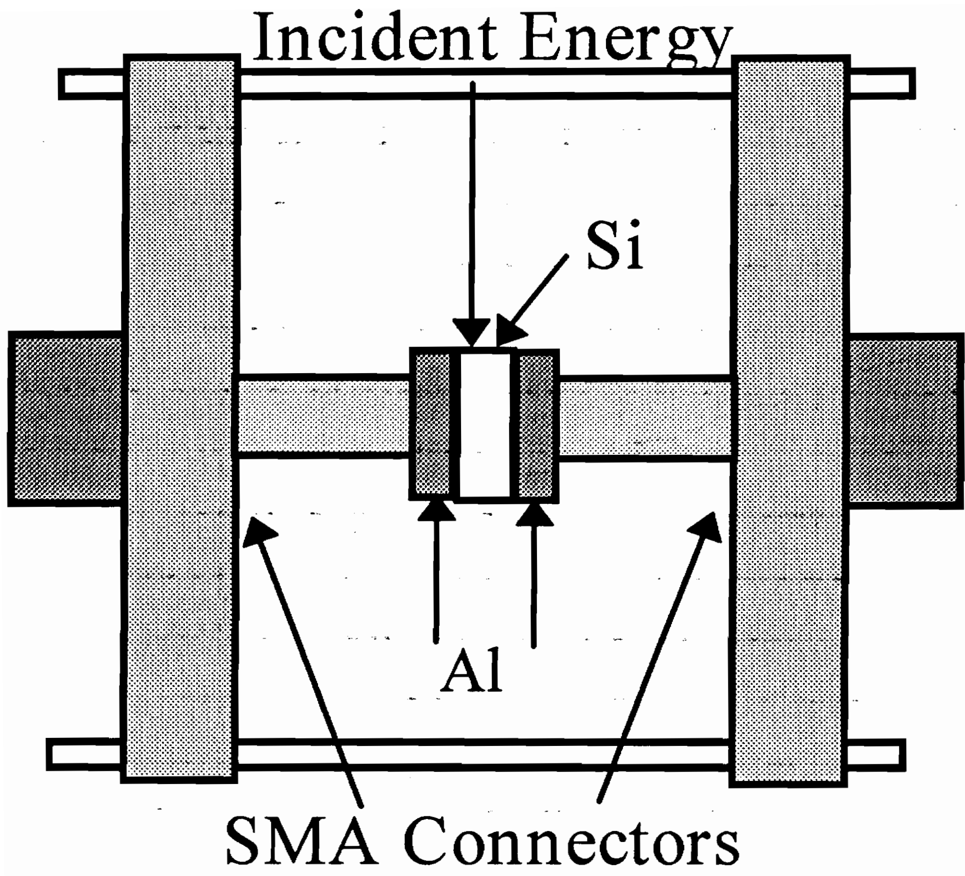

Figure 4.11. Si Double Ohmic Device in Vertical Test Fixture.

assembling and aligning the contacts within the test fixtures. This problem was solved by mounting the devices under high magnification.

The current-voltage characteristic of the double ohmic device is shown in Figure 4.12. The characteristic tends to become less ohmic with an increase in negative bias. This could be due to the un-polished back side of the wafer, which when contacted, could have enclosed traps, voids and other forms of contaminants. These defects formed after metallization, would result in a slightly anomalous behavior of the device, as observed in Figure 4.12. The resistivity measured from the I-V characteristics was 1.51×10^9 Ω-cm at 32 V, which was in agreement with the supplier.

The (111) Si wafer used in fabricating the p-n junction devices were prepared in the same manner as the double ohmic devices, by first performing a standard cleaning described before. Figure 4.13 shows the p-n junction Si device, where (a) shows the metallization layers and (b) shows the testing for the reverse bias setup. The p-n junctions were made by a two step process. First ohmic contacts were laid down on the back side by thermally evaporating Al to a thickness of 1 kÅ, then breaking vacuum the samples were flipped and shadow masked. The schottky contacts were made by depositing a combination of gold and antimony (Au/Sb) to a thickness of 1 kÅ in 16 mill pads. After processing the samples were annealed at 1000°C for 15 seconds.

The current-voltage characteristics of the Si p-n junction device after 5 hrs. of operation can be seen in Figure 4.14. The figure shows that the device still maintains its diode characteristics after being operated continuously for 5 hrs. However, these devices had a relatively low breakdown voltage, on the order of 200 Volts. From Tyagi[50] the expected breakdown voltage should have been in the kilovolts range. One possible explanation for this condition was leaky contacts, especially on the un-polished side, where pits and voids may have formed after metalization.

The Si samples used in the fabrication of the metal/insulator/semiconductor (MIS) devices were from low resistivity Si wafers of (100) orientation and resistivity on the order of 100 Ω-cm. Figure 4.15 shows the layout for the fabrication of these devices. The three

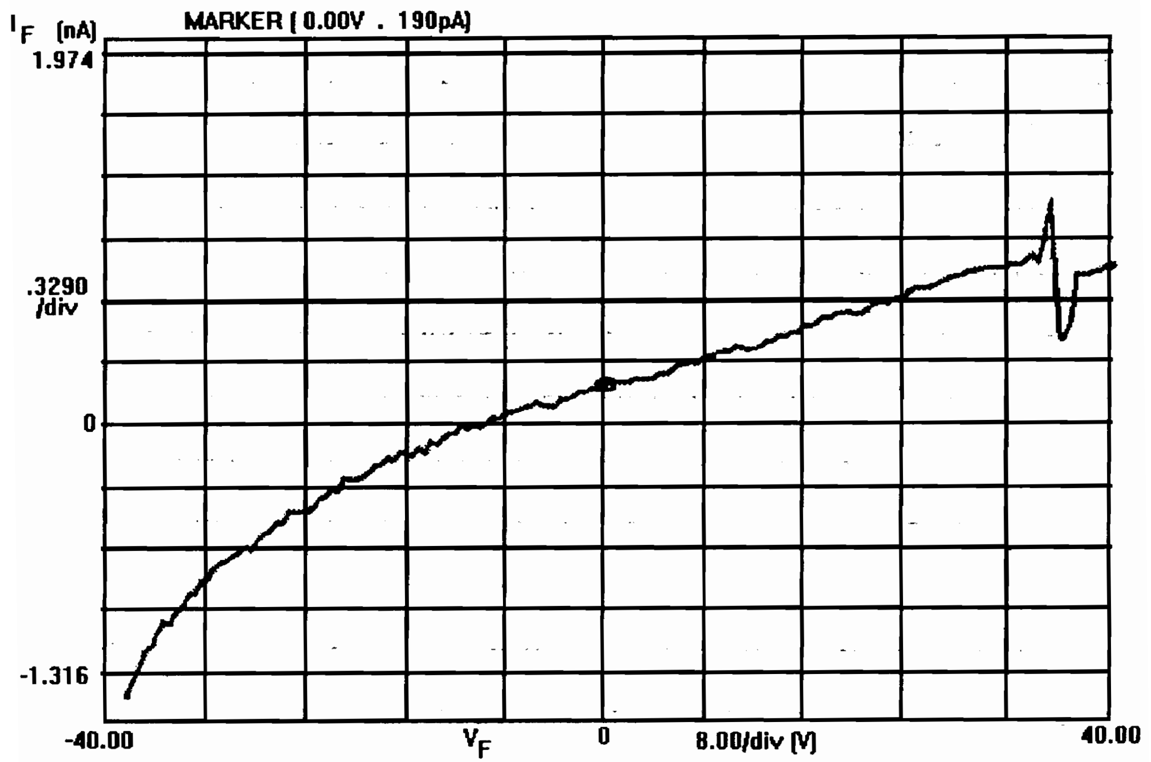

Figure 4.12. I-V Characteristics of Si Double Ohmic Device.

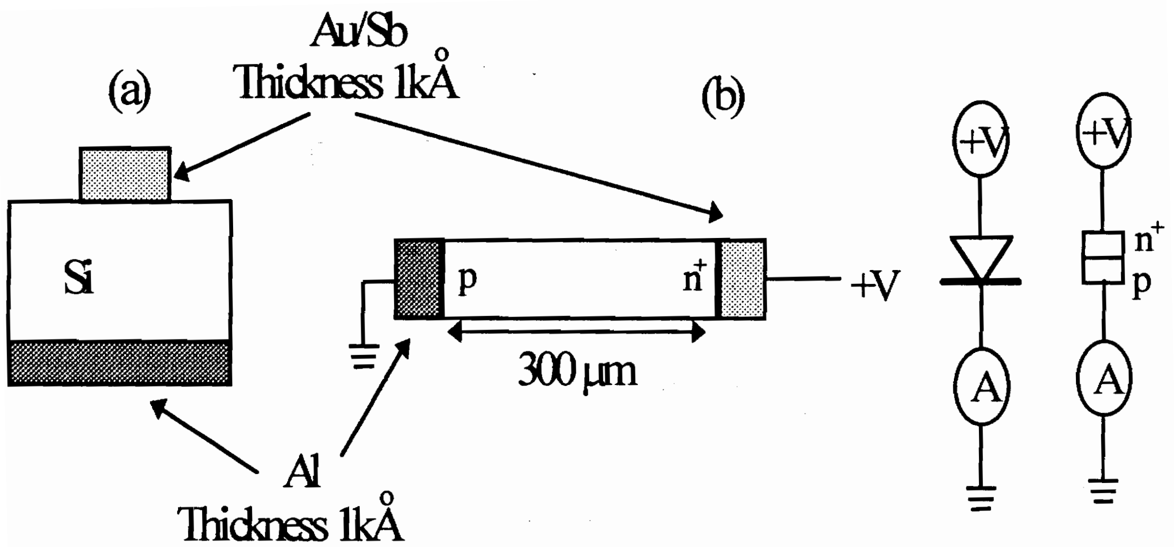

Figure 4.13. Si p-n junction device.

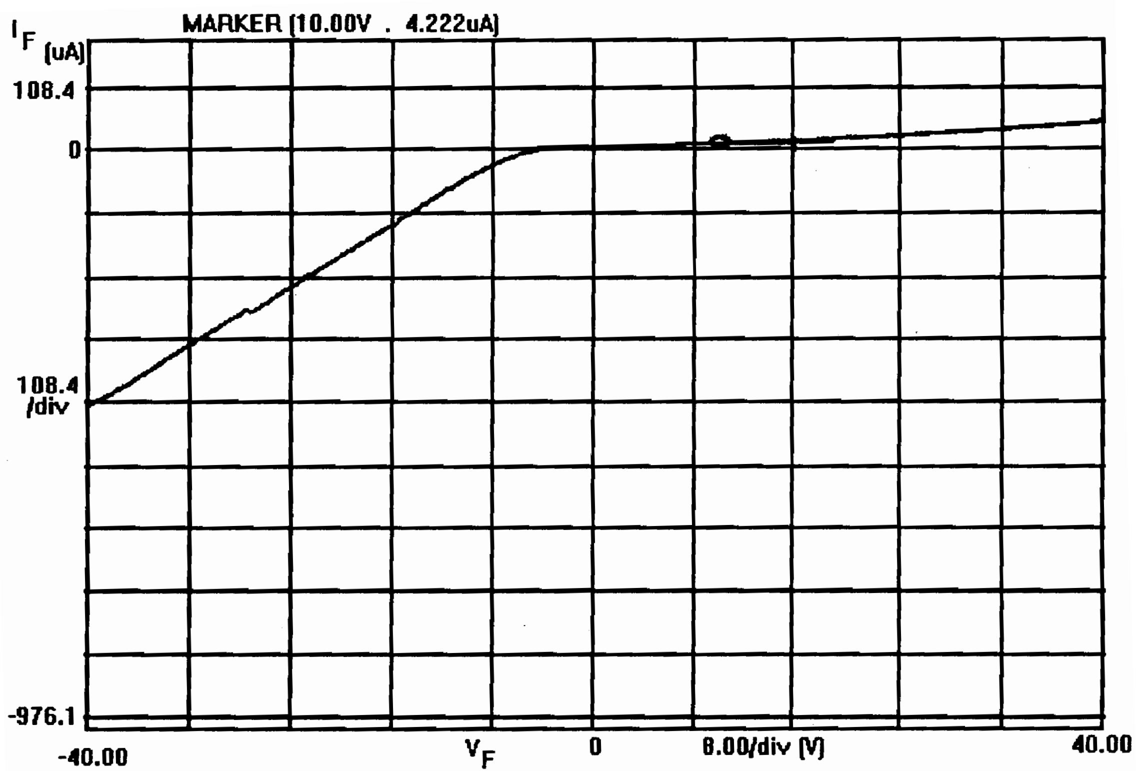

Figure 4.14. I-V Characteristics of Si p-n junction Device.

step fabrication process was preceded by the standard cleaning described earlier. The ohmic contacts of Al were thermally deposited first on the back un-polished side of the wafer, followed by the deposition of CaF_2 and then another layer of Al. Both layers of Al were 1 kÅ thick, with the shadow masking deposition technique used for the layer above the CaF_2. This Al contact layer above the CaF_2 was circular pads with a diameter of 16 mils. The thickness of the CaF_2 was varied for different samples, from 200 Å to 500 Å in steps of 100 Å.

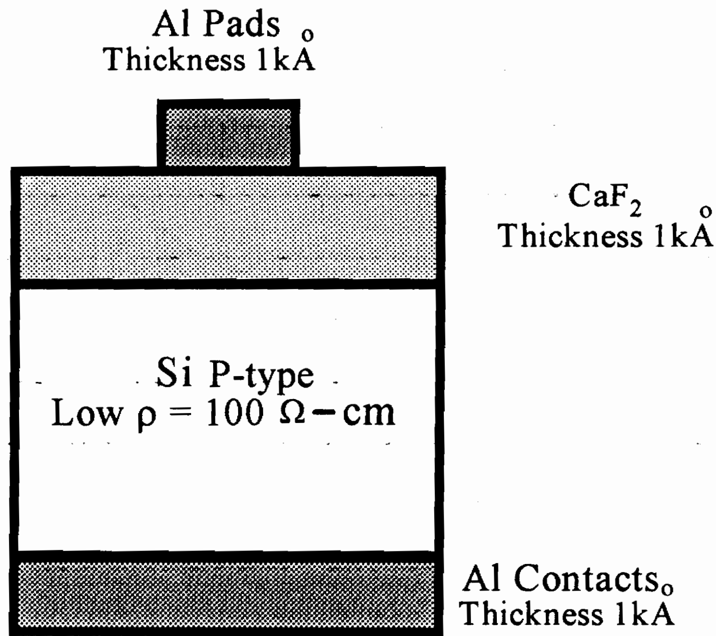

Figure 4.15. Si MIS Device.

The results of the current-voltage characteristics of these devices were too leaky for them to be used in any system. The dark current was well above 500 nA at 5 Volts. The reason for this problem was believed to be the porous nature of the CaF_2 layer. The deposition process of this layer was believed to have been contaminated due to equipment failure during preparation. This contamination could have provided the means for breakdown in the layer and ultimately the device.

The best Si results of all the fabricated and tested devices were the double ohmic devices. These devices were then chosen to be used in the calibration of both the laser and thermal EBIC systems.

4.2.2 Gallium Arsenide

After working with the Si samples, the need arose to find another material that had low background concentration and high resistivity that was easily obtainable. Two wafers of Gallium Arsenide (GaAs) were supplied to the project by Howard University. The wafer thickness' were 500 μm and 635 μm, with resistivity of 10^7 to 10^8 Ω-cm, etch pit density of 5 k cm^2 and slightly p-type. The resistivities were not representative of the doping concentration, because they were highly compensated (10^{14} cm^{-3}). Before the devices were made the wafers were prepared by standard cleaning as described before. In fabricating the double ohmic devices the contacts were made by depositing a combination of gold germanium nickel (AuGeNi) on both faces. The AuGe layer was deposited first to a thickness of 800 Å, of which 12 % was Ge and the remaining 88 % Au. The layer thickness of the Ni was 224 Å. The devices were then annealed at 410 ^{O}C for 30 seconds. The two step deposition process was performed under the same vacuum, however vacuum was broken to switch sides on the samples.

Figure 4.16 shows the current-voltage characteristics of the GaAs double ohmic devices before mounting into the test fixtures. Here the resistivity of the devices was approximately 8 x 10^7 Ω-cm for the 500 μm thick wafer. After assembling the devices into the vertical test fixture the current-voltage characteristics were measured. Figure 4.17 shows the current-voltage characteristics the GaAs double ohmic device assembled in the vertical test fixture before testing, and Figure 4.18 shows the results after testing.

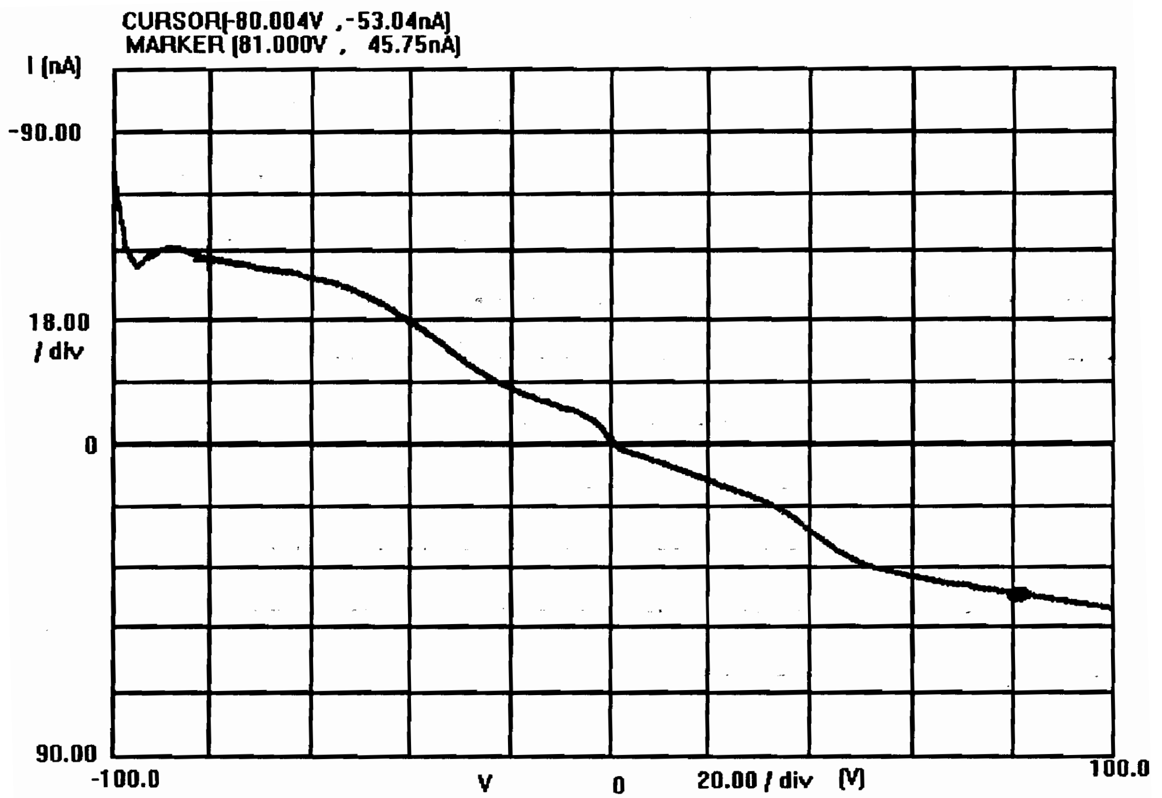

Figure 4.16. I-V Characteristics of GaAs Double Ohmic Device before Mounting.

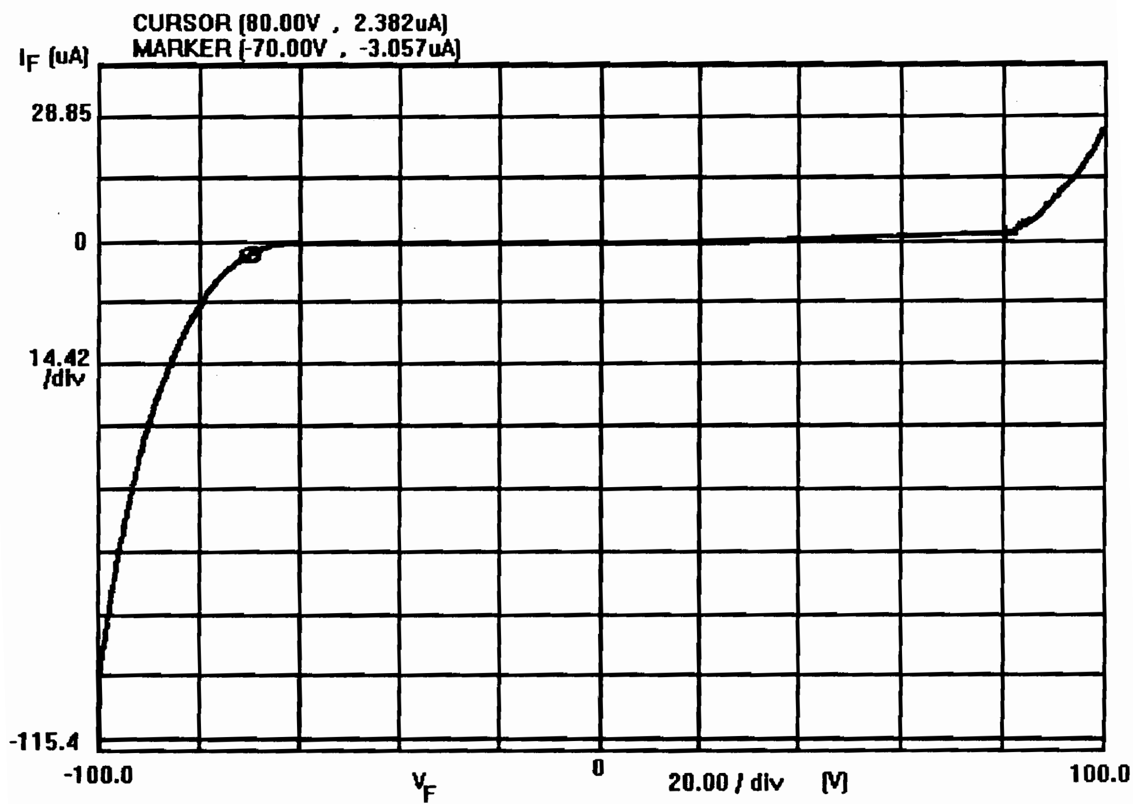

Figure 4.17. I-V Characteristics of GaAs Double Ohmic Device before Testing.

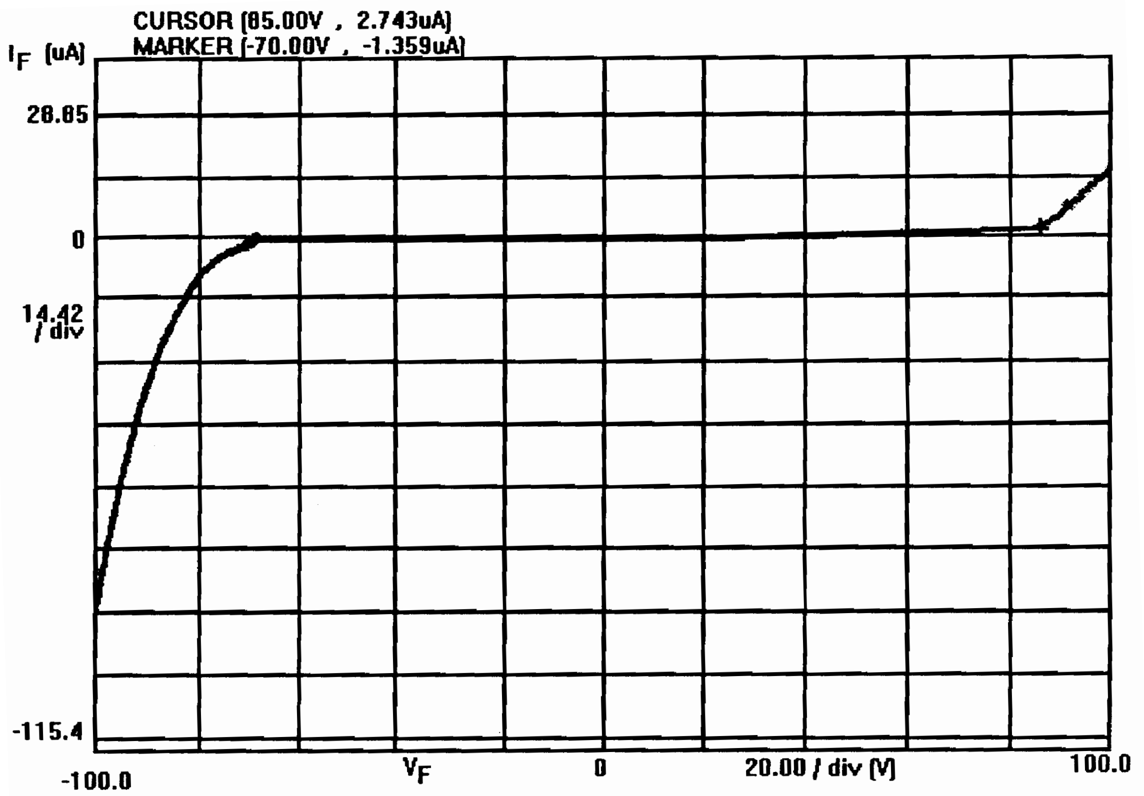

Figure 4.18. I-V Characteristics of GaAs Double Ohmic Device after Testing.

These two figures (4.17 & 4.18) show that after mounting the double ohmic devices into the test fixture, they were mostly ohmic especially in the region -70 Volts to 80 Volts. However, for voltages outside this range, the device current increased drastically with voltage indicating a breakdown trend. It is believed that this trend is due to problems encountered with connecting to the device and the highly compensative nature of the wafer. Observations were made that showed that on varying the contacts the devices behaved more ohmic. The resistivity of these devices was as high as $7 \times 10^6\ \Omega$-cm both before and after testing.

The schottky devices were fabricated with AuGeNi combinations on the back surface and Al pads on the front surface. AuGeNi combinations for the ohmic contact were described before in the double ohmic section. The front surface deposition of Al pads, with diameter 16 mills and thickness of 1 kÅ, by shadow masking were identical to those performed on the Si devices. Before any deposition took place, the wafer was prepared by the standard cleaning process described earlier. These devices worked well enough but did not have as low a dark current as the double ohmic devices.

The MIS devices were also tried on the GaAs wafers. They were processed with the same ohmic contacts to the back side. The front side was electron beam deposited with a layer of SiO_2 and then followed by a contact layer of gold. The SiO_2 layer was 250 Å thick and the gold layer 500 Å. In developing the MIS devices, the use of SIO was replaced with SiO_2 due to availability. This SiO_2 could have been the demise of these devices, because they were found to be very leaky. The dark current was on the order of 2 mA for an applied 20 Volts.

After all the fabrication and testing were completed on the GaAs devices, the most favorable device for the characterization of the system was the double ohmic. These devices were used in both the laser EBIC and OBIC systems.

4.2.3 Gallium Nitride & Diamond

Both the gallium nitride (GaN) and the type IIa natural diamond were supplied to the project already assembled in carriers by the Naval Research Laboratory, in Washington DC (Figure 4.4). Three types of GaN devices were supplied to this research project. The first was a double spiral ring configuration of width 26 μm and separated by 48 μm spacing, the second was a series of transmission lines with spacings from 5 μm and 25 μm and the third was a 3 μm spaced and width interdigitated fingers. The spiral rings were connected by bond wires to 50 Ω transmission lines that was attached to SMA connectors. The transmission lines and the interdigitated fingers used were connected by bond wires to contact pins on the carriers. The processing of the GaN can be found in the article by S. C. Binari et al.(1).

The GaN layer 1.3 μm thick was grown on top of a sapphire substrate by vertical metal organic phase epitaxy reactor. The metalization consists of a 500 μm thick Titanium (Ti) layer covered with a gold overlay by electron beam deposition. The diamond processing could be found in the article by S. C. Binari et al.(3). The contacts to the diamond were made with 500 nm thick Al, each 2.5 mm long and 0.3 mm wide. The distance of separation between the Al contacts was 350 μm each.

4.3 Spot Size

In order to probe the MUT the diameter of the beam needed to be known. The beam diameter would set the limit on how small a spacing between the contacts of the MUT can be probed. This in turn limits the size of the samples that can be used in the experiments. The electron and optical beam profiles were obtained by the same knife edge experiment.

4.3.1 Electron Beam Spot Size

The knife edge experiment was used to find the electron beam diameter in the modified SEM. A razor's sharp edge was connected halfway across the opening in the faraday cup. The razor was grounded and the electron beam was positioned just off the edge into the faraday cup. The faraday cup was moved by turning the translations on the specimen chamber of the SEM. The location of the faraday cup was observed from the micrometer on the translation. The current was monitored as a function of distance, as the beam moved across the blade's edge. The current versus distance relationship, as shown in Figure 4.19, was obtained in both the x and y direction and the beam diameter extracted. The plot was the same for both X and Y-directions, indicating that the electron beam had a symmetrically circular spot size.

The electron beam diameter calculated from Figure 4.19 was found to be 0.31 μm with 20 kV applied. The beam spot size was also measured as a function of accelerating voltage and this is shown in Figure 4.20. These two figures demonstrate the capability to probe structures with high spatial resolution.

4.3.2 Optical Beam Spot Size

The optical beam knife edge experimental setup can be seen in Figure 4.21. Here the razor was placed with its sharp edge connected halfway across the optical detector head. A 5 cm lens was used to focus the laser light onto the detector head. With the use of an XY translation the detector head was moved in one direction (X) and then in the other direction (Y). The data was taken on the position of the translation with respect to the measured power. Figure 2.22 shows the resultant plot for the X and Y-direction.

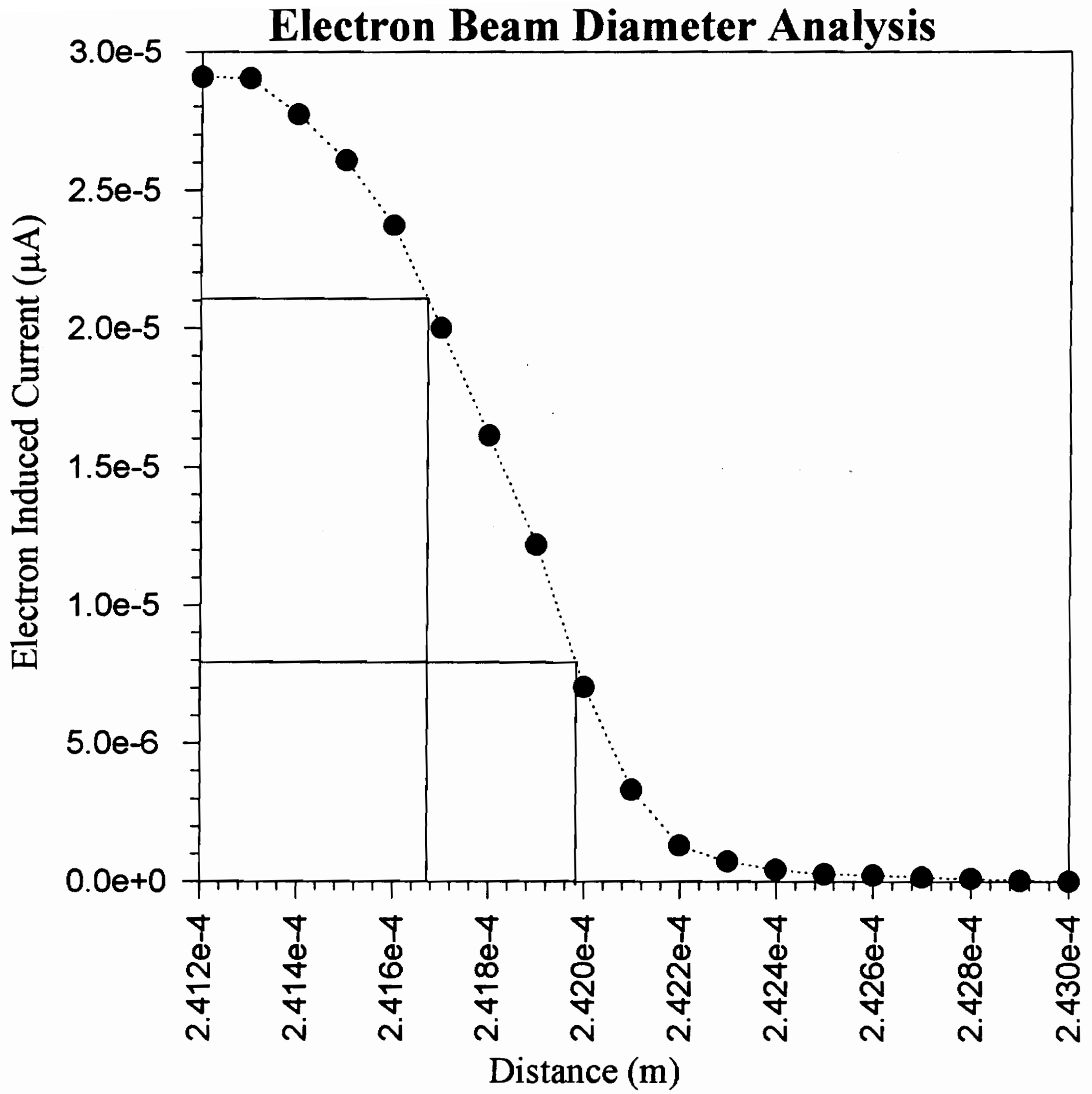

Figure 4.19. Electron Beam Diameter Analysis Results.

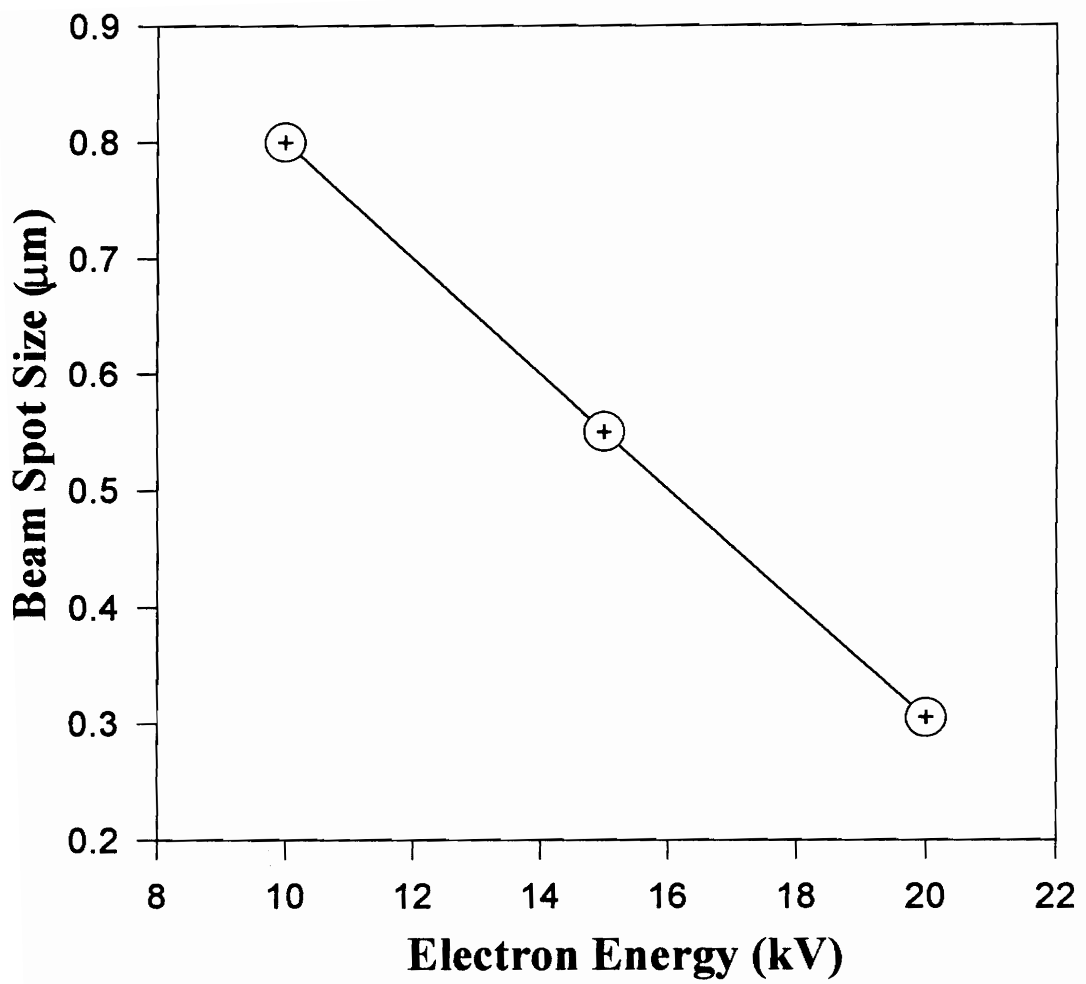

Figure 4.20. Measured Beam Spot Size vs Electron Energy.

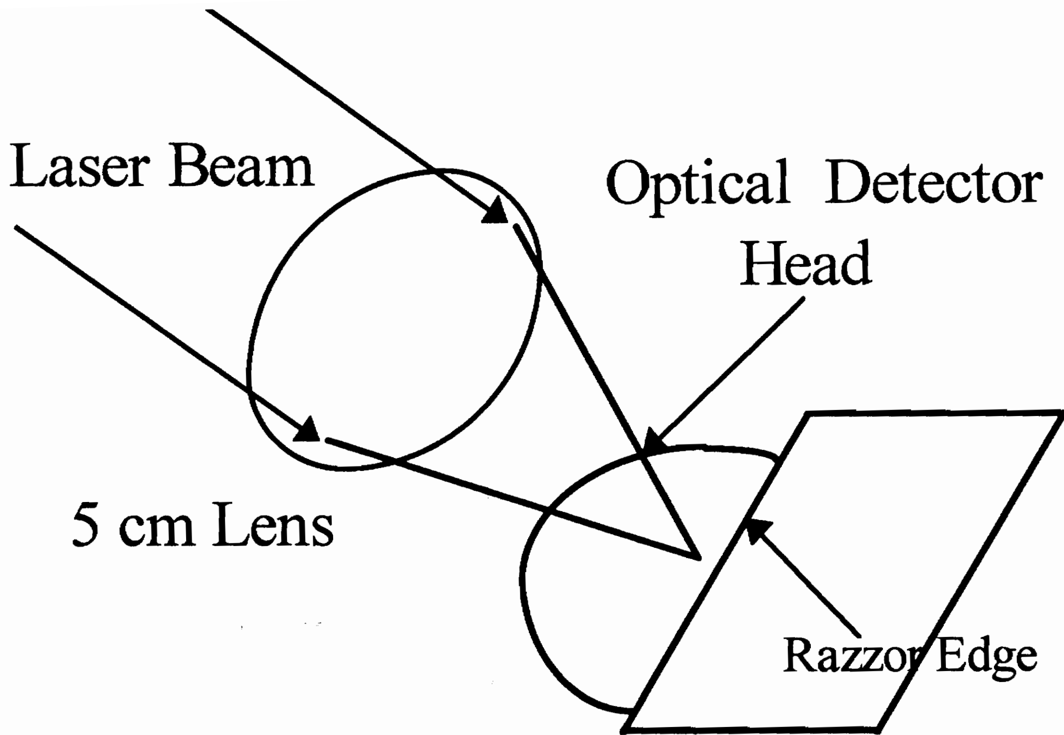

Figure 2.21. Optical Beam Knife Edge Experiment.

The output light produced from the Ti:Sapphire laser was rectangular in shape, with the beam waist given by:

$$2\omega_o = \frac{4\lambda}{\pi}\left(\frac{F}{D}\right) \qquad 4.5$$

where λ is the output wavelength being used (360 nm), F is the focal length of lens (5 cm) and D is the diameter of the original beam (2 mm). The theoretical analysis predicted the beam waist to be 11.46 μm, but actually ω_O was found, from Figure 4.26, to be 16 μm and width to be 4 μm.

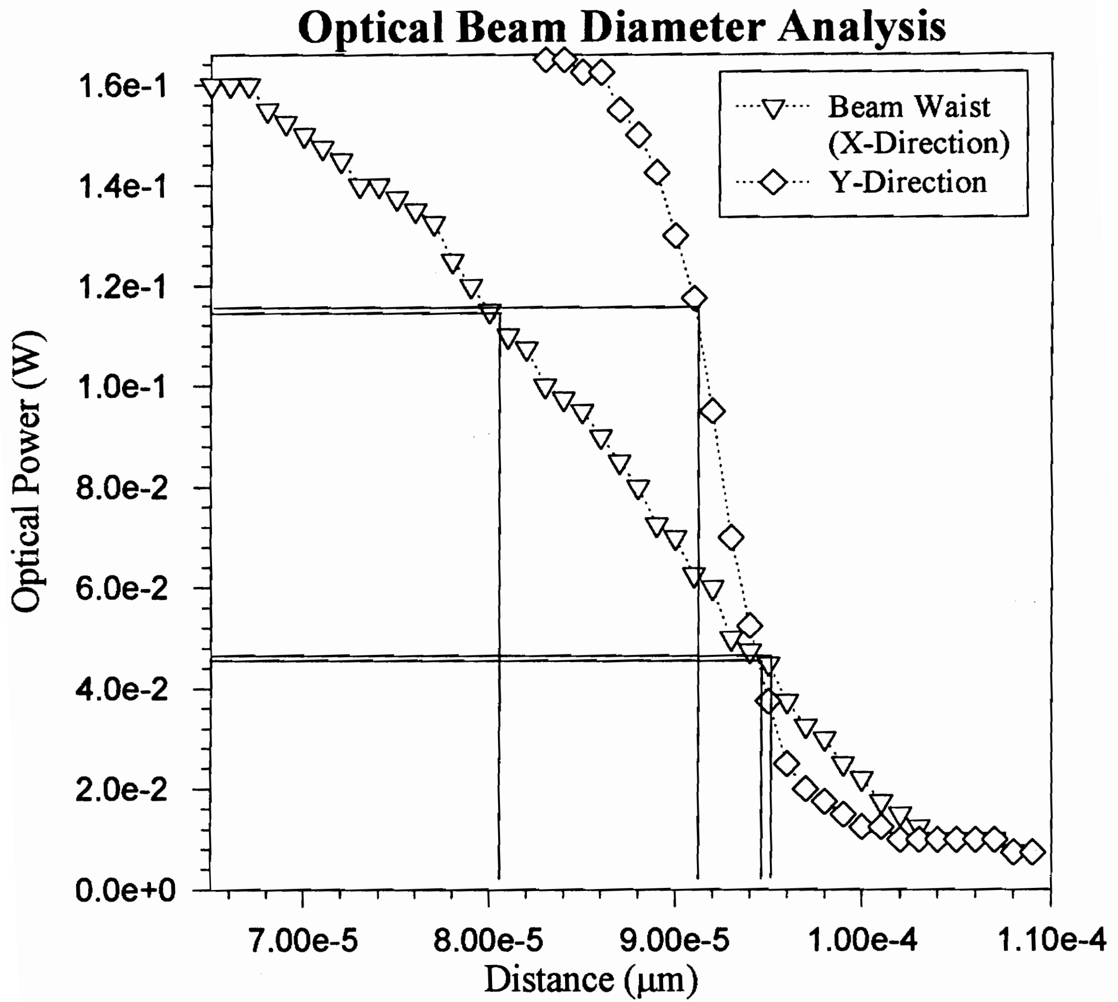

Figure 4.22. Optical Beam Diameter Analysis Results.

Chapter 5

Experimental Setup

5.1 Optical Beam Induced Current Setup

 5.1.1 Lasing System

 5.1.2 Second Harmonic Generator

 5.1.3 High Speed Detection System

5.2 Laser-Electron Beam Induced Current Setup

 5.2.1 Third Harmonic Generator

 5.2.2 Modified SEM

5.3 Thermal-Electron Beam Induced Current Setup

 5.3.1 Thermal Source System

 5.3.3 High Speed Blanker

5.0 Experimental Setup

In this chapter the focus will be on the equipment and conditions that was used in this project to obtain the transport properties of the materials under test. The chapter is divided into three sections, each pertaining to a particular system that was used (OBIC, L-EBIC and T-EBIC). Each section describes the equipment used and the adjustments needed to complete the assembly. In the OBIC system the equipment used was a two part optical generation source, a second harmonic generator (SHG) and a high speed digital oscilloscope. The optical generation source comprised of Ion Argon/Titanium:Sapphire lasers, the main component in the SHG was the nonlinear crystal, and the Tektronix CSA 803 digital oscilloscope was used as the high speed detection component. The L-EBIC used, in addition to the OBIC components, a third harmonic generator (THG) that tripled the output of the Titanium:Sapphire laser and a modified SEM. The modified SEM was fitted with a photoemission source in place of the regular thermionic source and a reconfigured specimen chamber. In the T-EBIC system the electron beam source was produced by a tungsten filament. The stream of electrons was pulsed with a high speed beam blanker. Also, the T-EBIC system used the same modified specimen chamber as in the L-EBIC system.

5.1 OBIC Setup

The OBIC system used a two component source made up of an Ion Argon Gas Laser and a Titanium:Sapphire solid state laser. The Ion Argon gas laser was capable of emitting light in the wavelength from 457 to 514 nm and was utilized to pump the Titanium:Sapphire solid state laser, that operated in the range of 680 nm to 1100 nm. The SHG doubled the output frequency of the Titanium:Sapphire laser using the BBO

nonlinear crystal and two focusing lenses to produced light in the range of 340 to 550 nm. The photoinduced output from the sample was detected by a Tektronix CSA 805 communication signal analyzer fitted with an SD 24 and SD 14 sampling head.

5.1.1 Lasing System

The actual set up used in this experiment can be seen in Figure 5.1. The experimental layout was divided into three sections: the lasing system, the optical harmonic generation section, and the detection section. In the lasing system the Argon Ion high power laser was tuned to 514 nm by adjusting the wavelength selector prism. The output power at the operating wavelength was 13 W with a beam diameter of 1.9 mm. This output was guided into the Titanium:Sapphire laser by optics. The operating frequency of the Titanium:Sapphire laser was anywhere between 700-780 nm with a 200 femto-second pulse width and a 76 MHz repetition rate, depending on the samples being tested.

For the GaN sample the Titanium:Sapphire laser was adjusted (for example by rotating the cavity mirrors and the output slit) to produce horizontally polarized wavelength of 720 nm (red light). The beam diameter at the output was 0.8 mm with an output power of at least 1.5 W. The Titanium:Sapphire laser was found to be very susceptible to fluctuation from any temperature change of the laser crystals. Steps taken to avoid this was supplying the lasing system with its own cooled water kept at 8 ^{o}C by a chiller and purging the Titanium:Sapphire laser continuously with nitrogen. These steps were used to ensure system stability. The operation of the lasers used in this research project was in accordance with laser standard safety procedures.

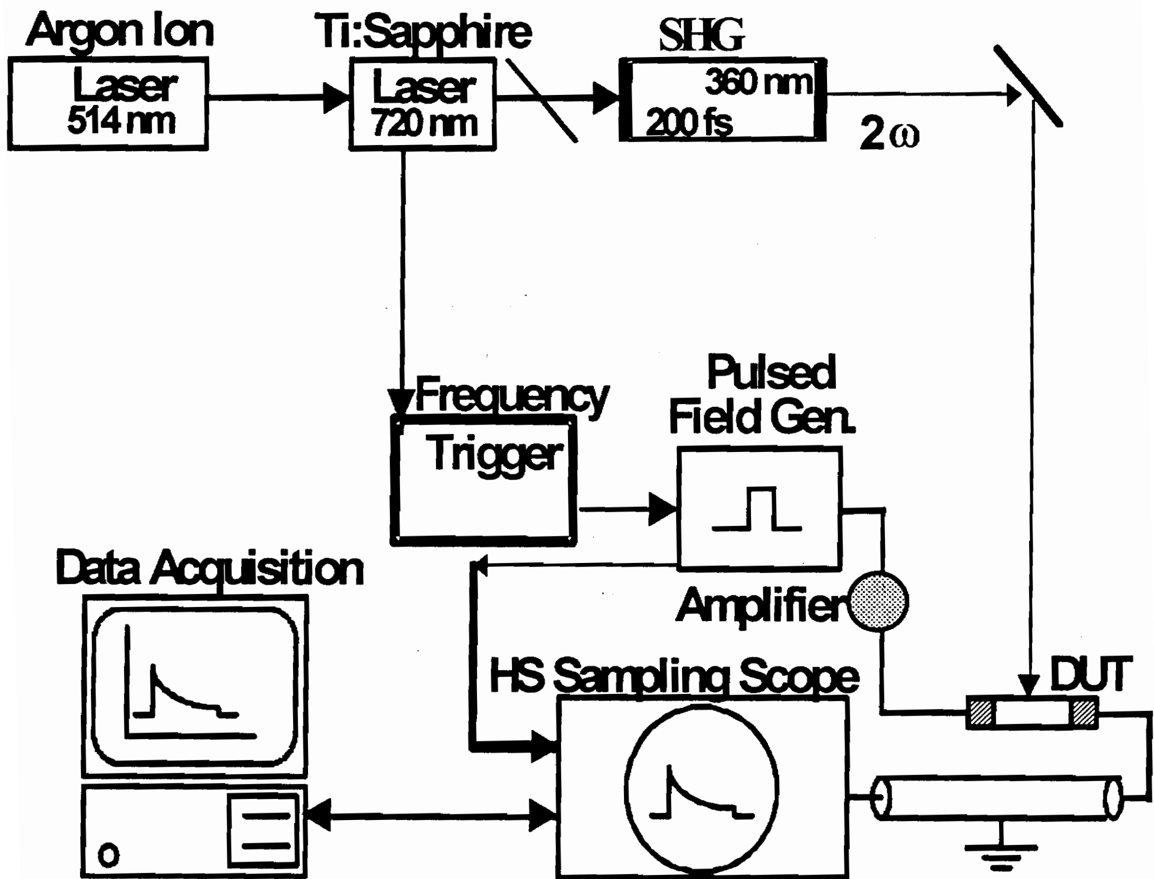

Figure 5.1. OBIC Experimental Setup.

5.1.2 Second Harmonic Generator

The femtosecond output of the Titanium:Sapphire laser was frequency doubled by the use of the SHG to produce light at 360 nm. The setup for the SHG can be seen in Figure 5.2. The SHG was designed with a combination of lenses, beamsplitter, nonlinear crystal and mounts. This combination was capable of producing vertically polarized blue output pulses in the range of 350 nm to 470 nm, from the femtosecond output of the Titanium:Sapphire laser. The use of a short nonlinear crystal was to reduced the pulse broadening due to group velocity mismatch of the fundamental and second harmonic. The group velocity mismatch decreased and spectral bandwidth increased directly with a decrease in crystal length. The group velocity mismatch for the nonlinear crystal used in this research project can be found in the literature published by INRAD INC.[47].

The one inch diameter plano-convex lenses used in the SHG had a short focal length of 63.5 mm and an antireflective coating. The input lens antireflective coating was in the range of 700 nm to 1000 nm and the recollimation lens coating was in the range of

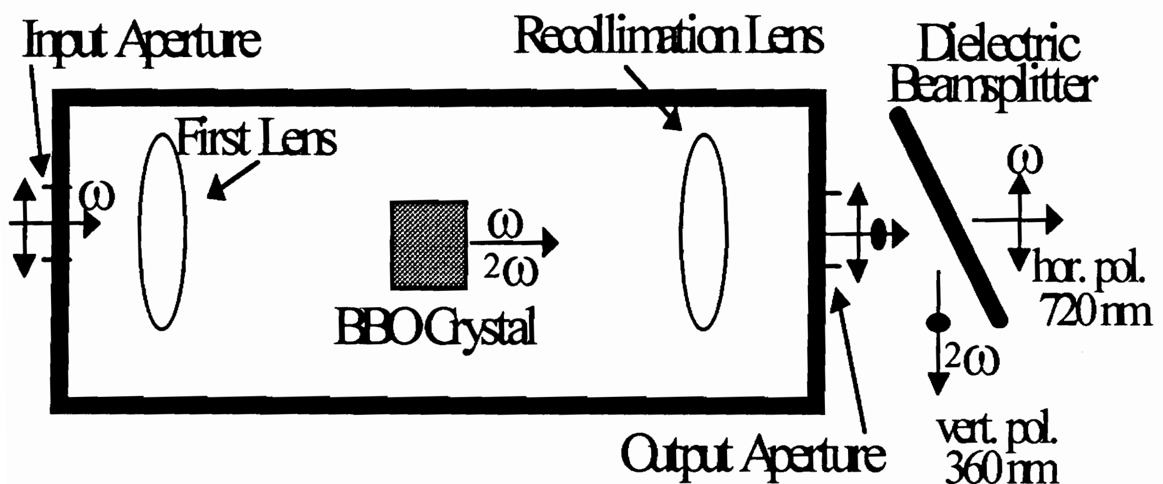

Figure 5.2. Second Harmonic Generator.

350 nm to 500 nm. These lenses were mounted with micrometer adjustments to help position the focused fundamental beam into the center of the nonlinear crystal. As the fundamental and second harmonic beams leave the recollimation lens they were separated by the dielectric beamsplitter. The dielectric beamsplitter was mounted at the end of the SHG at right angles to the output beams. The dielectric beamsplitter was designed to reflect s-polarized light in the wavelength range of 350 nm to 470 nm, (that is, to reflect the vertically polarized second harmonic) and transmit the p-polarized light in the range of 700 nm to 940 nm (that is, to transmit the horizontally polarized fundamental harmonic).

Experimentally, the out light from the lasers was focused into the SHG at low power with the use of the micrometer adjustments. The beam of light was adjusted to the center of the front aperture, then the first lens and finally into the middle of the nonlinear crystal. At full power the nonlinear crystal was tilted about its axis to achieve the phase-matching conditions required for optimum output power. The recollimating lens was then used to adjust the focus of the second harmonic out of the final aperture and onto the dielectric beamsplitter.

The output vertically polarized blue light of wavelength 360 nm, from the dielectric beamsplitter, achieved a constant output power of at least 500 mW. This light was directed to the test fixture, and the end result of the optical path can be seen in Figure 4.2. The samples to be tested were mounted into the test fixture and at low output powers, under magnification, they were aligned for excitation by the second harmonic of the Titanium:Sapphire laser.

5.1.3 High Speed Detection System

Before testing could have actually began, the electronic system for capturing the transport properties needed to be in place. The high speed detection system was comprised of the trigger components, the amplification network, the high speed sampling

oscilloscope and the data acquisition component. The trigger system used was a double component frequency counter that was triggered off the Titanium:Sapphire laser. This counter reduced the laser 76 MHz frequency to produce an output pulse once every 256 times. The resulting output frequency was a 296.8 kHz signal with a 200 ns pulse width. The setup for the triggering system can be seen in Figure 5.3. The 296.8 kHz signal was feed into a Wavetek pulse generator and the output pulse width was reduced to 10 ns. The trigger output of the pulse generator was used to trigger the sampling oscilloscope. The trigger input of the sampling oscilloscope was buffered with a 20 dB attenuator to reduced the trigger signal to 1.2 V. This was done to ensure no damage due to voltage surges could affect the scope.

The output of the pulse generator was amplifier to increase the amplitude to a range of -2 V to -70 V, with a pulse width of 10 ns. This amplified signal was coupled to the MUT. The induced response from the generation of electron-hole pairs within the MUT was observed by one of two input ports of the sampling oscilloscope, either the SD 24 or the SD 14 sampling heads. Both input ports had an inherent input capacitance of 0.5 pF, but the SD 24 had an input resistance of 50 Ω, whiles the SD 14 input resistance was 10^5 Ω.

The two sampling heads of the sampling oscilloscope was used to model the input RC impedance to establish the limitations of the system. The total input R′C′ terms were used, where R′ was the total input resistance from the MUT to sampling oscilloscope sampling heads and C′ was the total input capacitance for the same distance. The results showed that the photoinduced response needed from the MUT, had to be at least 20 μA for a spatial response time of 2 ns to be resolved on the SD 24 by the measuring system. For amplitude only detection the minimum photoinduced response needed to be on the order of 100 nA. The total error inherent in the system was found to be less than 10 % for spatial resolution and less than 5 % for amplitude resolution. This OBIC system was used on the GaAs double ohmic device as a bench mark and then applied to obtain the carrier lifetime of GaN.

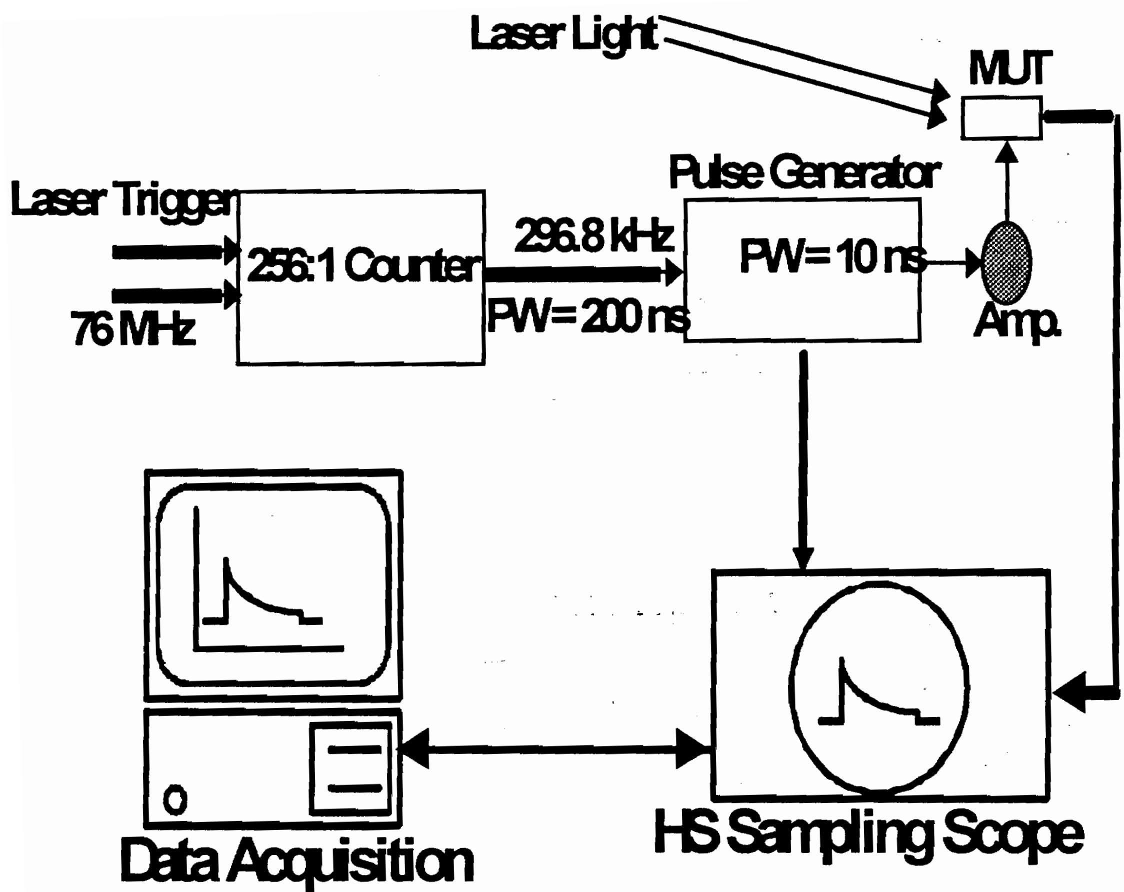

Figure 5.3. Trigger System for OBIC Measurements.

5.2 Laser-EBIC Setup

The set up for this experiment can be seen in Figure 5.4. The experimental layout was divided into four sections: the lasing system, the optical harmonic generation section, the modified SEM and the detection section. The lasing system and the detection section were the same as the ones used in the OBIC experiment. Except in the lasing system the frequency of operation of the Titanium:Sapphire laser was changed to 750 nm. This resulted in the SHG producing vertically polarized blue light at a wavelength of 375 nm.

The main difference between the OBIC and the L-EBIC was the method of electron-hole pair generated. In the OBIC system excess carriers were generated by the absorption of photons, but in EBIC, the generation of electron-hole pairs was by the interaction of an electron beam within the MUT. This section of the chapter will discuss the generation of the third harmonic using the THG, and the electron beam, as well as the process by which the electron beam interacts with the MUT.

5.2.1 Third Harmonic Generator

The third harmonic generator (THG) used in the L-EBIC experiments utilized the fundamental and the second harmonic beams from the Titanium:Sapphire laser to produce the third harmonic. However, the second harmonic was orthogonally polarized with respect to the fundamental beam, so the implementation of a femtosecond delay/rotation stage was used to synchronize the two beams. This femtosecond delay/rotation stage was placed between the SHG and the THG in order to rotate the second harmonic plane of polarization to match that of the fundamental beam. It was also used to overlap the two beams temporal and spatial profiles in the center of the nonlinear crystal of the THG. The reason for the difference in the time delay between the two harmonics was due to the

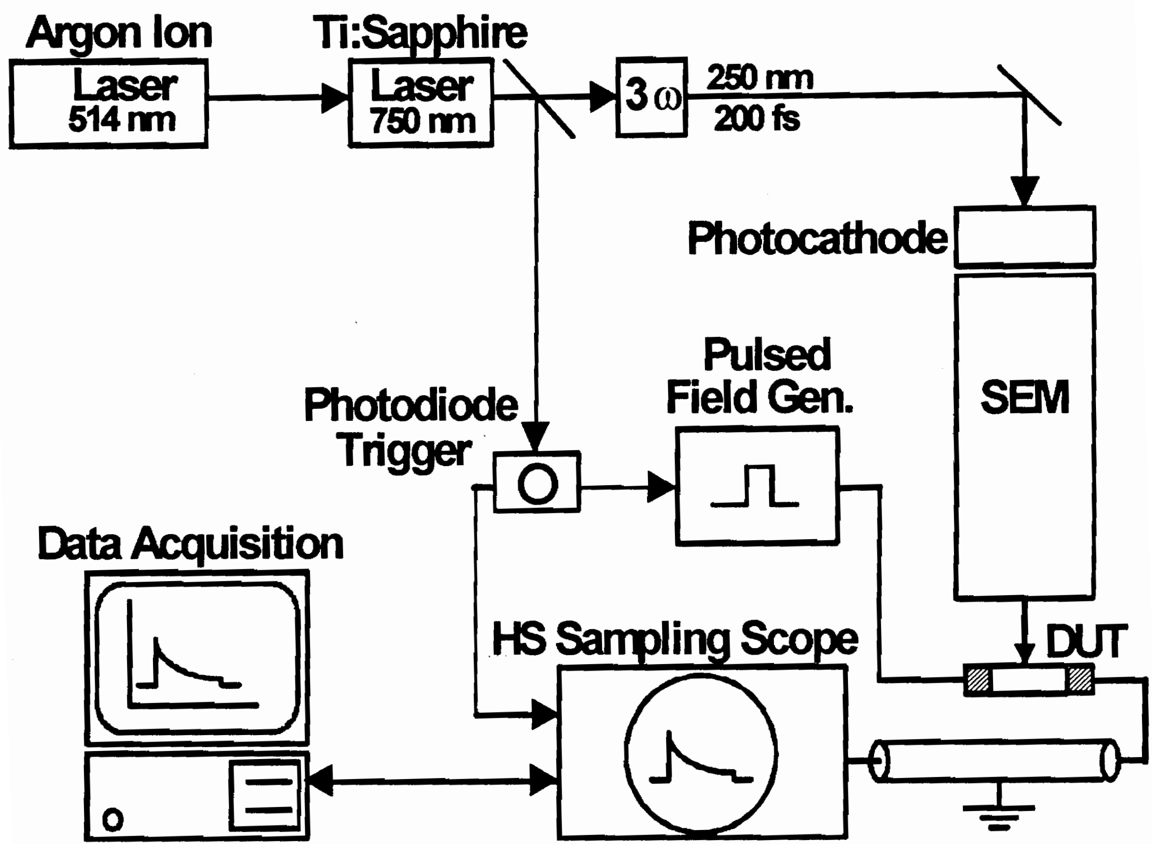

Figure 5.4. L-EBIC Experimental Setup.

walk-off of the second harmonic as it exits the recollimation lens. Therefore the two beams needed to be separated and re-aligned before they enter the THG for mixing. Figure 5.5 shows the experimental setup used to obtain the third harmonic.

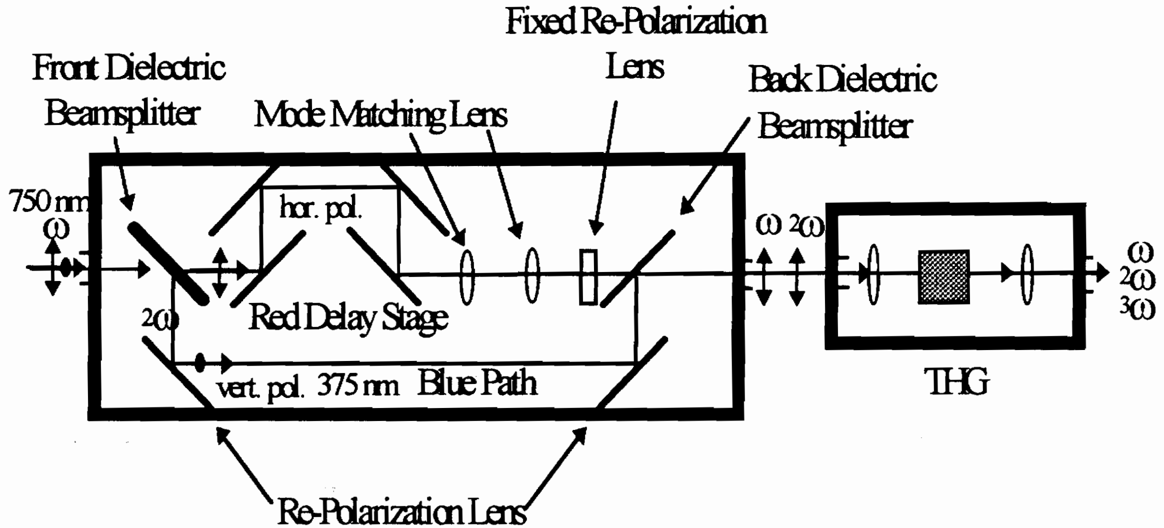

Figure 5.5. Generation of the Third Harmonic.

As the two beams enter into the femtosecond delay/rotation stage they were separated into a blue and a red beam path by the front dielectric beamsplitter. The red beam path was fitted with a variable delay stage to account for the time delay (± 30 ps max.) between the two beams. The adjustment of either mode matching lens pair resulted in the overlap of the red beam with the blue beam. These lenses were used both to direct the red beam along a collinear path with the blue beam and to vary the divergence of the red beam to coincide with the focused blue beam at the same spot in the nonlinear crystal of the THG. The re-polarization lenses in the blue path were used to rotate the blue beam to align with the red beam. A fixed re-polarization lens was also used to compensate for the small polarization rotation produced from the optics in the red beam path. The two horizontal polarized beams were then combined in the back dielectric beamsplitter and focused through the back aperture of the femtosecond delay/rotation stage and into the

front aperture of the THG. The THG operated similarly to the SHG, except the output frequency was the sum of the two input frequency ($\omega_3 = \omega_1 + \omega_2$).

Experimentally the second harmonic was optimized as described in section 5.1.2 at low power. The blue beam was aligned to the red using both a near field and a far field arrangement. This was accomplished by first walking the blue beam as close to the red as possible at the end of the femtosecond delay/rotation stage, then aligning the two together on a marker some distance away. The re-polarization lens was adjusted until the blue beam was parallel to the red, then fine tuning the front and rear dielectric beamsplitter brought the two beams closer together. The process was repeated until the beams overlap in both the near and far fields.

Once the beams overlap, the nonlinear crystal was removed and the two beams were then checked at the location for consistency. Replacing the nonlinear crystal the two beams were aligned at its center at full power. This was followed by adjustments to the red beam delay path. Once this was completed the third harmonic was usually faintly visible on an ultraviolet detector.

The third harmonic was optimized by tilting the nonlinear crystal in the THG and adjusting the front lens until maximum output was achieved. The fundamental, second and third harmonics were all visible on the detector placed at the output of the THG. Due to the walk off between the three beams no dielectric beamsplitter was used. As the beams were directed to the modified SEM the fundamental and second harmonic were far enough away as to not interfere with the generation of the electron beam from the interaction of the third harmonic with the photoemission source. In this system, a consistent operating ultraviolet power of 30 mW was achieved, with a peak power in excess of 35 mW on a regular basis.

5.2.2 Modified SEM

The modified Hitachi S-520 SEM consisted of a photoemission source, a modified specimen chamber and an altered vacuum system. The generating mechanism of the photoemission source was the 400/200 Å thick CaF_2/Au photocathode as described in section 4.1.3. This photoemission source replaced the regular thermionic source. The emission current detected from the Anode/Cathode experimental test as showed in Figure 4.5 was in excess of 200 nA. The initial current efficiency measured by the Faraday Cup at the bottom of the SEM was not as expected, but with adjustments the efficiency of the photocathodes was improved to 52.3 %.

The disadvantage to this modification was an increase in the spot size that resulted in a decrease in resolution and an increase in the spherical aberration. The spherical aberrations increase directly influence the depth of field resulting in its decrease. Also effected was the magnification, which was limited to $\leq$ 1000 X. The ability to focus was reduced, but the capability to resolve 1 μm spacing was still achieved. Overall, the system was still effective enough to perform the measurements necessary to obtain the diffusion lengths, carrier lifetimes and resistivity of diamond and Gallium Nitride.

The specimen chamber was re-modeled to include both the Faraday Cup and the MUT on the same XYZ translation stage, as well as, fitted with four vacuum sealed ports for connections. Two of the ports were used by the Tektronix CSA 803 communication signal analyzer, one was connected to the output of the MUT and the other connected to the Faraday Cup. One of the remaining two ports was used for the input pulsed signal to the MUT and the final port was used to supply the synchronous pulsed trigger signal to the high speed blanker.

Modifications were also made to the vacuum system showed in Figure 3.7. The diffusion pump was replaced with a turbomolecular pump which was the most effective of the pumps tried. It effectively attained vacuum pressures of 10^{-7} Pa. and required little or no maintenance.

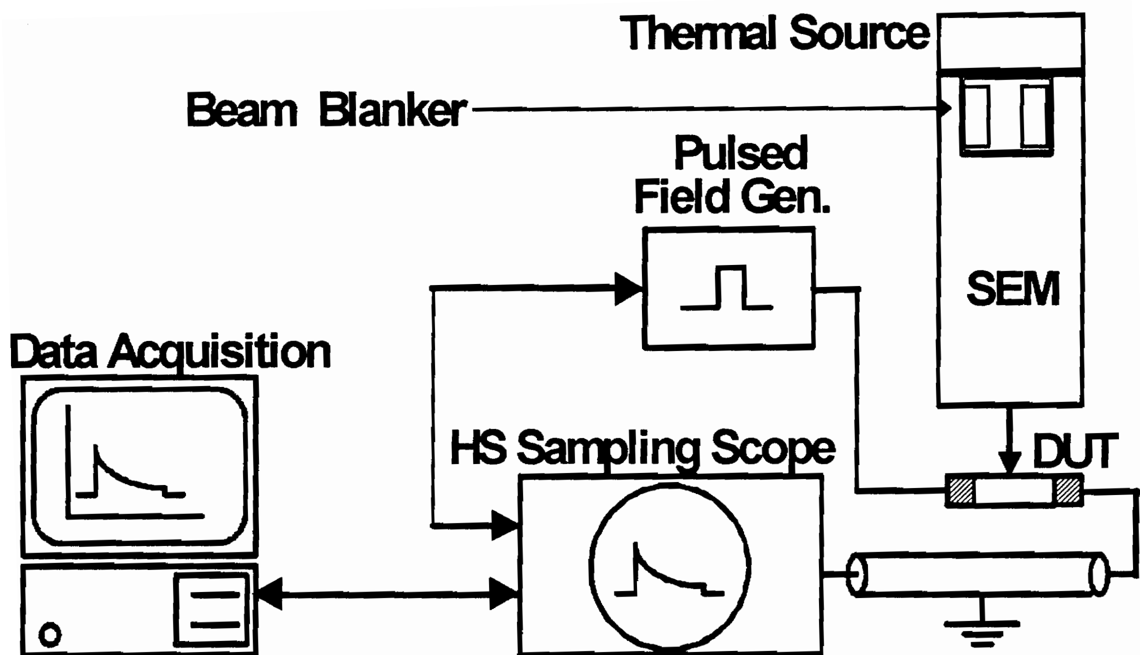

Figure 5.6. T-EBIC Experimental Setup.

5.3 Thermal-EBIC Setup

The set up for this experiment can be seen in Figure 5.6. The experimental layout was divided into two sections: the modified SEM and the detection section. The detection system used in this experiment was the same as in the L-EBIC experiment. The modified SEM here differed from the modified SEM used in the L-EBIC experiment by the method the pulsed electron beam was generated. The generation of the electron beam in this experiment was achieved by the use of the thermionic source described in section 3.2.1. The pulsing action of the electron beam was accomplished by the use of a high speed blanker. The design of the blanker can be found in reference[51]. This section will focus its discussion on the characterization of the thermionic source and its use with the high speed blanker.

5.3.1 Thermal Source System

The V-shaped tungsten filament thermal source provided a constant stream of electrons that was controlled and pulsed. For the modified SEM used, the current received by the Faraday Cup (stage current) from the thermal source varied with emission current. Factors affecting the stage current were shield bias, filament/shield distance, spacing between the cathode and the anode, the environment within the SEM and the accelerating voltage.

The high voltage shield was biased slightly more negative than the filament. The difference in bias was established by connecting the shield directly to the negative high voltage line and placing a variable resistor in the high voltage line to the filament as shown in Figure 3.3. The filament was made less negative than the shield by varying the resistor. The greater the value of the variable resistor, the more negative the shield became relative

to the filament. As the shield became less negative, more electrons were passed through the shield aperture. The overall effect of the variable bias was to regulate the escape of electrons. The optimum setting for the variable shield bias was found prior to beginning the experiment.

Another condition that affected the stage current was the distance of separation between the filament and the shield aperture. The results showed that by moving the filament closer to the shield aperture, allowed more electrons to pass through to the SEM column. However, if the filament was placed too close to the aperture, the bias control by the shield was lost and the emission became excessive. On the other hand, filaments placed too far away from the aperture yielded low levels of electrons. Therefore, a setting of 0.2 mm was found to be ideal for the experiment.

The distance of the anode from filament and shield was also an important factor affecting the stage current. As the distance of separation was decreased more electrons were extracted from the gun, especially at the lower acceleration voltages. However, making the distance too small drastically reduced the lifetime of the filaments. An anode-cathode spacing of 6 cm gave the best results and was used in this experiment.

One of the main causes of no stage current was due to premature filament failure within the SEM. Premature filament failure was directly related to high voltage discharge caused by dirt in the gun region, poor vacuum, air leaks and outgassing from contaminations in the SEM. All efforts were made at all times to wear gloves while working within the SEM and to prevent any extraneous contamination from entering the chamber.

The final mechanism that affected the stage current was the applied acceleration voltage. The acceleration voltage ranged from 1 kV to 25 kV, but to increase the lifetime of the filament, the experiment was performed using the lower range of voltages. Figure 5.7 shows the results of stage current for various acceleration voltages for an emission current of 20 μA and a bias of 3.

The results showed that the most efficient acceleration voltage was at 10 kV, which also correlated with the results from the penetration depth in section 2.3.1. With a setting of 10 kV, and at bias 3 the emission current was varied and the stage current monitored in hopes of further optimizing the system. Figure 5.8 shows the results of stage current with respect to emission current. The results showed that the stage currents in excess of 50 μA could be achieved at the top end of the emission current control, but at these high ranges the lifetime of the filaments was drastically reduced. The range of emission current used during the experiment was from 50 μA to 70 μA.

5.3.3 High Speed Blanker

The high speed blanker was used in the T-EBIC experiment to avoid space charge build up in the MUT as discussed in section 2.3.3. Other types of electron beam pulsing systems can be found in reference[52,53] such as pulsing the central grid of the electron run and Klystron bunching techniques. In this research project the blanking of the electron beam was accomplished by the deflection method. Here the stream of electrons released from the thermionic source was electronically blanked by a parallel plate deflecting blanker.

Figure 5.9 shows the schematic of the high speed blanker used in the experiment. The blanker was placed within the anode column between the thermionic source and the SEM column. The electron beam was deflected as they passed between the parallel plates of the blanker. The deflection was accomplished by connecting a high speed pulse generator to the deflecting plates in the anode. The negatively offset pulse supplied by the pulse generator and the response from the blanker, as detected by the Faraday Cup, can also be seen in Figure 5.9.

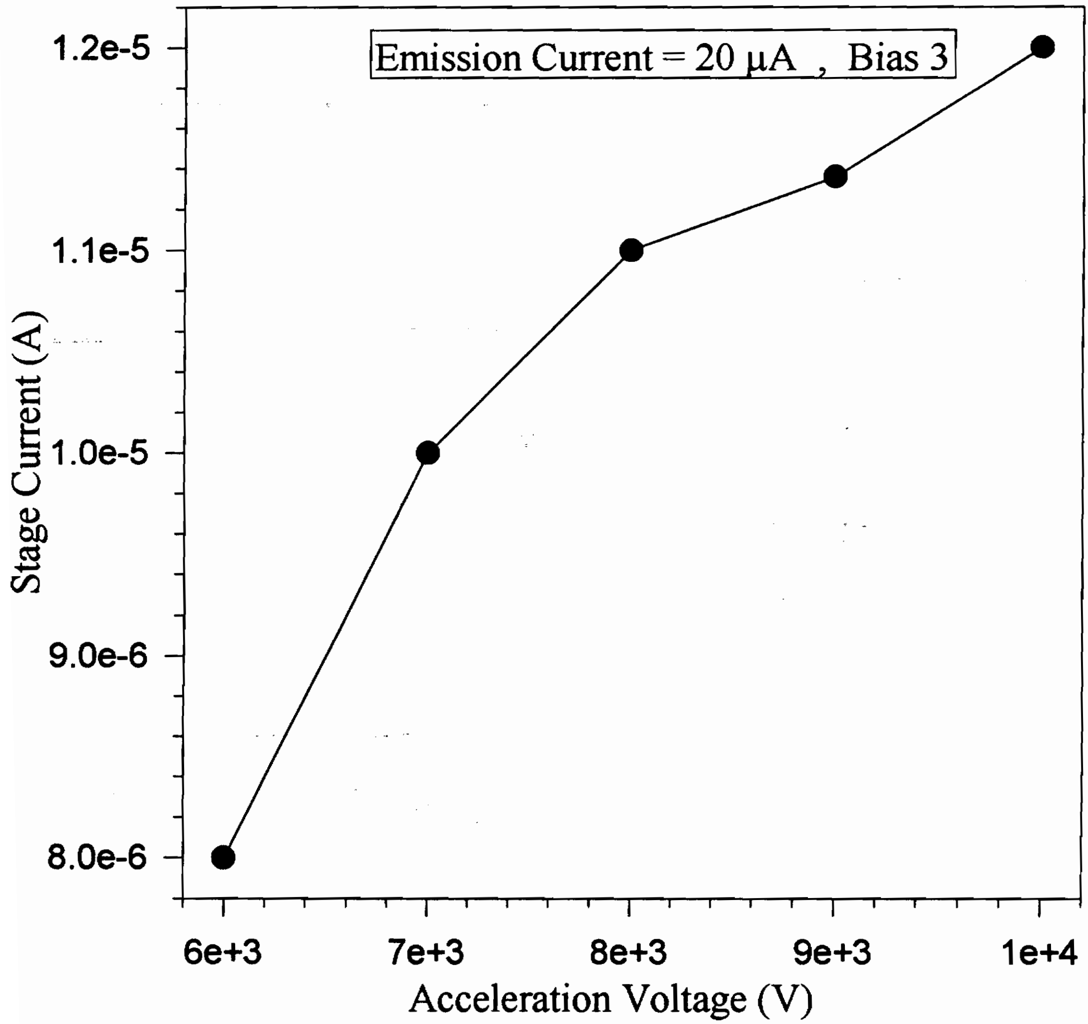

Figure 5.7. Stage Current vs Acceleration Voltage.

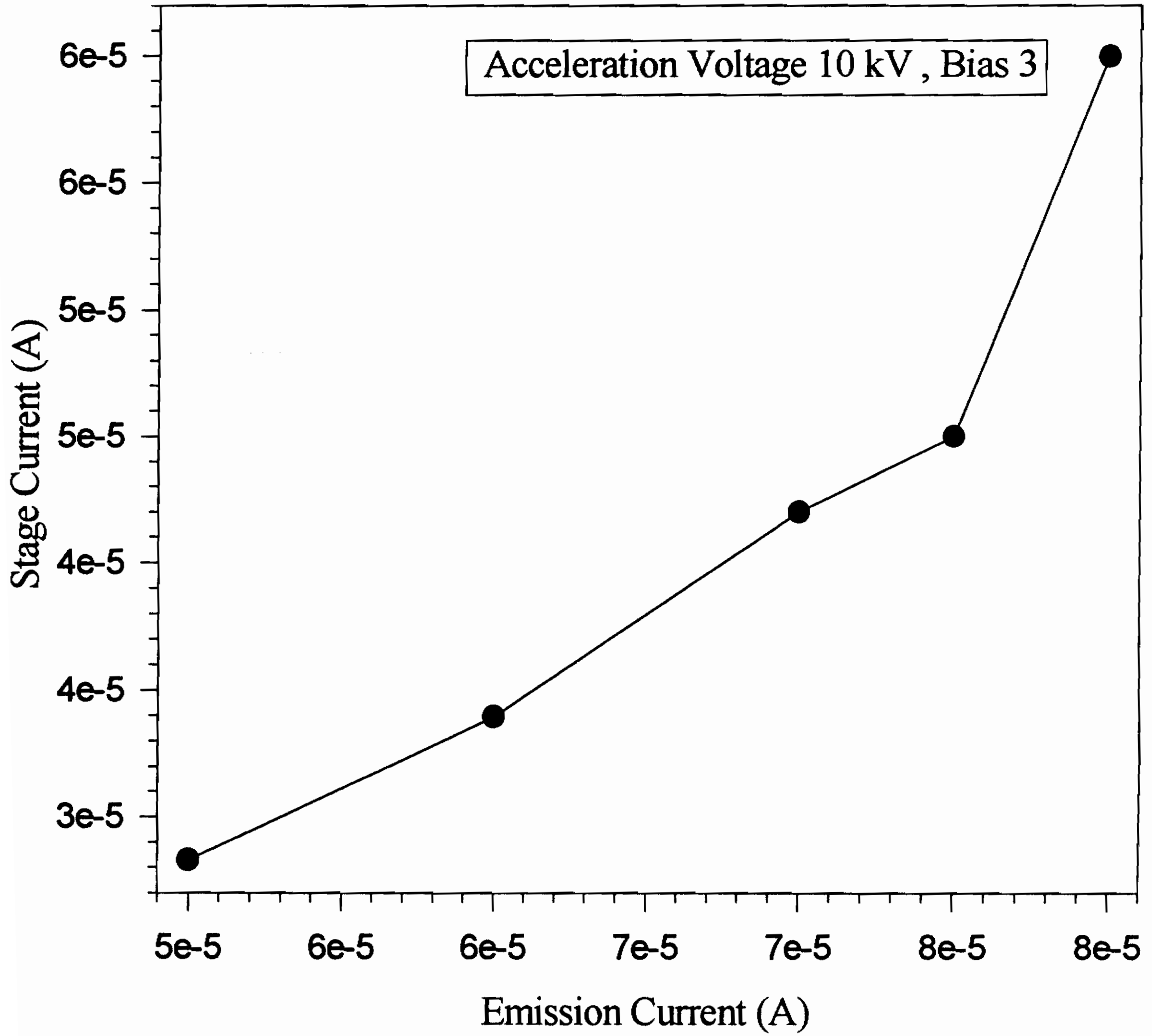

Figure 5.8. Stage Current vs Emission Current.

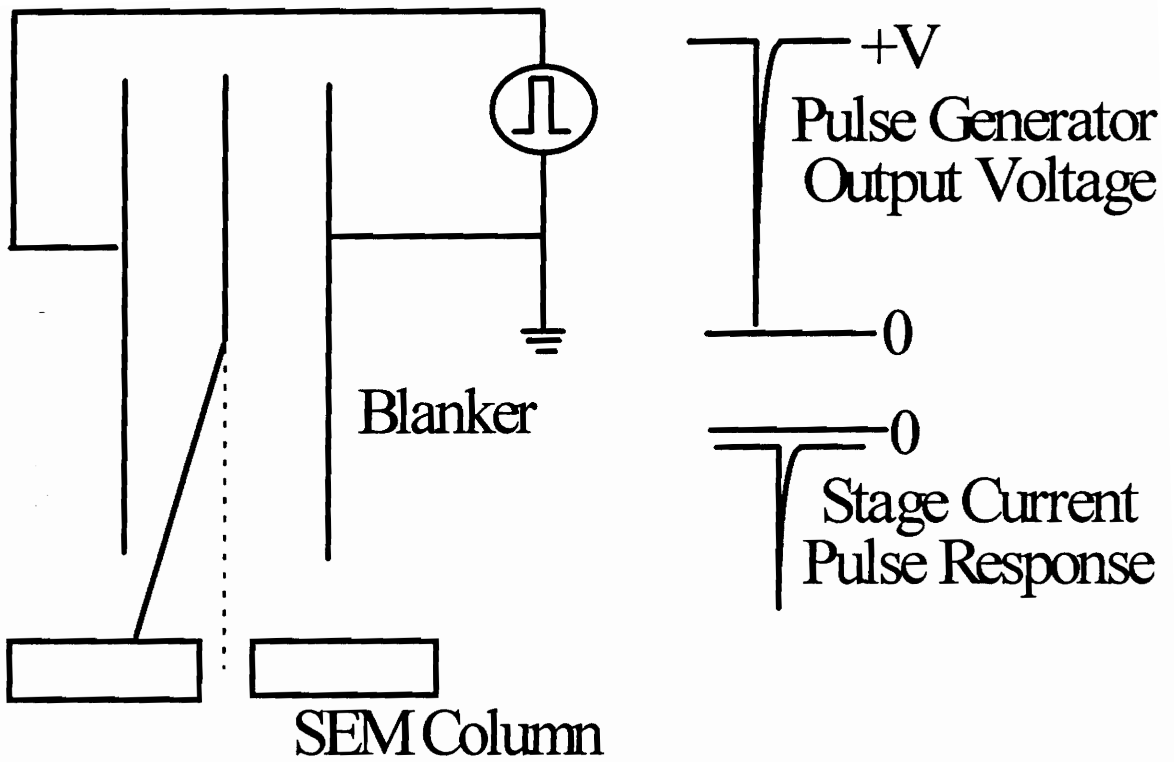

Figure 5.9. High Speed Blanker.

The required voltage necessary to completely turn off the electron beam was found by measuring the stage current, with respect to the applied voltage, across the parallel plates of the blanker. The results indicated that the emission current from the thermionic source, at applied acceleration voltage of 10 kV, was completely terminated at 20 V. The stage current versus the applied voltage at the blanker can be seen in Figure 5.10. Therefore, as shown in Figure 5.10, for the maximum allowable current to flow from the filament to the MUT, the bias voltage applied to the blanker must have a voltage in excess of 20 V with a 20 V swing. The pulse generator used was adjusted for a voltage swing of 20 V and offset by 20 V. Therefore, the only time the electron beam was allowed to travel to the MUT was when the signal at the parallel plates of the Blanker went to zero.

With all the components and equipment in place and calibrated, the EBIC systems were ready for testing. The system was first bench marked using the Si double ohmic device and then the diffusion length and carrier lifetime of Gallium Nitride and diamond was measured.

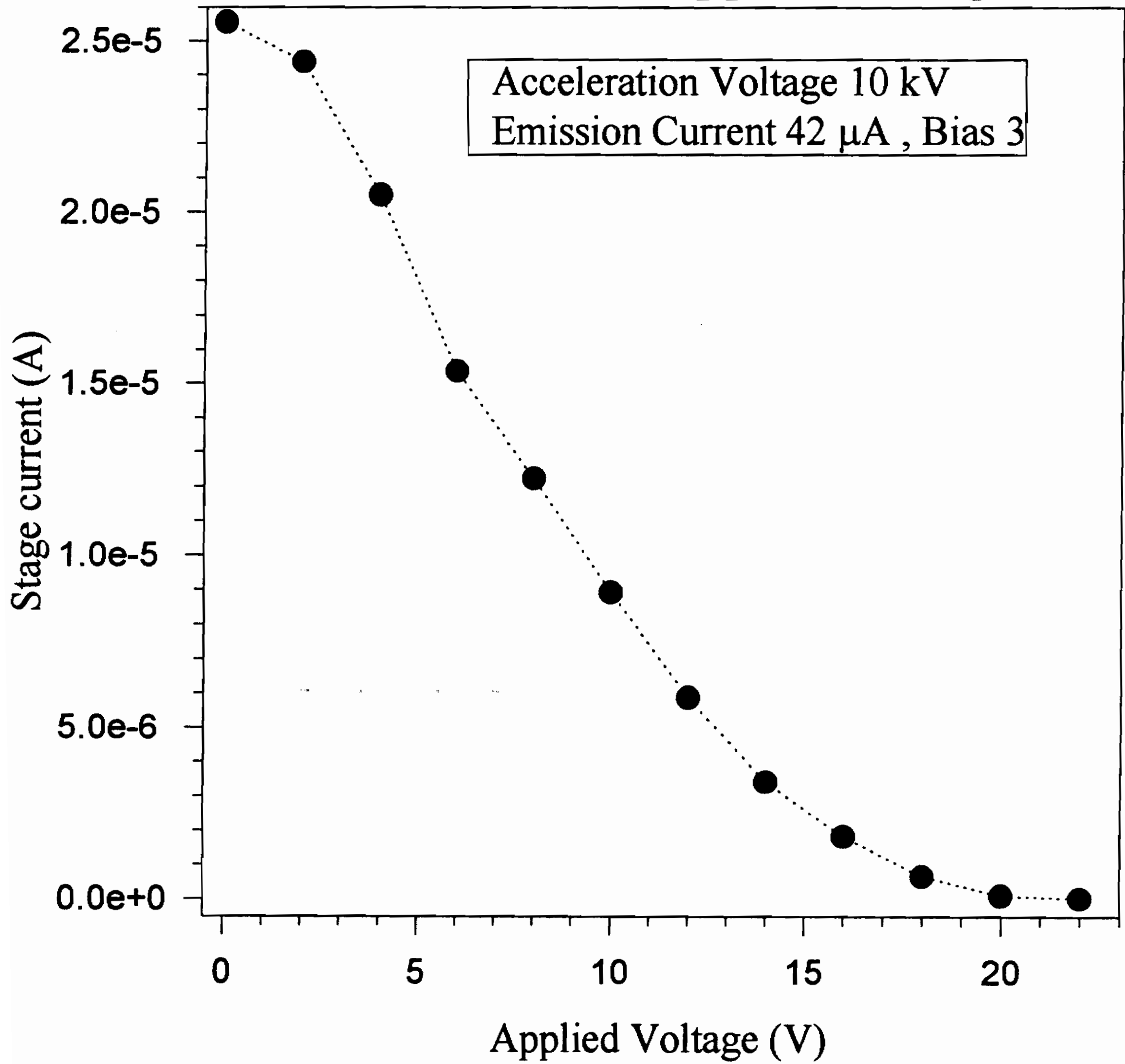

Figure 5.10. Turn-off Voltage of High Speed Blanker.

Chapter 6

Results, Discussion and Conclusion

6.1 Preliminary Evaluation
6.1.1 Si and GaAs
6.2 GaN Testing
6.2.1 OBIC Testing
6.2.2 EBIC Testing
6.3 Diamond Testing
6.3.1 EBIC Testing
6.4 Discussion of Results and Conclusion
6.4.1 Future Work
6.4.2 Summary and Conclusion

6.0 Results, Discussion and Conclusion

The chapters before examined and outline the requirements necessary for the extraction of the carrier transport properties in wide bandgap materials. Some of these requirements were materials with low dark current and high resistivity, the elimination of space charge effects, and the use of injected pulses much shorter than the transit time of the carriers in the material. Once these were in place, the determinations of the diffusion length, carrier lifetime and the dark resistivity were obtained by the combination of OBIC and EBIC techniques. This chapter describes the results of the experiments, with an explanation of some of the more interesting observations and comparisons with other work being performed in this area. In the final portion of the chapter, some discussion is given to the possible ventures that can be expanded from this research, followed by some concluding remarks.

6.1 Preliminary Evaluation

Before the actual testing of the wide bandgap materials could take place, the system was checked using Si and GaAs devices fabricated as described in section 4.2. These preliminary tests indicated the competence of the systems to generate electron-hole pairs within the devices and detect the drift/diffusion of carriers through the devices. This portion of the chapter describes the use of the Si double ohmic device to confirm the injection of electron-hole pairs in the T-EBIC system and observe the drift/diffusion of carriers through the device. Also described in this portion of the chapter is the use of the GaAs double ohmic device in evaluating the OBIC and the L-EBIC systems. The device was used to indicate a response to induced electron-hole pairs and observe the drift of

carriers at low electric fields. Further discussion of drift velocity can be found in Appendix A.

6.1.1 Si and GaAs Evaluation

The Si double ohmic was first sample tested in conjunction with the T-EBIC system. The device was mounted in the vertical test fixture, as shown in Figure 4.13 and aligned under high magnification in the modified SEM under vacuum. The current voltage characteristics were taken without any excitation to the device. This was performed to obtain the dark current flowing through the device. The results indicated that at an applied voltage of -24 V the dark current was -328 μA. At an acceleration voltage of 10 kV, with filament bias 3 and an emission current of 50 μA, the device was exposed to the electron beam and the current voltage characteristics were taken again. The resulting photoinduced response showed that at -24 V the photoinduced current was approximately 590 μA, which was an increase of approximately 262 μA. This indicated that the T-EBIC system was capable of generating excess carriers within the material.

The device was also used to obtain a rough estimate of the diffusion length in Si. This was performed to verify that the system was capable of measuring the photoinduced current with respect to distance across the device. Under the same conditions as described above, except for zero bias across the sample, the device was exposed to a constant electron beam at a particular location, and the photoinduced current was measured. The electron beam was turned off and the device was moved to a new location, after which the device was exposed to the electron beam again. The process was continued until the entire width of the device was covered.

The data taken from the photoinduced current with respect to distance across the device was applied to equation 2.69 and the diffusion length extrapolated. The results of

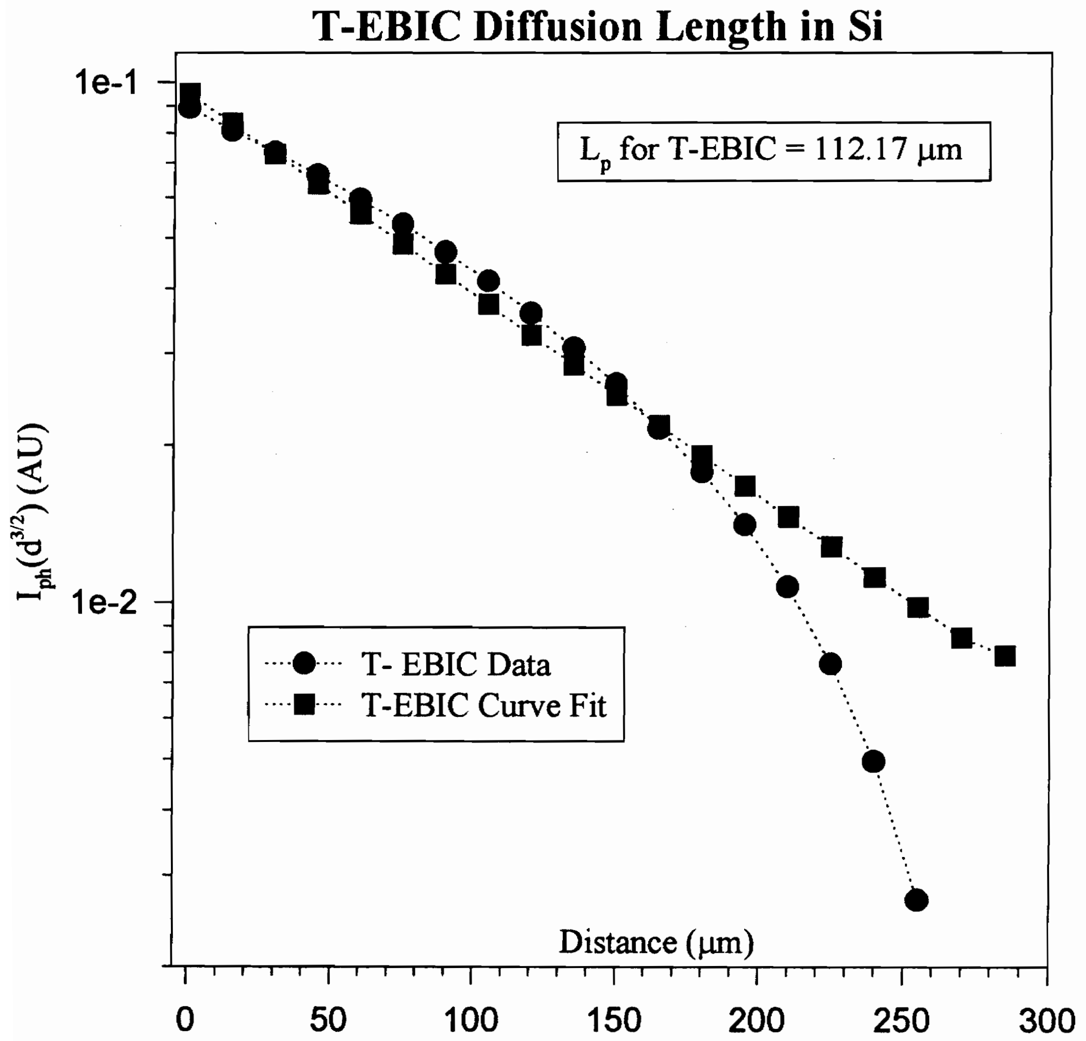

Figure 6.1. Diffusion Length for Silicon.

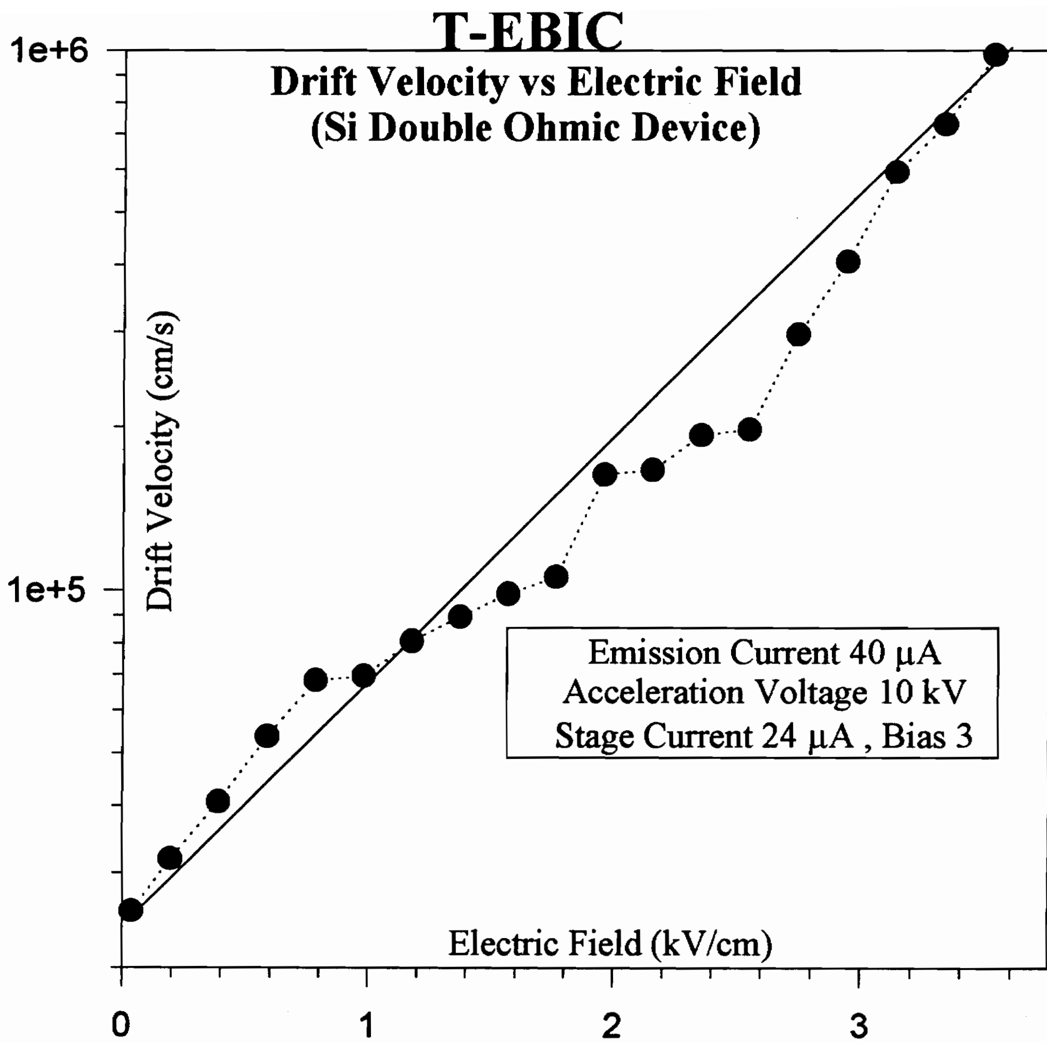

Figure 6.2. Si Double Ohmic Testing of Drift Velocity vs Electric Field.

the diffusion length can be seen in Figure 6.1. The diffusion length obtained from the double ohmic device for Si was approximately 112 μm. Zimmermann[54] using an T-EBIC system found $L_p \approx 198$ μm. Although the theoretical diffusion length for intrinsic material ranges from a few microns to tenths of a millimeter depending on the inherent impurities, the results were quite reasonable, because of the highly compensated nature of the wafer used.

The device was also used to observed the transient response in the T-EBIC system. In this case the pulsed electron beam was applied to the device when a low electric field region (less than 3 kV/cm) was applied across its terminals. Further discussion on the drift velocity with respect to the electric field, used in an EBIC system can be found in Appendix A. During the experiment the emission current was set to 40 μA at bias 3, the acceleration voltage of the electron beam was 10 kV and the stage current before and after the data was taken was 24 μA. The results can be seen in Figure 6.2. These results were approximately an order of magnitude lower than those reported by Sze[55] for intrinsic Si and by Canali et al.[56] for T-EBIC. The hole mobility obtained from the data was approximately 382.53 cm^2/V-s ± 20%. The mobility value in Figure 6.2 is represented by the straight line and was a bit lower than the expected value 450 cm^2/V-s for holes. However, the data taken was very encouraging since the wafer used was highly compensated. The overall results indicated that the T-EBIC system was indeed capable of not only generating electron-hole pairs, but also observing the drift/diffusion of carriers through any highly resistive device.

The GaAs double ohmic device was used to test the effectiveness of the OBIC and the L-EBIC system in generating electron-hole pairs and observing the transient response of excess carriers. For the L-EBIC system, the GaAs device was first assembled in the vertical test fixture and mounted into the modified SEM. Under high vacuum and with no excitation, the dark current was measured by sweeping the voltage from -100 V to 100 V and monitoring the current. At -80 V the dark current was -619 nA. The laser was turned on and adjusted to produce a third harmonic of 30 mW. The resulting stage

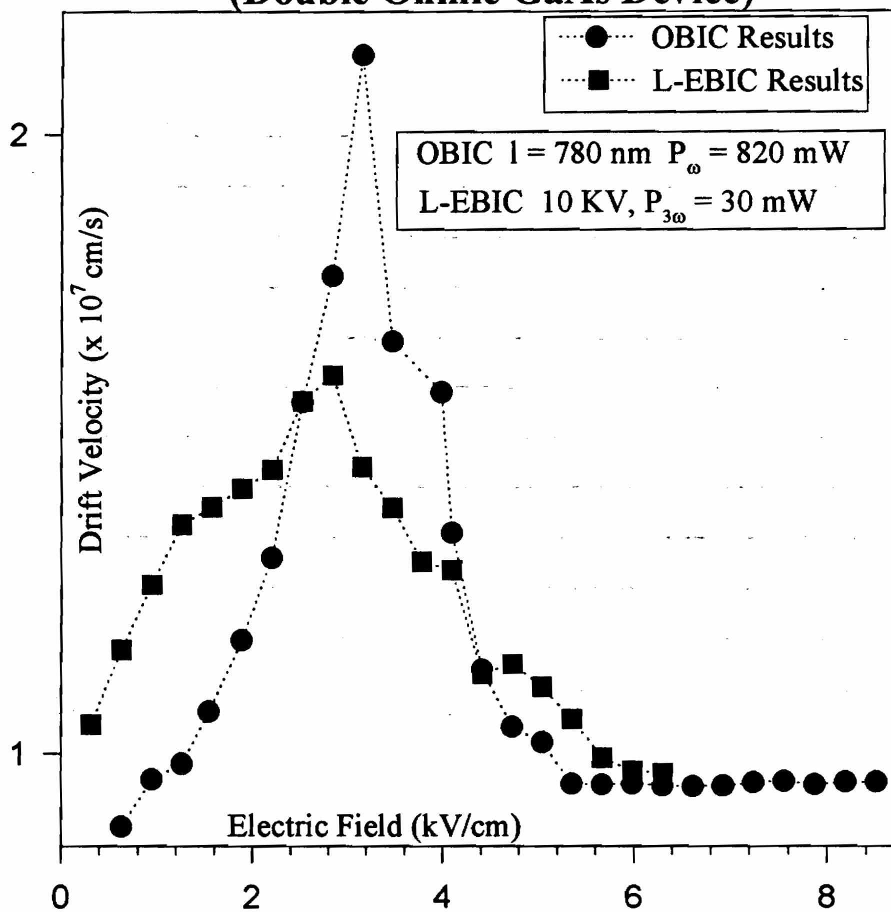

Figure 6.3. GaAs Double Ohmic Testing of Drift Velocity vs Electric Field.

current for an acceleration voltage of 10 kV was 15 nA. The device was aligned and exposed to the pulsed electron beam. The photoinduced current was measured for a voltage sweep over the same range and for a value of -80 V the net current was -3.23 μA. The photoinduced current produced from the generation of electron-hole pairs was 2.61 μA. This successfully proved that the L-EBIC system was capable of generating excess carriers.

The transient response of the excess carriers in the L-EBIC system was detected by applying a bias across the device. The applied bias created an electric field that corresponded to the region in the drift velocity electric field curve where the peak occurs (i. e. between 2 to 4 kV/cm). The plot of this response can be seen in Figure 6.3. The same device was used to obtain the drift velocity electric field curve in the OBIC system. The laser operating conditions for this experiment was a wavelength of 780 nm with a power of 820 mW. The results from OBIC system can also be seen in Figure 6.3. Both of these curves generally agreed with data reported by Sze[(55)] for high purity GaAs and by Evans et al.[(57)] for Microwave-EBIC system. The L-EBIC results were much closer to those reported by Evans although they were slightly lower than the OBIC. The general characteristics of the curves were similar indicating that both the L-EBIC and OBIC systems were capable of generating and observing electron-hole pairs within highly resistive device.

6.2 GaN Testing

Before the carrier transport data was taken the GaN was tested to ensure that the dark current was sufficiently low as to not interfere in the measurement of the induced response of the excess electron-hole pairs. The current voltage characteristics were observed under vacuum in the modified SEM. The dark current for all the samples was

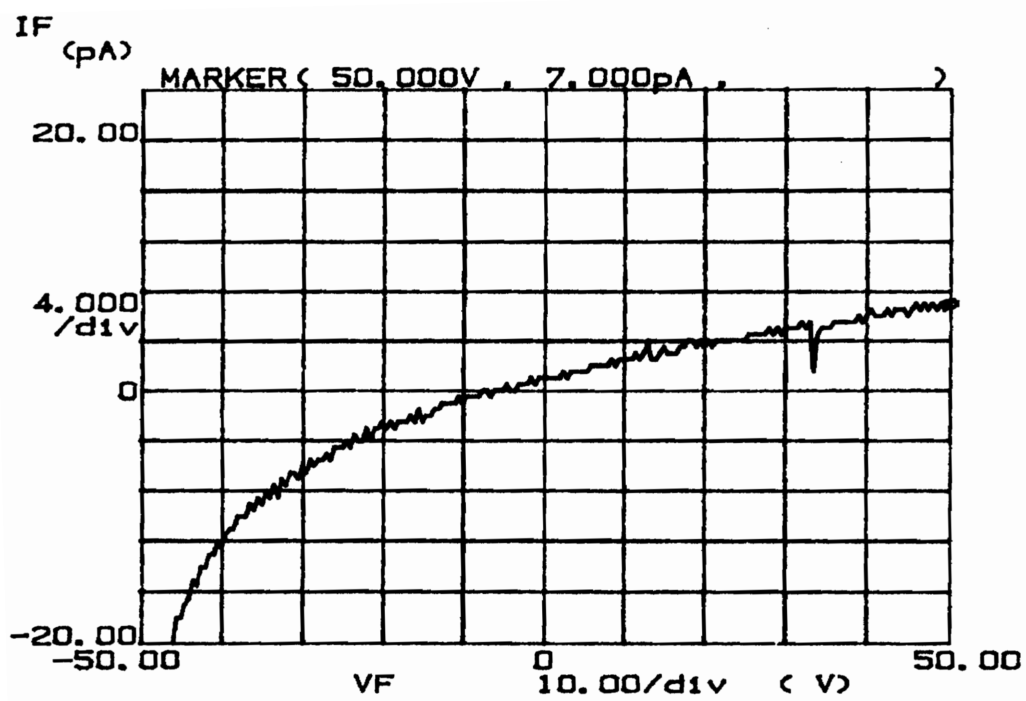

Figure 6.4. Dark Current for GaN Sample.

measured using the HP 4145 parameter analyzer. For the spiral ring and interdigitated fingers structures the dark current for the negative bias regions exhibited anomalous behavior, however the positive bias region exhibited extremely low dark currents in the pico-Amp. range.

The reason for the anomalous behavior is not quit known, but is suspected to be due to the contacts. The larger the size of the contact, the lesser the anomalous behavior in the negative bias region and the more linear the dark current characteristics. The 25 μm spacing transmission line produced the lowest dark current response and exhibited less of the anomalous behavior in the negative bias region. Figure 6.4 shows the dark current for the 25 μm spacing transmission line configuration.

From the dark current and the distance of separation between the contacts, the dark resistivity was calculated. For the 25 μm spacing transmission line structure the dark resistivity was 1.79×10^{10} Ω-cm[58,59], for the 3 μm interdigitated fingers structures the dark resistivity was 3.53×10^{8} Ω-cm and for the 48 μm spaced spiral ring the dark resistivity was 4.09×10^{6} Ω-cm. The results of the current voltage characteristic test showed that the samples being used had low dark currents that would not interfere in the detection of the excess carriers.

After calibration was completed the systems were ready for testing of the wide bandgap materials. The first to be tested was the 25 μm spacing transmission line GaN sample. The diffusion current was measured with respect to distance across the sample, in hopes of verifying that these samples did indeed perform as predicted by their theoretical calculations. Both the L-EBIC and the T-EBIC were used to obtain these measurements. The sample was mounted into the Modified SEM and with an acceleration voltage of 10 kV and a primary current or stage current of 1 nA used in both systems, the results can be seen in Figure 6.5.

The results indicated that the measured T-EBIC data was within 20 % of the theoretical values at all times except at the measuring contact. At this point the deviation was as high as 61 %. This behavior was also seen with respect to the L-EBIC data which

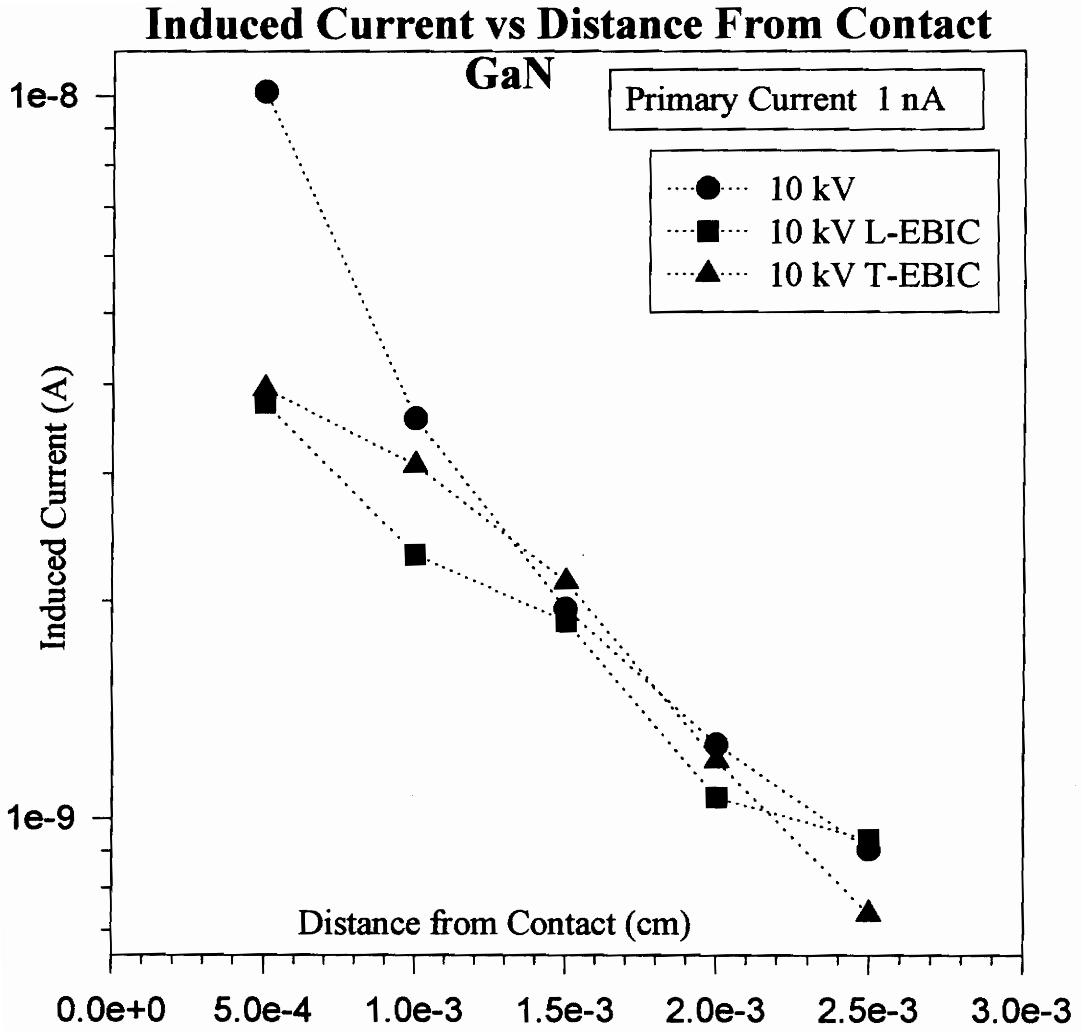

Figure 6.5. Comparison between Theoretical & Measured Diffusion Current.

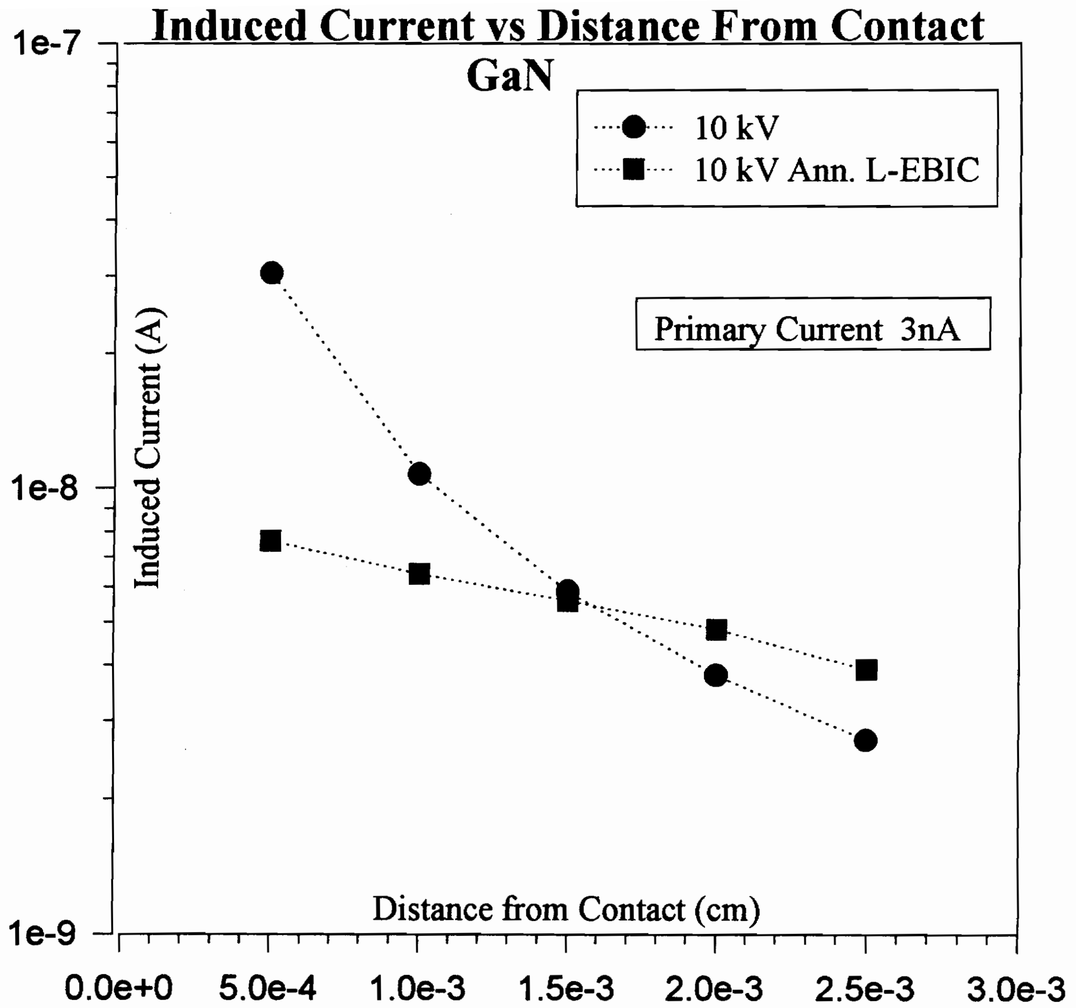

Figure 6.6. Comparison of Theoretical & Measured Diffusion Current after Annealing.

was 62 % at the same point. In the hopes of eliminating this problem the GaN sample was annealed for 15 minutes at 90 ^{O}C and then tested again in the L-EBIC system. The results of the diffusion current as a function of distance for the annealed sample can be seen in Figure 6.6. The test was performed at the same 10 kV acceleration voltage and with a primary current of 3 nA. The results however did not show any improvements. The deviation was up to 74 % at the measuring contact and 40 % along the rest of the plot, except at the center point that stayed the same as before. The belief here is that by annealing, the inherent impurities in the substrate were removed from the center region between the contacts. However under the Al/Ti contacts, the impurities were drawn up to the layer under the contacts and trapped.

Most of the impurities were believed to have occurred from damage done to the material during the deposition of the Al/Ti contacts onto the GaN substrate(1). These impurities were most likely the ones trapped in the immediate layer under the contact as a result of the annealing process. Other problems that occurred with the samples were, dark spots appeared on the surface and the Al/Ti metallization oxidized after long hours of usage. However the results of the diffusion current test showed that the samples did produced significant amounts of induced current to be used to obtain the carrier lifetimes and diffusion lengths.

6.2.1 OBIC Testing

The GaN 3 μm spaced interdigitated finger structure was used to obtain the transient response to optical excitation. The sample was assembled in the horizontal test fixture for OBIC experiments as shown in Figure 4.2. The Titanium:Sapphire laser was tuned to 640 nm and the resulting second harmonic was 320 nm. This wavelength was equivalent to 3.449 eV which was slightly larger than the bandgap of GaN (3.4 eV).

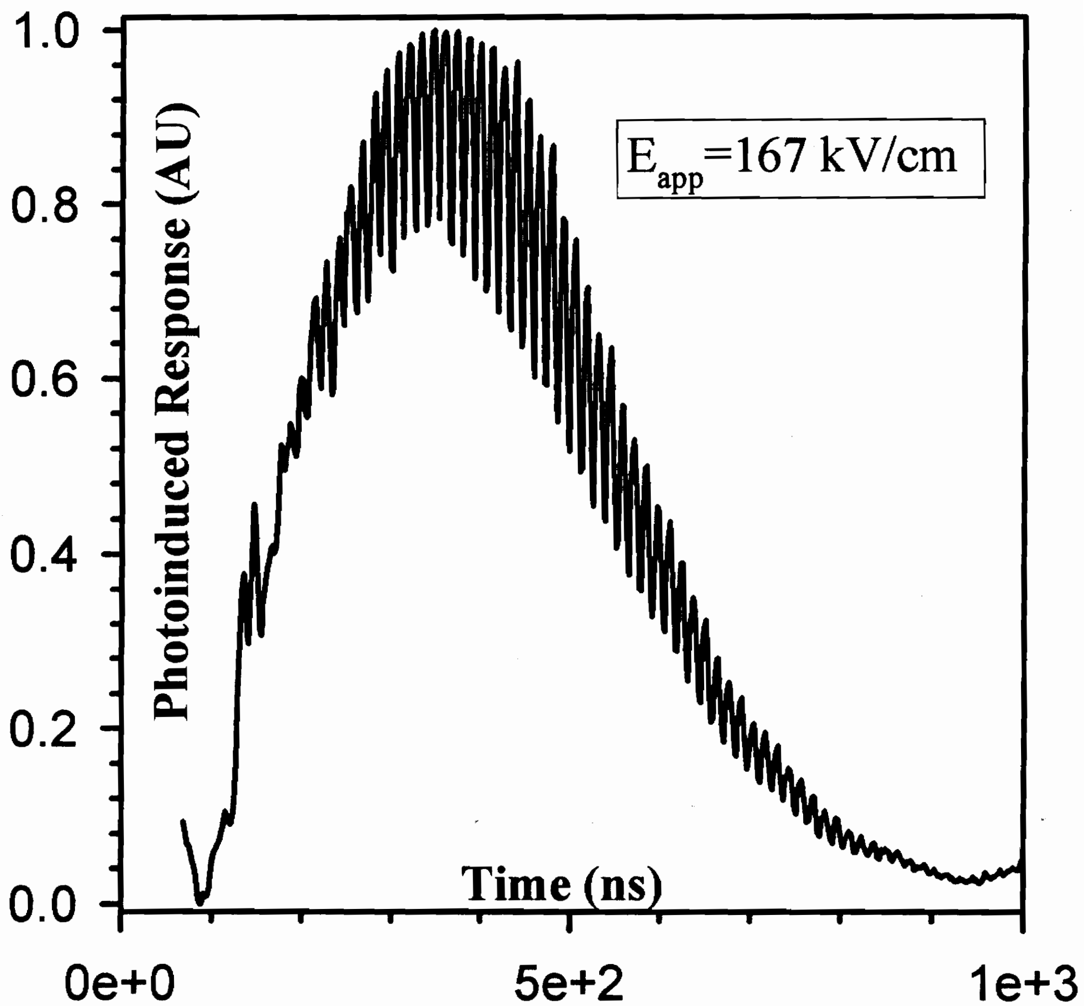

Figure 6.7. Photoinduced Response of GaN in OBIC System.

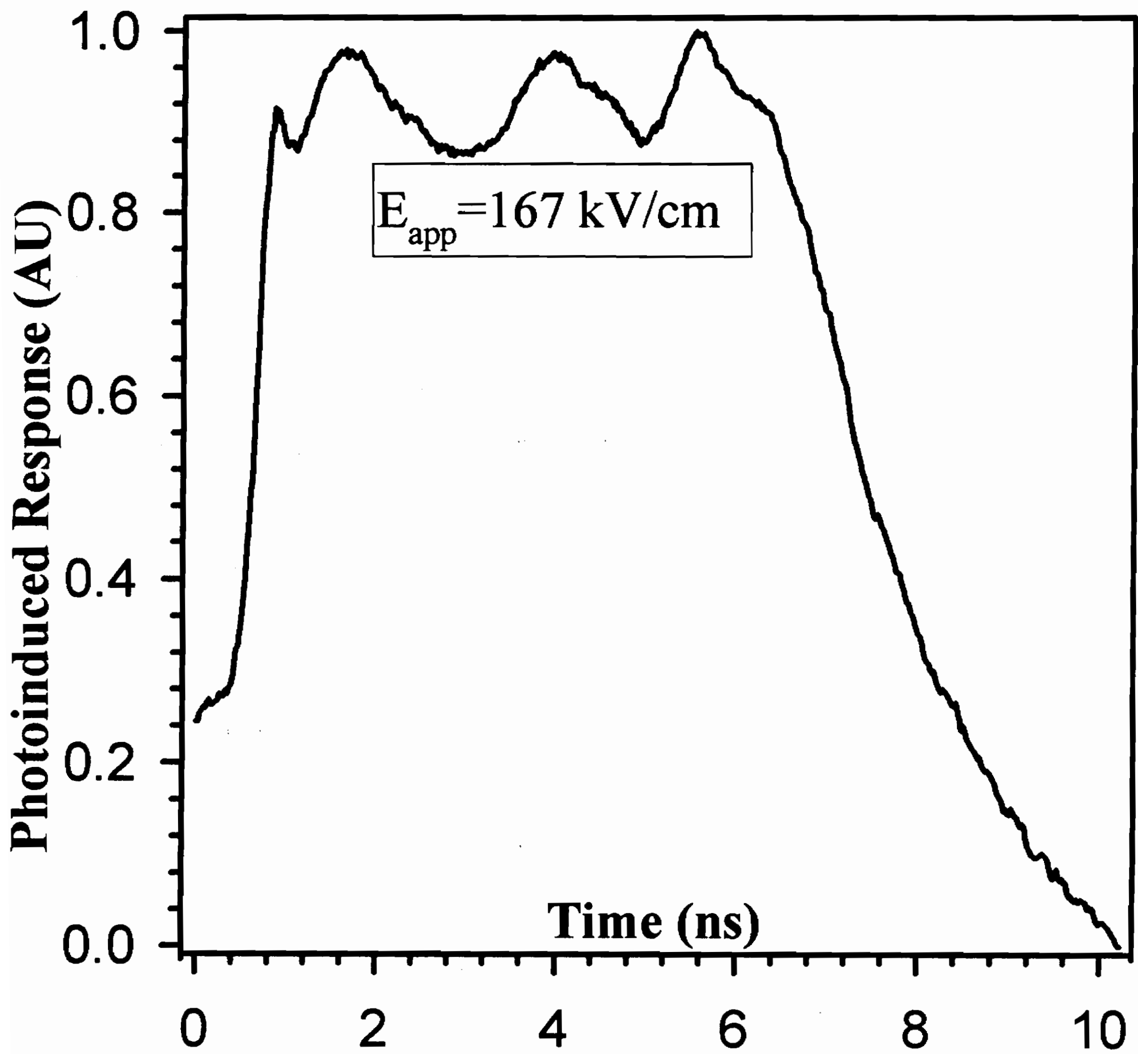

Figure 6.8. Expanded View of GaN Photoinduced Response under OBIC.

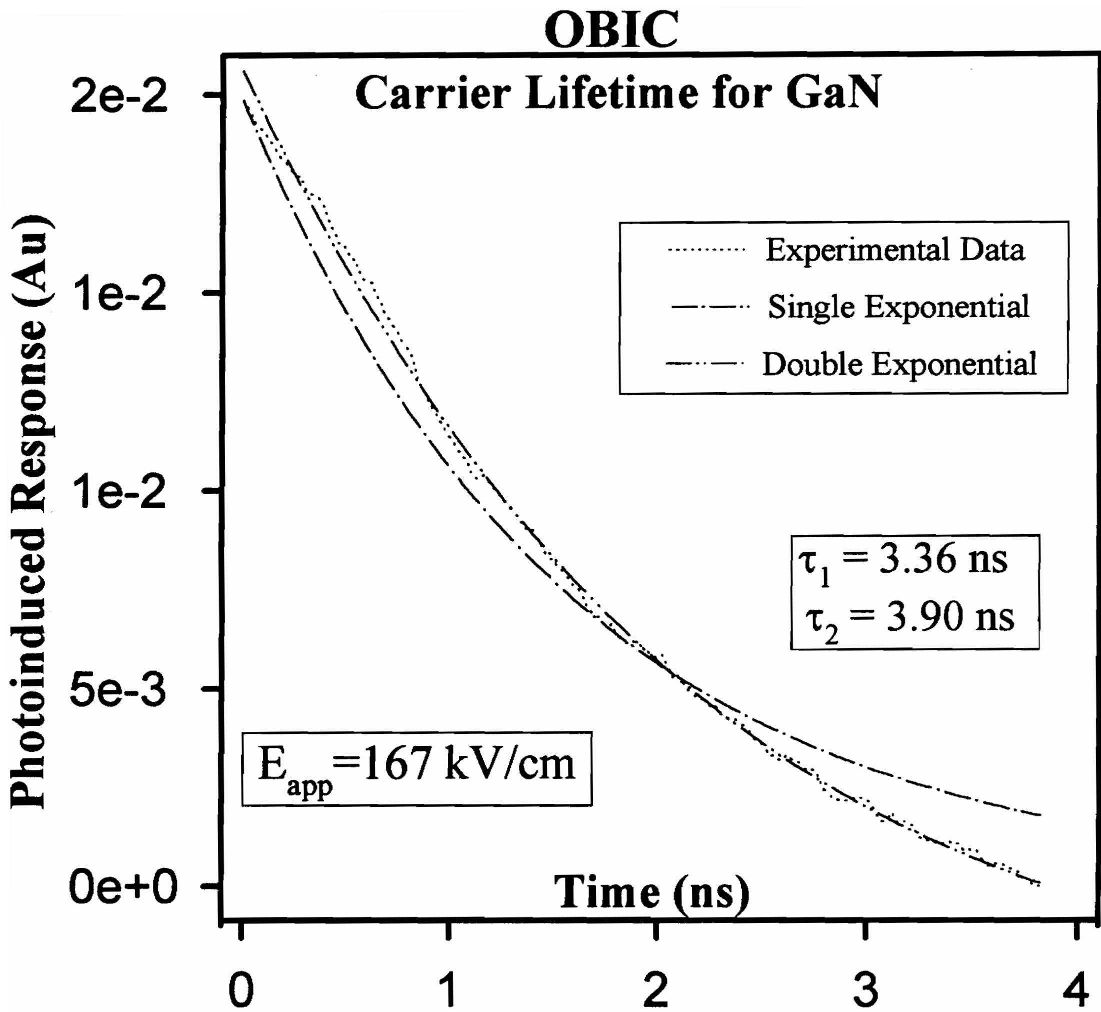

Figure 6.9. Extracted OBIC Carrier Lifetime for GaN.

Therefore most of the energy incident on the sample should be absorbed and generate excess carriers. Since the sample spacing between the contacts was only 3 μm and the diameter of the incident blue light was 4 μm, only time constant information was extracted (carrier lifetime). The applied voltage across the contacts was 50 V and this gave an applied electric field of 167 kV/cm in a 1 μs pulse width.

The photoinduced response for an applied field pulse width can be seen in Figure 6.7. In this figure the high frequency laser pulses are shown superimposed onto the applied field pulse response. These pulses repeat themselves approximately every 13 ns. Figure 6.8 shows an expanded view of the photoinduced response near the maximum portion of the field pulse response curve. Here the high frequency laser pulse width can clearly be seen to be on the order of 13 ns. The cusps at the top of the response were believed to have formed partially from the multiple reflection of the light within the GaN layer.

The absorption depth calculated from Comphausen and Connell[(60)] absorption coefficient of GaN at 320 nm for 90 % absorption was 4.6 μm. This indicated that the light reached the GaN/sapphire interface. The net result of this condition was an oscillation of the light within the GaN layer leading to the build up of excess carriers, for the duration of the pulse. The trailing portion of the photoinduced response in Figure 6.8 was fitted to a single and double exponential function. The results can be seen in Figure 6.9.

The single exponential time constant curve was found to be 20.1 ns, but the fit was not very accurate. The better exponential fit was found from the double exponential function. The resulting time constant was 3.36 ns and 3.9 ns[(58,59)]. These results predicted a multiple recombination process tacking place. The effective drift lifetimes for these results were due to the combine surface, interface and bulk recombination processes of GaN materials.

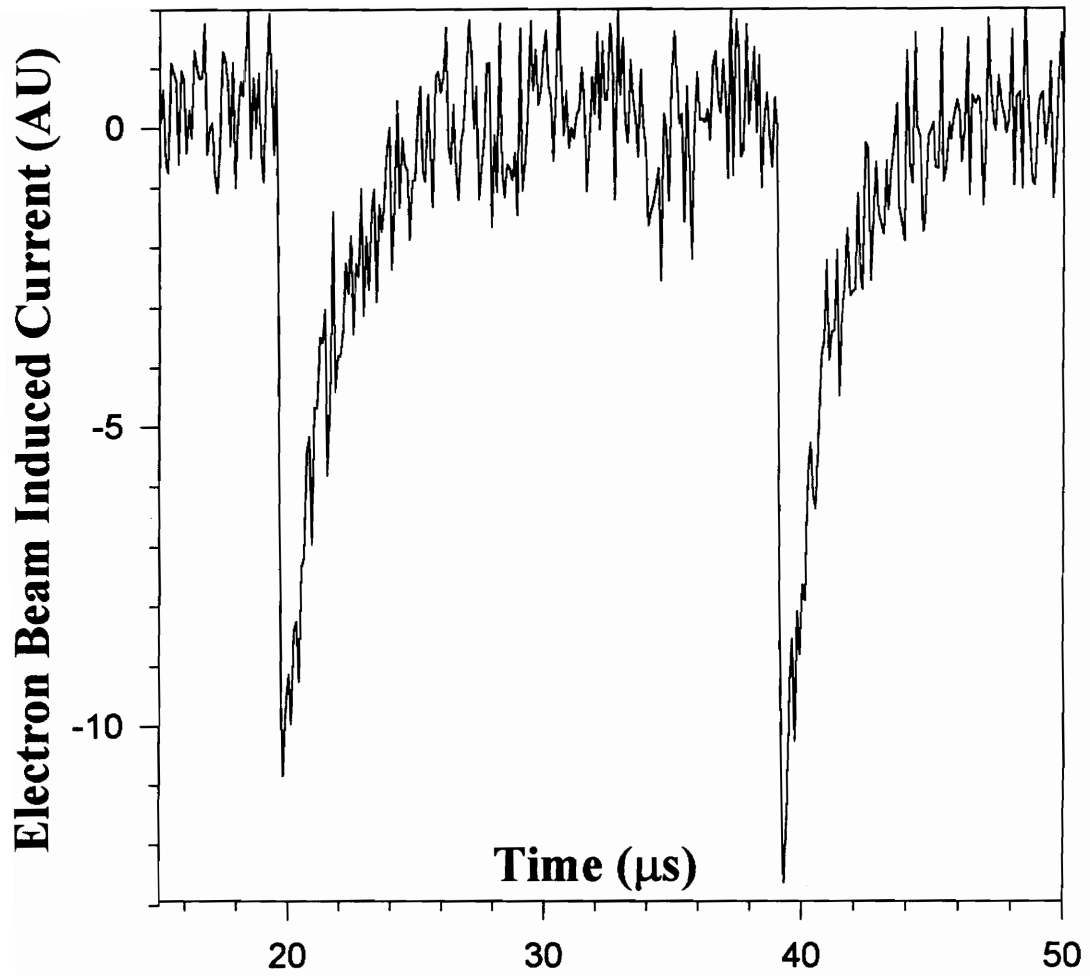

Figure 6.10. GaN Transient Response to L-EBIC in Raster Mode.

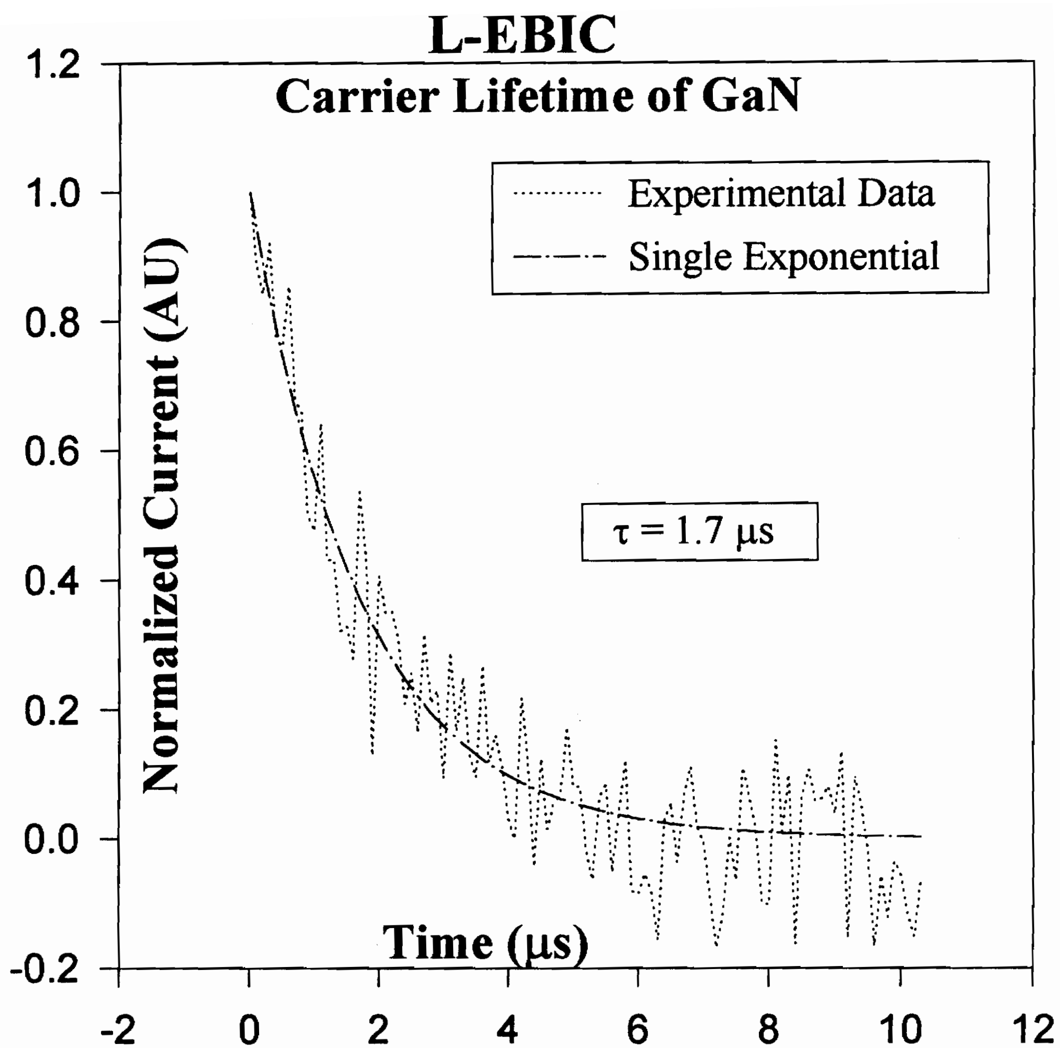

Figure 6.11. L-EBIC Carrier Lifetime for GaN.

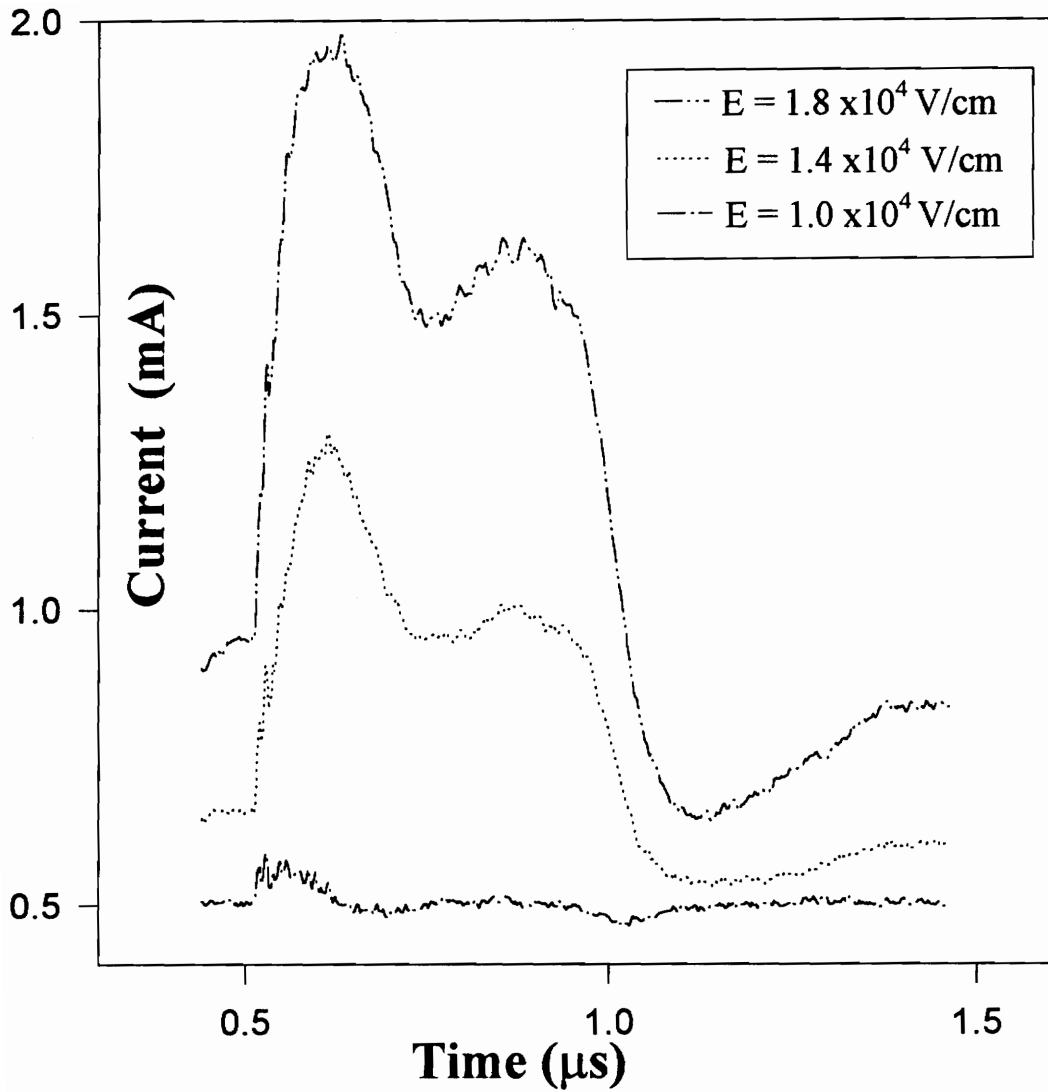

Figure 6.12. GaN Transient Response for Various Electric Fields in L-EBIC.

6.2.2 EBIC Testing

The GaN 25 μm spaced transmission line structure was used to obtain the transient response to electron beam excitation. The sample was mounted in the modified SEM and both the effective carrier lifetime and the diffusion length were measured. In the L-EBIC system the effective carrier lifetime was measured by scanning the electron beam across the sample in a raster mode, with no field applied and an acceleration voltage of 10 kV. This process slows down the rate at which the electron beam moves across the sample, to that of the raster frequency.

The raster period was observed to be on the order of 20 μs as shown in Figure 6.10. As the electron beam moves across the sample, the only time a transient response was detected, was when the electron beam interacts with either the contacts or the sensitive space between the contacts. As the electron beam leaves the last contact there was a sudden drop in injected carriers, therefore the response shows the recombination of the last few injected excess carriers. From this information the effective carrier lifetime can be obtained. Fitting the decay portion of the electron beam induced response, the effective carrier lifetime was obtained to be on the order of 1.7 μs(58,59). Figure 6.11 shows the fitted effective carrier lifetime for GaN sample tested in the L-EBIC system.

The effective carrier lifetime measured from the L-EBIC system was considerably longer than that of the OBIC system. This was expected because the penetration depth of the EBIC system was on the order of 0.4 μm. This penetration depth was well away from the high recombination centers at the surface and interface regions of the GaN layer. Therefore the EBIC results are a good representation of the effective thin film carrier lifetime in the GaN material.

An electric field was applied across the sample and the electron beam induced transient response can be seen in Figure 6.12. The response showed no high frequency characteristic transient pulse superimposed on the field as in the OBIC system. The

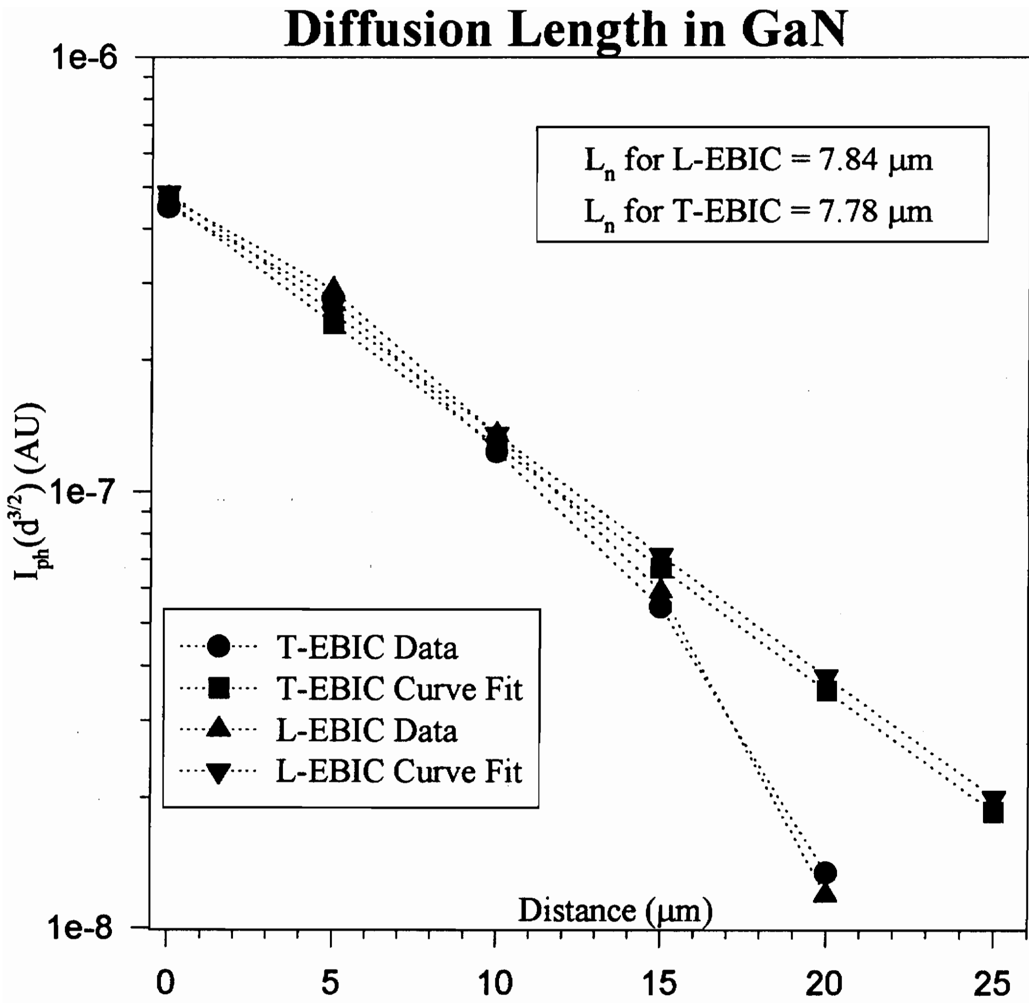

Figure 6.13. Diffusion Length in GaN for T-EBIC and L-EBIC.

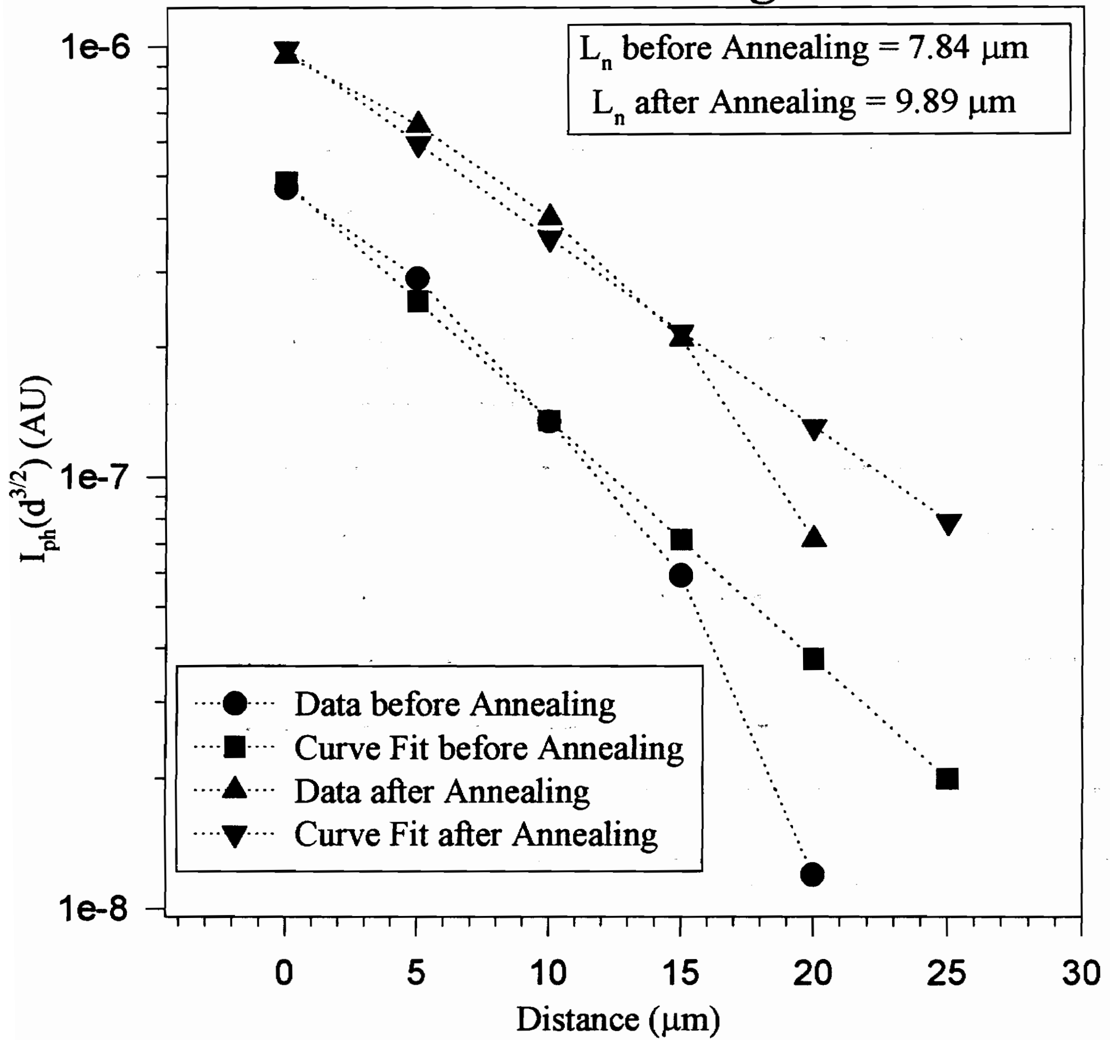

Figure 6.14. GaN Annealed & Non-Annealed Diffusion Length.

electron beam induced current response was greatly diminished when the electron beam was blocked, indicating an ample amount of excess carriers being generated. The reason for the lack of temporal resolution was due to the build up of excess carriers as described in the section on spacecharge effects.

The same sample was also used to obtain the diffusion length of the GaN material. In the T-EBIC system the sample was exposed to constant electron beam at a particular location, and the photoinduced current was measured. The sample was moved to a new location after the electron beam was terminated and the process was continued again until the entire sensitive region of the sample was covered.

The data taken from the photoinduced current with respect to distance across the sample was used in equation 2.69 to extrapolate the diffusion length. The diffusion length was extrapolated by curve fitting the data of $\ln(I_{ph}d^{3/2})$ versus d, where I_{ph} was the photoinduced current and d was the distance between the contacts. The results of the diffusion length for an acceleration voltage of 10 kV and primary current of 1 nA, can be seen in Figure 6.13. The diffusion length obtained from the curve fit of the data for the T-EBIC system was 7.78 μm ± 8 %(58,59).

The same sample was applied to obtain the diffusion length from the L-EBIC system under the same conditions. Figure 6.13 shows the results of the diffusion length for an acceleration voltage of 10 kV in the L-EBIC system. The diffusion length obtained from the curve fit of the data for the L-EBIC was 7.84 μm ± 5 %(58,59).

In hopes of improving the diffusion length, the GaN sample was annealed for 15 minutes at 90 ^{O}C and then tested again in the L-EBIC system under the same conditions as before. Figure 6.14 shows the results of the diffusion length for the annealed sample in the L-EBIC system. The diffusion length obtained for the annealed sample in the L-EBIC was 9.89 μm ± 8 %(58,59). The results showed an increase in the diffusion length, indicating that some of the inherent impurities of the GaN material were removed from the sample during annealing.

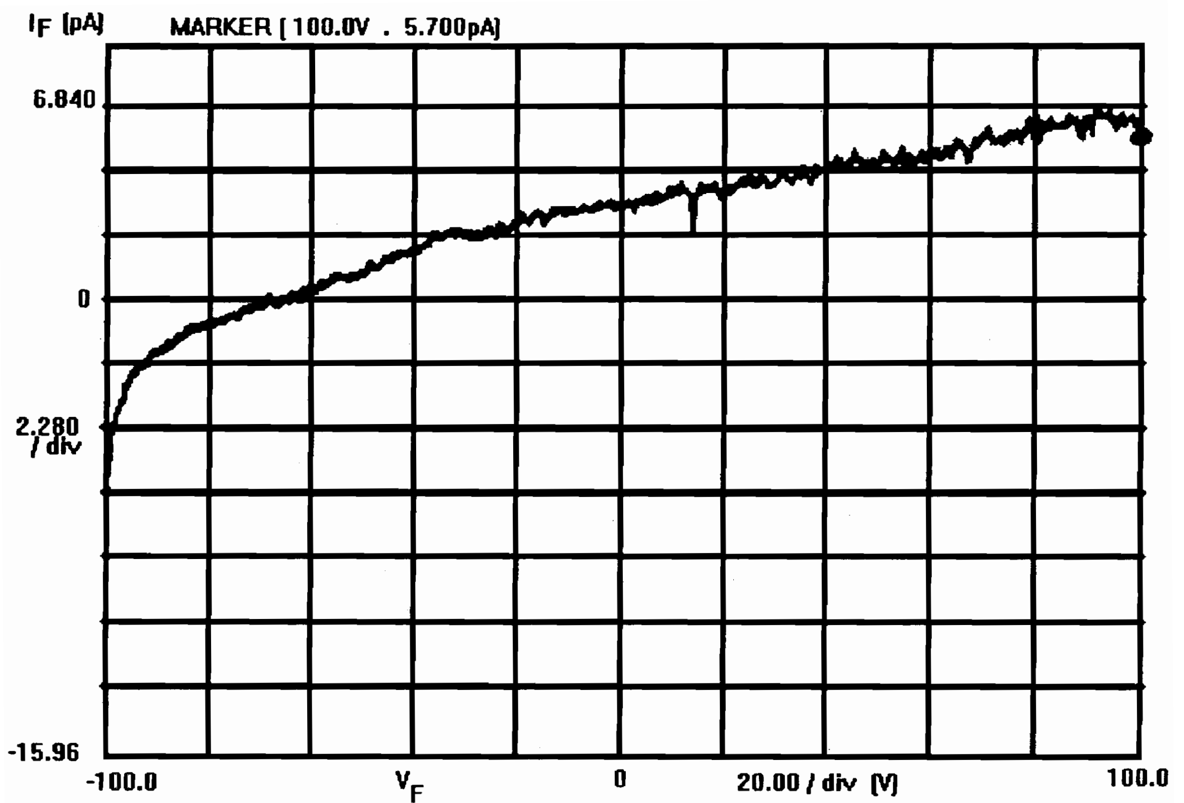

Figure 6.15. Dark Current for Type IIa Natural Diamond.

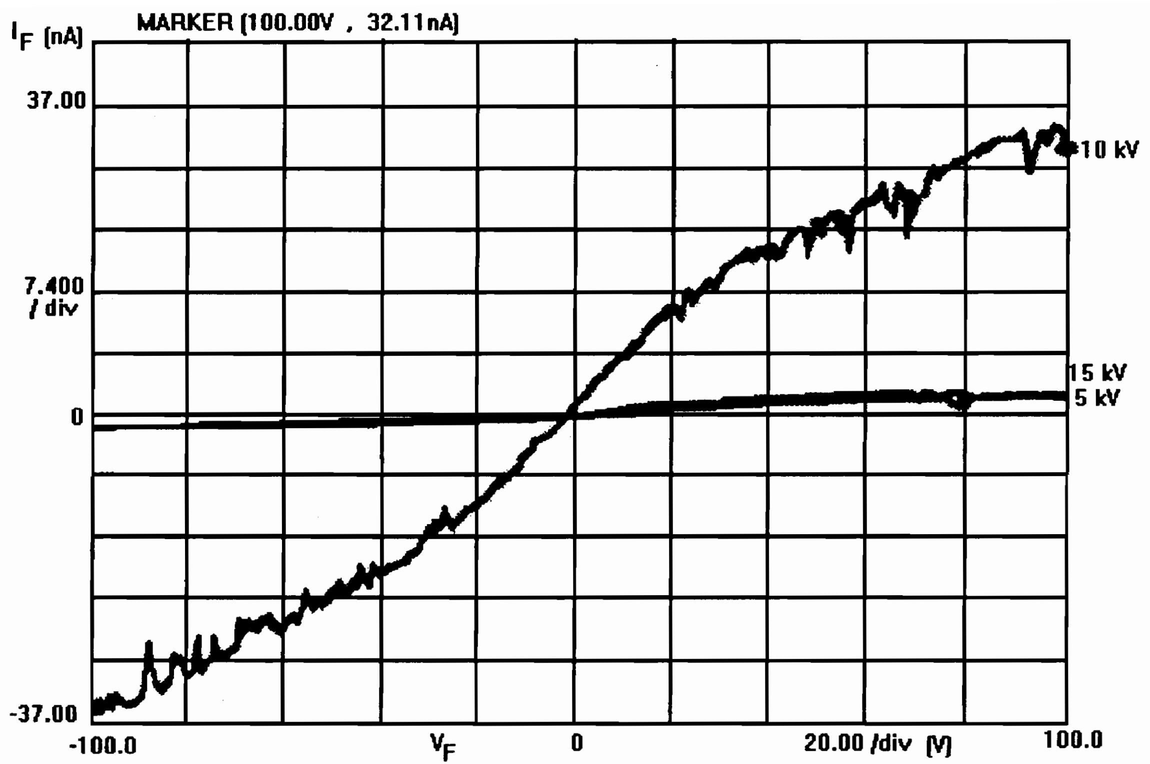

Figure 6.16. Induced Current in L-EBIC for Type IIa Natural Diamond as a Function of Acceleration Voltage.

6.3 Diamond Testing

Along with the GaN material, type IIa natural diamond was the other material used in the test of the carrier transport properties of wide bandgap materials. In order to use the diamond material in the system, the sample's dark current was evaluated to ensure that the material was indeed highly resistive. The current voltage characteristics were observed under vacuum in the modified SEM. The dark current for the samples was measured using the HP 4145 parameter analyzer.

The current voltage characteristics were obtained by sweeping an applied voltage to the contacts from -100 V to 100 V and monitoring the current response. This was performed with no excitation to the sample. The dark current obtained from the type IIa natural diamond can be seen in Figure 6.15. This dark current value was the lower of the two wide bandgap materials tested. From the data of the dark current the dark resistivity was calculated. For a 350 μm spacing between the contacts and a dark current of 5.7 pA for an applied of 100 Volts, the dark resisitivity was found to be 6.14×10^{11} Ω-cm[58,61,62]. The results of the current voltage characteristic test showed that the type IIa natural diamond sample being used had an extremely low dark current and would be effective in detecting any excess carriers generated.

The sample was then exposed to an electron beam produced from the L-EBIC system. Varying the accelerating voltage, the current voltage characteristic was monitored. The results in Figure 6.16 show that the electron beam induced current increased with decreasing acceleration voltage from 15 kV to 10 kV. Upon further decrease in acceleration voltage, from 10 kV to 5 kV, the electron beam induced current decreased. This indicated that the optimum acceleration voltage for the induced current was at 10 kV.

This was mainly due to the number of generated carriers as a function of electron range, as discussed in section 2.3.1 and 3.2.2. At high acceleration voltages the electron penetrates deeply into the material (Figure 2.7) and so avoids the high recombination

velocity at the surface. However the higher the acceleration voltage, the lower numbers of electron-hole pairs are generated (Figure 2.6) therefore the net result is a low induced current. As the acceleration voltage decrease, the depth of penetration decreases and the number of electron-hole pairs increases. Therefore the net result is an increase in the induced current. With further decrease in the acceleration voltage, although the depth of penetration decreases and the number of electron-hole pairs increases, the effect of surface recombination becomes more prominent. This results in a decrease in the induced current because more of the generated excess carriers are recombining before they have a chance to collected at the contacts.

From this information, both the L-EBIC and the T-EBIC systems acceleration voltages were set to 10 kV when measuring the data for the diffusion length. This was performed to ensure the maximum induced current for type IIa natural diamond would be measured.

6.3.1 EBIC Testing

Both the L-EBIC and the T-EBIC systems were used to obtain the diffusion length of the type IIa natural diamond. The diffusion current was measured with respect to distance across the sample in hopes of verifying that these samples did indeed perform as predicted by their theoretical calculations. For the T-EBIC system the acceleration voltage was set to 10 kV with a primary current of 8.35 nA at bias 3 and the L-EBIC system was adjusted to 15 kV with a primary current of 10.5 nA. The results of the T-EBIC system can be seen in Figure 6.16 and the results of the L-EBIC system in Figure 6.17.

The results indicated that the measured T-EBIC data was greater than its theoretical values for most of the distance between the contacts by at least 31 % except at the measuring contact. At this point the deviation was approximately 70 % below the

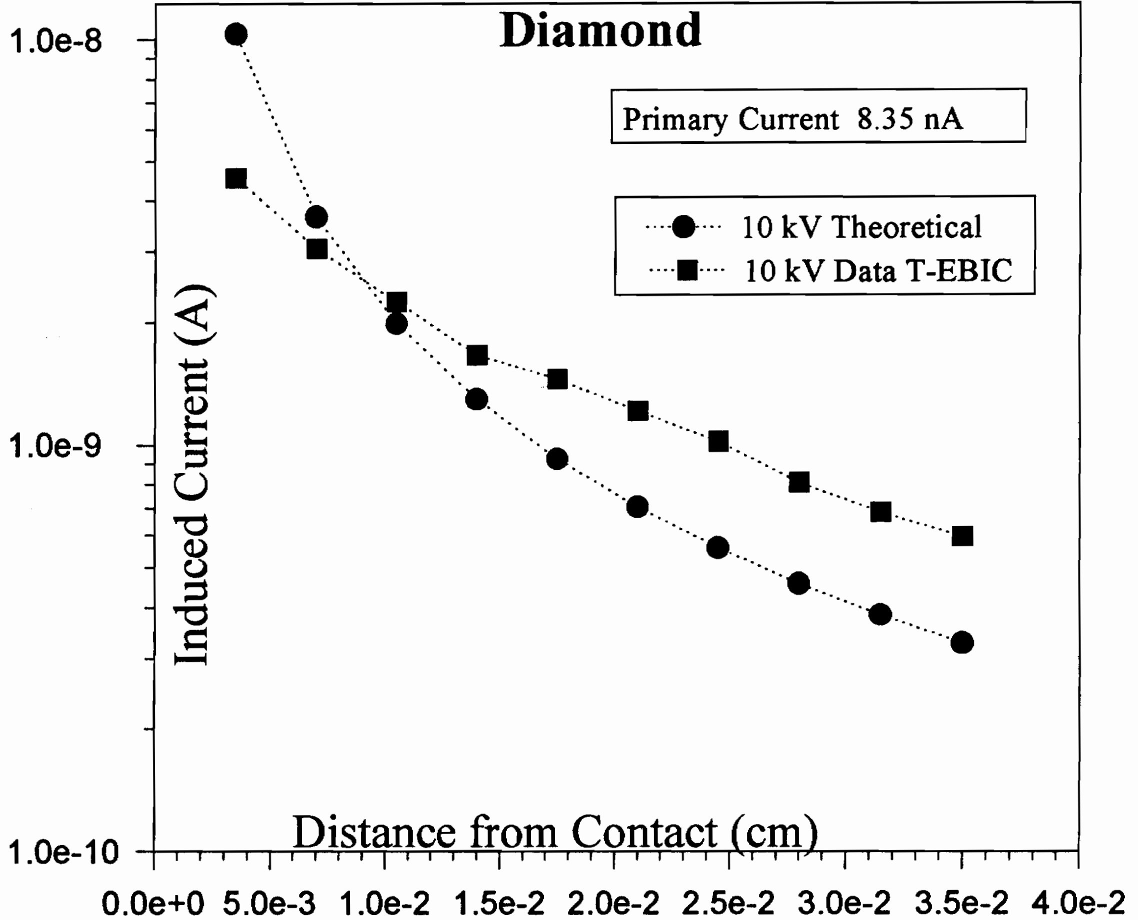

Figure 6.17. Comparison of Theoretical & Measured Diffusion Current in T-EBIC.

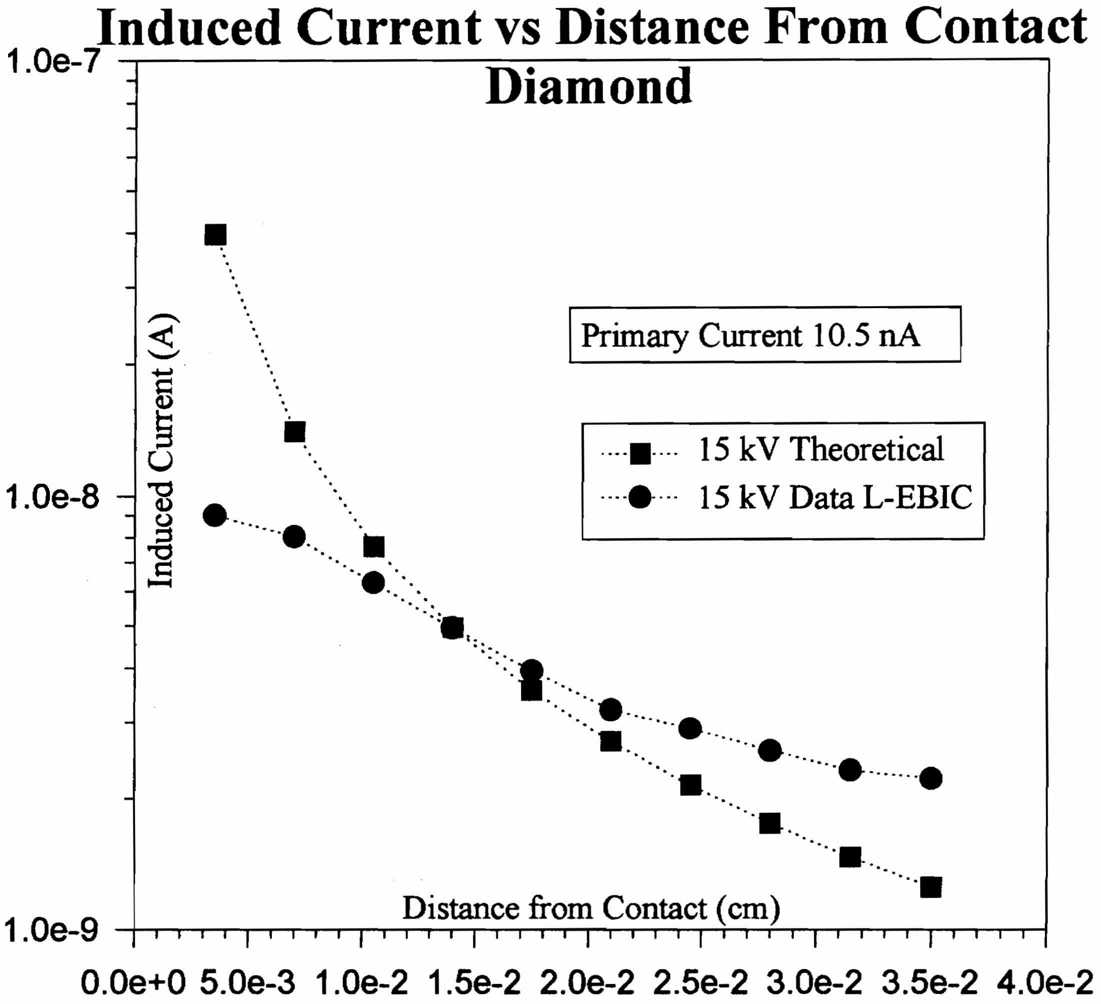

Figure 6.18. Comparison of Theoretical & Measured Diffusion Current in L-EBIC.

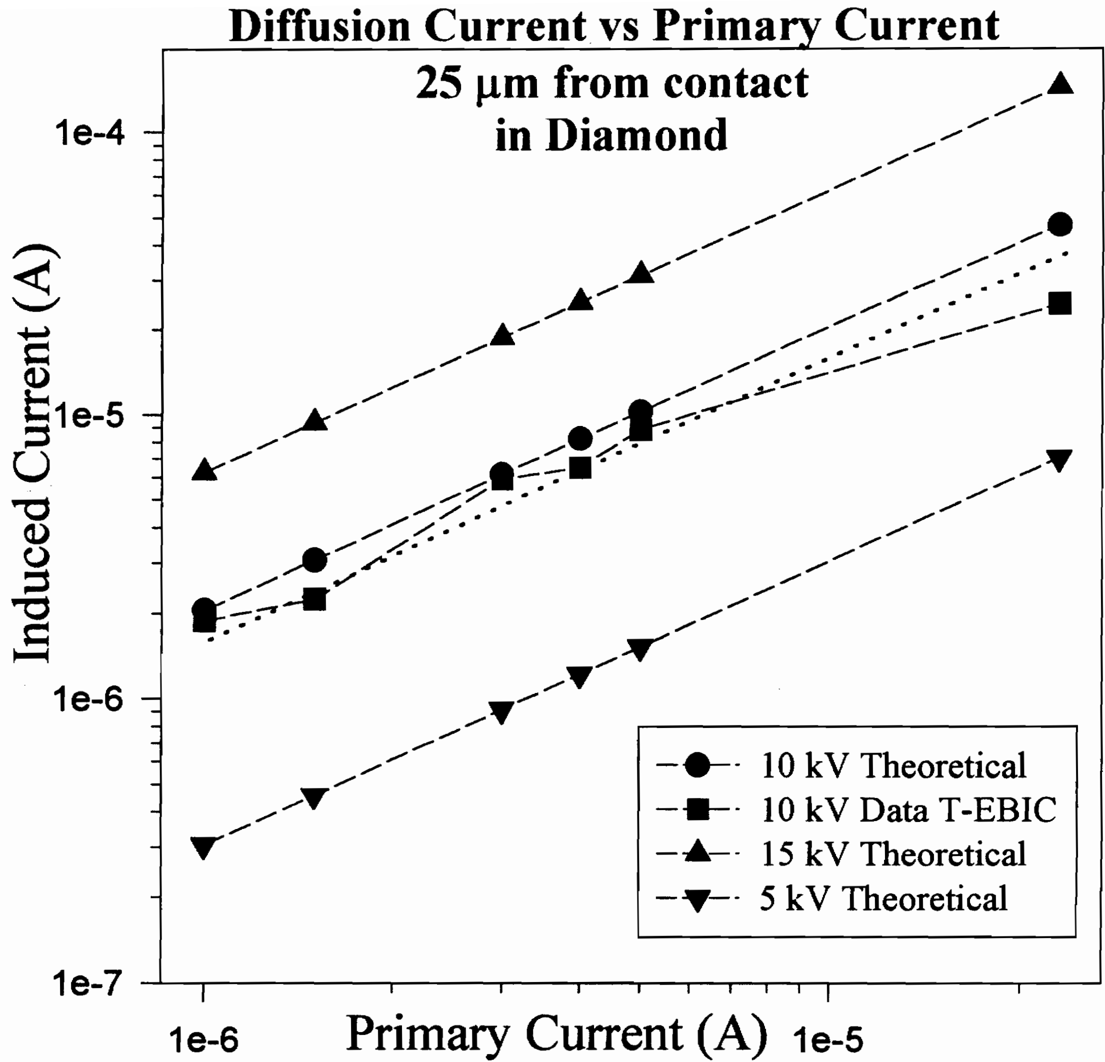

Figure 6.19. Comparison of Theoretical & Measured Diffusion Current vs Primary Current in T-EBIC.

theoretical values. The reason for the drop off close to the measuring contacts is believe to be due to the unintentional doping type effect of the contacts that increased the trapping centers in that area. For the L-EBIC system the measured data behaved the same, at least 11 % above the theoretical values, everywhere but close to the measuring contact. At the measuring contact the deviation was approximately 77 % below the theoretical values.

Using the T-EBIC system the diffusion current was measured versus the primary current to the sample. This was performed to verifying that the electron beam induce current gain of type IIa natural diamond matched theoretical calculations (Figure 2.10b). The results of the test can be seen in Figure 6.18. The basic patterns for both the theoretical and experimental values were the same, but the deviation between the two tended to increase with increasing primary current. The dashed line represents the average induced current which deviated by 20 % from the theoretical values. However the results of all the diffusion current test showed that the samples did produced significant amounts of electron beam induced current to be used to obtain the diffusion length in type IIa natural diamond.

Both L-EBIC and T-EBIC systems were used to obtain the diffusion length in type IIa natural diamond. Both the L-EBIC and the T-EBIC systems operated at an acceleration voltage of 10 kV. The primary current for the L-EBIC system was 10.5 nA and for the T-EBIC system it was 8.35 nA. The sample was exposed to the electron beam and the induced current was measured as a function of distance.

The data taken from the electron beam induced current with respect to distance across the sample was substituted into equation 2.69 and the diffusion length was extrapolated. The extrapolated diffusion length was obtained by curve fitting the data of $\ln(I_{ph}d^{3/2})$ versus d, where I_{ph} was the photoinduced current and d was the distance of the sensitive region between the contacts. The results of the diffusion length in type IIa natural diamond for both L-EBIC and T-EBIC systems can be seen in Figure 6.19.

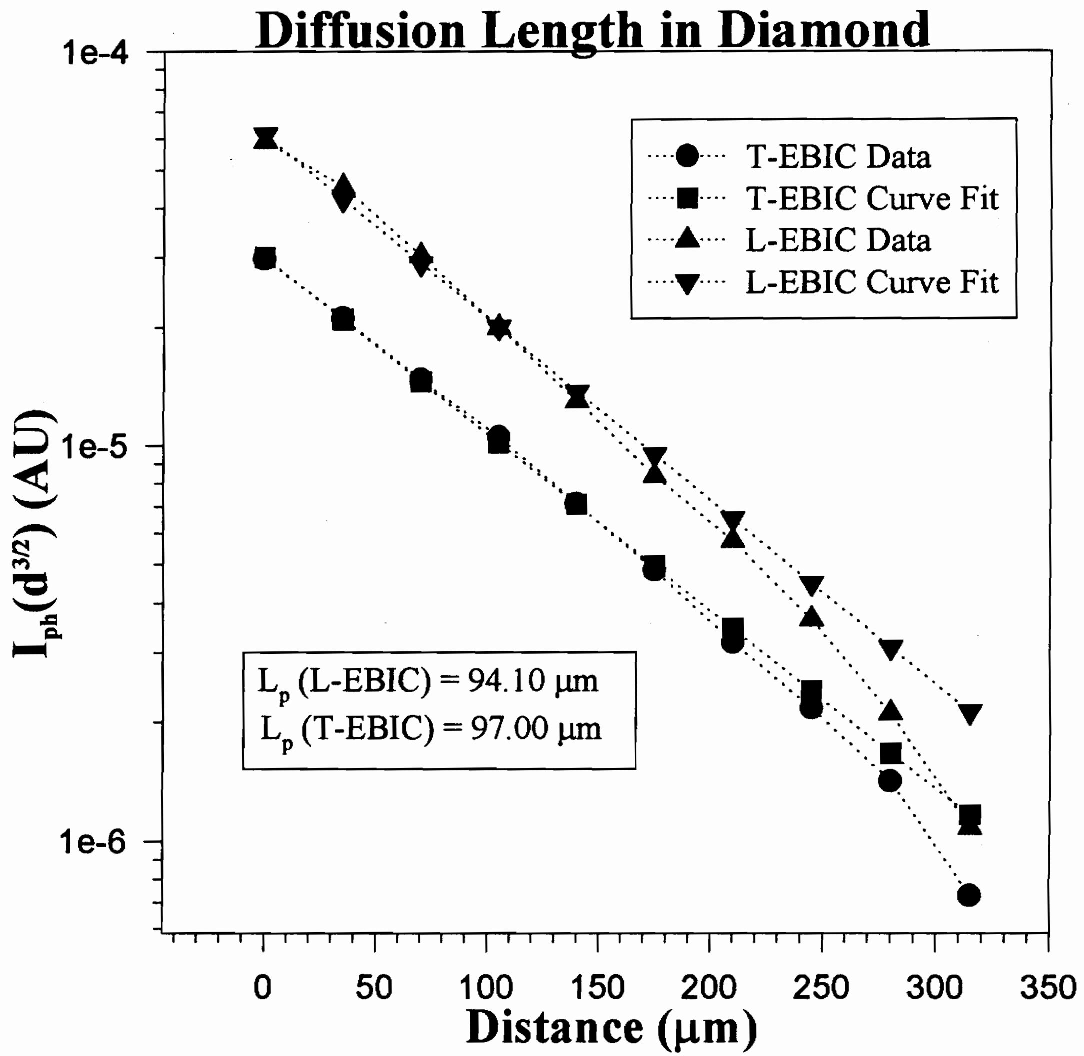

Figure 6.20. Diffusion Length for Type IIa Natural Diamond.

The L-EBIC system diffusion length results for type IIa natural diamond was found to be 94.10 μm ± 5 % and the T-EBIC system diffusion length results was found to be 97.00 μm ± 1 %[58,61,62]. These results were similar to work performed on the collecting distance of type IIa natural diamond by Plano et al.[63] (30 μm) and Pan et al.[64,65] (50 μm and 160 μm).

6.4 Discussion of Results and Conclusion

The purpose of the research was to obtain diffusion lengths, carrier lifetimes and verify the high resistivity of two wide bandgap materials. As discussed in chapter 6 the goals of this project were achieved. The diffusion length of GaN was measured to be 7.84 μm and 7.78 μm by the L-EBIC and T-EBIC systems respectively. After annealing out some of the inherent impurities in the material the diffusion length increased to 9.89 μm when measured in the L-EBIC system. The data suggested that the areas closer to the collecting contact had a higher level of impurities, which may have developed during deposition of the metallization for the contacts. The data taken on the diffusion length of GaN all were within a 10 % spread.

The carrier lifetime measured for the GaN material using the OBIC system was 3.36 and 3.9 ns. This double exponential fit indicated that more than one recombination process was present. This is typical for recombination processes near the interface and surface of materials. Therefore the author believes that the results obtained from the OBIC system were for the combine surface and interface carrier lifetimes. The carrier lifetime results obtained from the L-EBIC system was 1.7 μs. This value is much longer than the OBIC results and it is believed to be the lifetime within the material. In the EBIC system the generated excess carriers were achieved at a location approximately one third the depth of the material. At this position the surface and interface traps was not a significant factor in the recombination of the carriers. Therefore the author believes that

the lifetime obtained is a good representation of the effective thin film carrier lifetime of GaN, due to the more dominant SRH and Auger recombination processes. Findings by Baur et al.[66] showed that the iron and chromium were the main minority carrier lifetime limiters in epitaxial grown GaN. Indicating that along with Auger, deep level impurities play a significant role in the recombination process of GaN.

The resistivity for the GaN samples varied from 1.79 x 10^{10} Ω-cm to 4.09 x 10^{6} Ω-cm, with the 25 μm spacing transmission line structure providing the highest resistivity value. The resistivity measured for the type IIa natural diamond was found to be 6.14 x 10^{10} Ω-cm. These resistivities correlated with results found by Hofsas et al.[67], Konorava et al.[68], Pan et al.[69], and Grot et al.[70] for diamond. Using the type IIa natural diamond sample the maximum induced current gain was found to occur at an acceleration voltage of 10 kV.

The diffusion length of type IIa natural diamond was measured to be 94.10 μm and 97.00 μm by the L-EBIC and T-EBIC systems respectively. All the data values taken were within 5 % spread. The data points taken for the T-EBIC system were remarkably close to each other. Most of the research performed to this date, except Pleskov estimation, has stayed away from measuring the diffusion lengths of diamond and GaN because of their low dark current in their intrinsic form.

Pleskov et al.[71] developed a photoelectrochemical estimation of the diffusion length in synthetic diamond. Pleskov estimated using the absorption coefficient, light intensities and the corresponding wavelength values, that the diffusion length ranged from 2 μm to 4 μm. However Plano et al.[63] and Pan et al.[64,65] have obtained collecting distance or drift lengths for both type IIa natural and CVD diamond as high as 160 μm. Plano found for an applied field of 10 kV/cm the drift length was 30 μm[63], and Pan found at an applied field of 2 kV/cm the drift length was 50 μm[64] and 160 μm[65]. Although, the difference between these reported results and the findings of the research were noticeable, they were expected. The results presented here represents the actual diffusion

of carriers across the materials without an applied field, unlike Plano and Pan results. These results add to the unique nature of this research project.

6.4.1 Future Work

The results obtained from this research project has proven to be very successful in the understanding the diffusion of carriers in type IIa natural diamond and GaN, as well as the effective carrier lifetime at the surface and in the bulk of GaN materials. However, the potential for future work in this field, using the EBIC system is remarkable. Areas in which the author feels that this project can be applied in future applications are:

- Measuring the carriers lifetime of diamond and other wide bandgap materials, in particular Silicon Carbide (SiC) and Aluminum Nitride (AlN).
- Obtaining the drift velocity versus electric field curves for wide bandgap materials.
- Measuring the saturation velocity of these wide bandgap materials.
- Improving the emission current of the photoemission system.
- Increasing the sensitivity of the detection system by further reducing the space charge effects.
- Obtain a set of standard transport property parameters for wide bandgap materials.
- Comparison of synthetic grown diamond transport properties with that of natural diamond.

6.4.2 Summary and Conclusion

The electrical transport properties for diamond and Gallium Nitride materials have presented experimental problems in measuring. The most commonly used technique

conventional Hall measurements are difficult to accomplish because of the minuscule currents that flow in the intrinsic forms of these materials at room temperature. The technique that was effective in providing a direct approach in the investigation of transport properties was the time of flight transient measurement technique. The diffusion length, carrier lifetime and resistivity were extracted from the measurements of the drift/diffusion of carriers across the sample. This process was a device-oriented measurement technique and so very useful particularly for high resistivity near insulating materials. This research project obtained the carrier transport properties in two of the wide bandgap materials GaN and diamond.

The two techniques used to generate electron-hole pairs in this project, to obtain the transport properties, were optical beam induced current (OBIC) and electron beam induced current (EBIC) time of flight transient measurement techniques. These techniques consisted of measuring the current transient and steady state response to the drift/diffusion of carriers created by a short-duration pulse of radiation. A high field region was created with low levels of dark current, when an applied voltage was placed across the high resistivity materials with noninjecting contacts. The measurement of the transit time across the high field region led to the determination of the carrier lifetime. Under steady state condition, the diffusion current was measured with respect to the distance across the sample and the diffusion length extracted.

In the OBIC system, the carriers were generated throughout the material where surface and interface recombination velocities were generally higher. The resultant carrier lifetimes obtained from this system were considerably short. Some of the problems encountered experimentally were: the generation of the required optical pulses, the elimination of space charge effects, and the generation of sufficient numbers of excess carriers for analysis on the detection system. With the optical source, short duration pulses with the required spot size, in the required spectral range, with an electron beam excitation pulse time much less than the transit time of the material was needed. Here, free carrier lifetimes were the limiting factor, requiring short drift regions. The difficulty

arose in that with decreasing pulse width the number of photons per pulse decreased. The decline in photons per pulse eventually became too small for the production of enough charge carriers suitable for measurements with wide band electronic equipment. After overcoming these difficulties, the results showed that sufficient numbers of excess carriers were generated and the carrier lifetime was successfully measured.

The second technique of excitation used in this project was the EBIC method. This technique involved the use of high energy fast electrons to generate the excess carriers. A photoemissiom source and pulse thermal source was used to generate an electron beam that interacted with the sample. This interaction resulted in the generation of free carriers within the material. The location and number of free carriers were varied by altering the acceleration of the electron beam. The main problem encountered with this method was controlling the buildup of excess carriers within the samples. This was overcome by pulsing either the sample or electron beam. The preliminary test showed that the optimum condition for maximum detection of the electron beam induced current was with an acceleration voltage of 10 kV. For this setting the results of the diffusion lengths and carrier lifetimes were obtained from the EBIC systems.

The proposed goals of this research project, obtaining the diffusion lengths, carrier lifetimes and verify the high resistivity of diamond and GaN, was achieved by using a combination of OBIC, L-EBIC and T-EBIC systems. Future research in this area may involve the improvement of the measuring system to obtain the drift velocity and mobility measurements of any wide bandgap material. In addition this system may be used to obtain saturation velocities for diamond and GaN materials, as well as any other wide bandgap material.

References

1. S.C. Binari, H.B. Dietrick, G.Kelner L.B. Rowland, F.Doverspike and D.K. Gaskill, Electronics Letters 30, 11, p.909, 1994.
2. J.L. Davison, Proc. Third International Symposium on Diamond Materials, CECS Proc., p.93, 1993.
3. S.C. Binari, M. Marchywka, D.A. Koolbeck, H.B. Dietrich and D. Moses, Diamond and Related Materials, 2, p.1020, 1993.
4. H. Hillmer, G. Mayer and A. Forchel, Applied Physics Letters, 49, p.948, 1986.
5. D.J. Westland, D. Mihailovic, J.F.Rayen and M.D. Scott, Applied Physics Letters 51, p.590, 1987.
6. C.B. Norris, Jr., and J.F. Gibbons, IEEE Transactions on Electron Devices, ED-14, p.38, 1967.
7. B. Gudden and R.W. Phohl. Zeitschrift fuer Physik, 16, p.170, 1923.
8. B. Gudden and R.W. Phohl. Zeitschrift fuer Physik, 6, p.248, 1921.
9. K. Hect, Zeitschrift fuer Physik, 77, p.235, 1932.
10. P.J. Van Heerden, Physics Review, 106, p.468, 1957.
11. R. Hofstadter, Nucleonics 4 (4), p.2, 1949; 4 (5), p.29, 1949.
12. W.E. Spear, Physics Review Letters 8, p.3141, 1962
13. W.E. Spear, Journal of Non-Crystal Solids 1, p.197, 1970.
14. J.R. Haynes and W.S. Schockley, Physica Review, 81 p.835,1951
15. J.R. Haynes and W.S. Schockley, Physica Review, 82 p.935,1951
16. E.M. Conwell, "High Field Transport in Semiconductors", Academic Press, New York, 1967.
17. A. Many and G. Rakavy, Physics Review, 126, p.1980, 1962.
18. A. Many, S.Z. Weisz and M. Simhony, Physics Review, 126, p.1989, 1962.
19. W.E. Spear, H.P. Lanyon and J. Mort, Journal of Scientific Instrument, 39, p.81, 1962.
20. C.J. Scott, "Electron Beam Testing Using a Photocathode Scanning Electron Microscope", Ph. D. Thesis, Howard University, 1991.
21. W. Ehrenberg and D.E. King, Proc. of the Royal Society of London 81, p.751, 1963.
22. R.N. Hall, "Recombination Processes in Semiconductors", Proc. IEEE, 106B, p.923, 1960.
23. W. Shockley and W.T. Read, Physics Review, 87, p.835, 1952.
24. Y.P. Varshni, Physica Status Solidi, 19, p.459, 1967; ibid. 20, p.9, 1967.
25. J.G. Fussum, R.P. Mertens, D.S. Lee and J.F. Nijs, Solid-State Electron, 26, p.569, 1983.
26. D.J. Fitzgerald and A.S. Grove, Surface Science, 9, p.347, 1968.
27. M. Boulou and D. Bois, Journal of Applied Physics, 48, p.4713, 1977.
28. J.S. Blakemore, "Semiconductor Statistics", Pergaman, New York, 1962.
29. V.L. Bonch-Bruevickk and E.G. Landsberg, Physica Status Solidi, 29, p.9, 1968.
30. G.A. Dussel and R.H. Bube, Journal of Applied Physics, 37, p.2797, 1966.

31. M. Lax, Physics Review, 119, p.1502, 1960.
32. R.H. Bube, "Photoconductivity of Solids", John Wiley, New York, 1960.
33. K.R. Zanio, W.M. Akutagawa and R. Kikuchi, Journal of Applied Physics, 39, p.2818, 1968.
34. J.W. Mayer "Semiconductor Detector" (G. Bertalini and A. Cocks, eds.) Ch #5 North Holland, Publ., Amsterdam, 1968.
35. T.E. Everhart and P.H. Huff, Journal of Applied Physics, 42, p.5837, 1971.
36. A.E. Given, Z. Naturforsch, 12 A, p.89, 1957.
37. V.E. Casslett and R.N. Thomas, Britain Journal of Applied Physics, 15, p.1283, 1964.
38. D.B. Wittey and D.K. Kyser, Journal of Applied Physics, 38, p.375, 1967.
39. M.J. Berger and S.M. Seltzer, National Academy of Science-National Research Council Publ. no.1133, p.205, 1964.
40. J.R. Fiebiger and R.S. Muller, Journal of Applied Physics, 43, p. 3202, 1972.
41. C.A. Klevin, Journal of Applied Physics, 39, p.2029, 1968.
42. J.F. Bresse, Scanning Electron Microscopy, 1, p.717, 1978.
43. D.K. Schroder, "Semiconductor Material and Device Characterization", John Wiley, New York, 1990.
44. F. Berz and H.K. Kulken, Solid State Electron, 19, p.437, 1976.
45. D.E. Inoannov and C.A. Dimitriadis, IEEE Transitions on Electron Devices, ED-29, p.445, 1982.
46. D.J. Gibbons and A.C. Papadakis, Journal of Physics and Chemistry of Solids, 29, p.115, 1968.
47. K. Kato, IEEE Journal on Quantum Electronics, QE-22(7), p.1013, 1986.
48. T.E. Everhart and R.F. Thornley, Japan Journal of Applied Physics, 10, p.678, 1971.
49. P.E. Ottinge, Applied Physics Letters, 56, p.333, 1990.
50. Tyagi, "Introduction to Semiconductor Devices", John Wiley, New York, 1991.
51. A.A. Millings II, S. Brown, C.J. Scott and A.D. Cropper, Proc. Third National Conference on Diversity in The Science & Technology Workforce, Washington D.C. 1994.
52. E. Menzal and E. Kubalak, Scanning Electron Microscopy, 1, p.305, 1979.
53. T. Hosckawa, H. Fujioka and K. Ura, Review of Scientific Instruments 49(3), p.624, 1978.
54. W. Zimmermann, Physica Status Solidi (a), 12, p671, 1972.
55. S.M. Sze, "Physics of Semiconductor Devices", John Wiley, New York, 1981.
56. C. Canali, C. Jacoboni, F. Nava, Physics Review B, 12, no.4, p.2265, 1975.
57. A.G. Evans and P.N. Robson, Solid-State Electronics, 17, p.805, 1074.
58. A.D. Cropper, D. Moore, C. Scott and R. Green, SPIE Proc. XXVI Annual Symposium on Optical Material for High Power Lasers, 1994.
59. A.D. Cropper, C. Scott, and D. Moore, Proc. Fifth International Conference on the Formation of Semiconductor Interface, 1995.
60. D.L. Comphausen and G.A.N. Connell, Journal of Applied Physics, 42, (11), p.4438, 1971.

61. A.D. Cropper, C. Scott, D. Moore, S. Binari and D. Wickenden, Electrochemical Society Proc. Fourth International Symposium on Diamond Materials, 1995.
62. C.J. Scott, A. Cropper, A. Millings, D. Moore and S. Binari, Proc. Third International Conference on the Applications of Diamond Films & Related Materials, 1995.
63. M.A. Plano, M. Landstrass, M. Pan, L. Han S. Kanie, Science, 260, no.5112, p.1310, 1993.
64. L.S. Pan, S. Han, D.R. Kania, M.A. Plano and M.I. Landstrass, Diamond and Related materials, 2, no5-7, p.820, 1993.
65. L.S. Pan, S. Han, D. Kania and W. Banholzer, Materials Research Society Symposium Proc., 302 p.299, 1993.
66. J. Baur, K. Maier, M. Kuncer, U. Kaufman, J. Schneider, H. Amano, I. Akasaki, T. Detchprohm and K. Hiramatsu, Applied Physics Letters, 64, no.7, p.857, 1994.
67. H. Hofsass, H. Binder, T. Klumpp and E. Recknagel, Diamond and Related Materials, 3, no1-2, p. 137, 1994.
68. E.A. Konarava and S.A. Sherchenko, Soviet Physics-Semiconductor, 1, no.3, p.299. 1967.
69. L.S. Pan, D.R. Konia, P. Pianetta, O.L. Landen. Applied Physics Letters, 57, no.6, p.623, 1990.
70. S.A. Grot, C.W. Hatfield, G. Gildenblat, A. Badizam and T. Badziam, Applied Physics Letters 58, no.14, p.1542, 1991.
71. Y.U. Pleskov, A.Y. Sakharova, E.V. Kasatkin and V.A. Shepelin, Journal of Electroanalytical Chemistry v.344, no.1-2, p.401, 1993.
A1. W.Shockley, Journal of Applied Physics, 9, p.635, 1938.
A2. W.E. Tefft, Journal of Applied Physics, 38, p.5265, 1967.
A3. G.W.Bradberry and W.E. Spear, Britain Journal of Applied Physics, 15, p.1127, 1964.

Appendix A.

EBIC Drift Velocity and Mobility Considerations

As discussed in section 2.3 and 6.4.2, the next progressive step would be to measure the drift velocity and mobility for wide bandgap materials. In order to accomplish this task, some understanding of the EBIC method as it applies to the transient case with an applied electric field must be considered. This appendix will introduce the reader to some of the basic theory and limitation that must be considered for drift velocity and mobility measurements.

A.1 Transport Equations

The extraction of the transport properties from the EBIC or OBIC time of flight transient measurement technique, requires the generation of free carriers within the MUT by an electron beam pulse in a reasonable uniform electric field. The duration of the excitation pulse (t_e) should be much shorter than the transit time (T_R) of the generated carriers across the sample. If the absorption depth (δ), of the excitation is kept much smaller than the sample thickness d, then a narrow sheet of charge carriers of one sign traverses the sample as shown in Figure A.1. The generation of N carriers in a surface area (A) creates a sheet of charge at $x = x'$ within an applied field. This drifting sheet of charge carriers will modify the applied field ($E_a = V_a/d$) and the solution to Poisson's

equation (2.4) subject to these conditions, for the electric field before (E_1) and after (E_2) the injected sheet of carriers can be expressed as [13]:

$$E_1(x') = E_a - E_{self}\left(1-\frac{x'}{d}\right) \tag{A.1}$$

$$E_2(x') = E_a + E_{self}\left(\frac{x'}{d}\right) \tag{A.2}$$

where ε is the dielectric constant of the material and

$$E_{self} = \left(\frac{4\pi N e}{\varepsilon A}\right) \tag{A.3}$$

is the self-field of the moving sheet of carriers. The drifting carriers will perturb the field

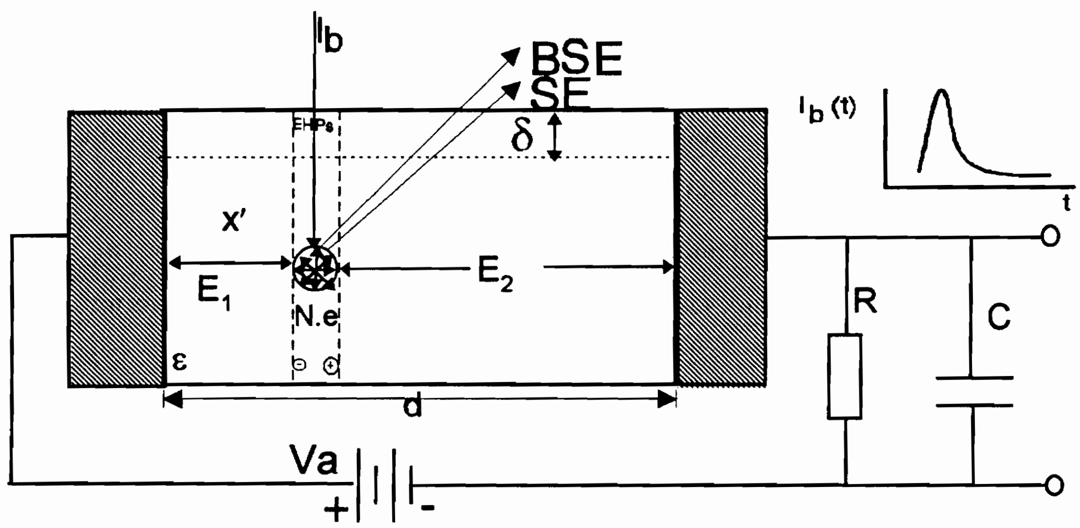

Figure A.1. Electron-Hole Pairs Generation in Samples.

within the sample, but if N is kept small so that the self-field $E_{self} << E_a$, the internal field

can be taken as V_a/d. This description of carrier transport applies to an insulating or near insulating material in which the dielectric relaxation time is very much longer than the transit time.

There are two ways in which the transit time of the carriers can be determined. The first relies on charge integration and here the R′C′ time constant is made much larger than the transit time (T_R). The (C′) total capacity across resistor R′ includes that of the sample, the leads, and the input of the detecting system. The changing fields E_1 and E_2 produced from the generated carriers drifting across the sample, will cause a re-distribution of charge on the contacts. For the right contact;

$$\Delta q = \frac{Nex'}{d} \qquad \text{A.4}$$

the resulting potential drop across the resistor at the input of the detecting system is given by:

$$\Delta V(t) = \left(\frac{Ne}{C'd}\right) v\, t \qquad 0 < t < T_R \qquad \text{A.5}$$

$$\Delta V(t) = \frac{Ne}{C'} \qquad t > T_R \qquad \text{A.6}$$

where the drift velocity is $v = d/T_R$, and is valid as long as $t \ll R'C'$.

Secondly from the duration of the current pulse produced by the drifting carriers, the transit time can be found. In this case R′ is reduce so that $C'R' \ll T_R$ and current pulse is given by[A.1]:

$$i(t) = \left(\frac{Ne}{d}\right) v \qquad 0 < t < T_R \qquad \text{A.7}$$

$$i(t) = 0 \qquad t > T_R \qquad \text{A.8}$$

and the voltage as:

$$\Delta V = R\left(\frac{Ne}{d}\right)v \qquad 0 < t < T_R \qquad A.9$$

$$\Delta V = 0 \qquad t > T_R \qquad A.10$$

An important consideration about these techniques, is that the lower limit on the transit time, is controlled by the overall rise time and spatial resolution of the electronic measuring equipment, including connections. This is more prevalent in the current pulse measuring technique than in the voltage integration method. However this can be compensated for, if the carrier generation concentration is made sufficiently large so that the resolution of the transit pulse can be detected. This increase in carrier generation concentration also affects the measuring system by creating the space charge buildup in the material. Therefore the result is a trade off between the two in order to observe the signal transit response.

If deep traps are present however, displaying of current pulses is more advantageous because, it is easier to determine the transit time and obtain a value for the free carrier lifetimes. In samples that have uniform field distributions and are relatively free of trapping effects the current pulse is nearly rectangular in shape. The current pulse time duration is given by the transit time of the carriers across the sample, as shown in Figure A.2. The transit time is given by:

$$T_R = \frac{d}{v} \qquad A.11$$

Once the transit time has been measured, the drift mobility is obtained from:

$$\mu = \frac{d}{E_a T_R} \qquad A.12$$

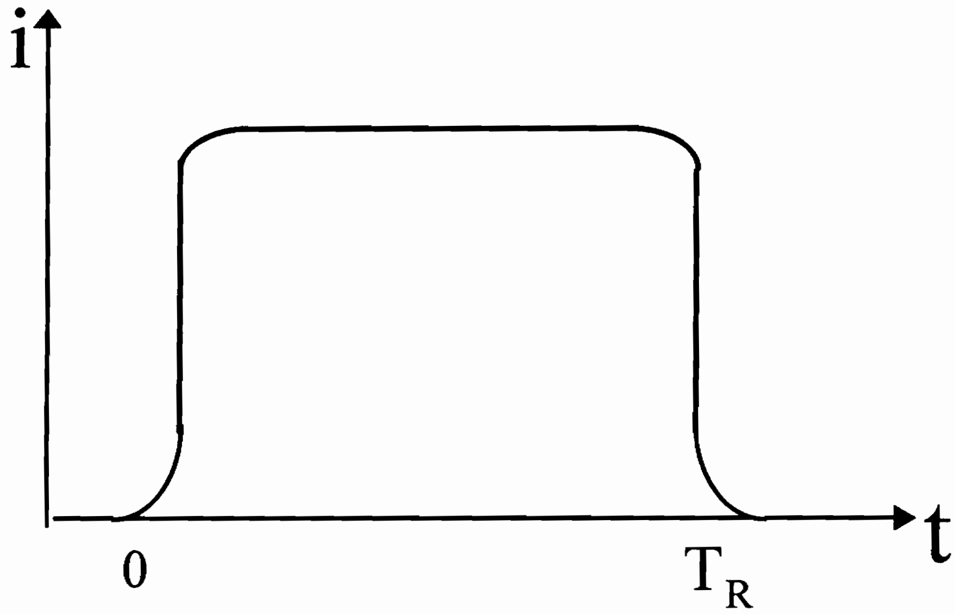

Figure A.2. Induced Current Response.

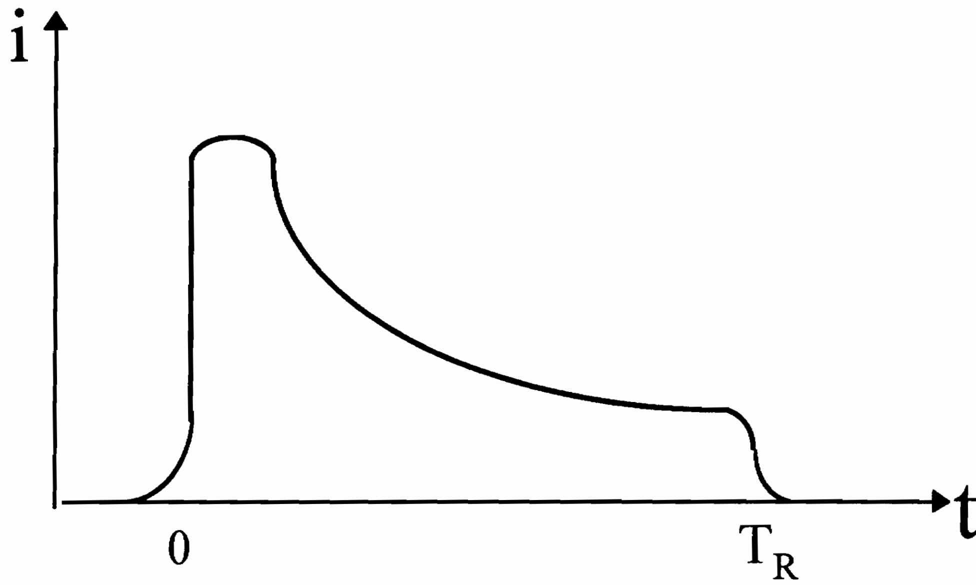

Figure A.3. Induced Current Response due to Deep Traps

The measurement of the width of the current pulse gives a direct indication of the drift velocity. Under conditions where the field distribution is non uniform or trapping effects are present, the shape of the current pulse is no longer rectangular as shown in Figure A.3. However, for certain conditions, the pulse shape is well enough defined to permit determination of the transit time and so extract the transport properties. When the carriers experience multiple trapping and release during their transit across the sample, the measurement of the current pulse length gives a reduced drift velocity.

A.2 Trapping Limitations

When trapping effects are present, they sometimes results in significant limitations in measuring the drift mobility and therefore should be addressed. A typical sample with both deep and shallow traps is shown in Figure A.4. Here, μ is the mobility of the free carriers n_o in the conduction band of the solid. The lifetime with respect to any particular group of traps, E_t below the band edge, is τ. The probability per sec of thermal release from these centers is denoted by l/τ_r. If the processes of these traps are of the single level trapping and de-trapping kind. Then for the single level of shallow electron traps under condition $\tau_r << T_R$, and $\tau << T_R$, the electron transit will be controlled by this trapping and de-trapping, as discussed in section 2.2.3.

The current and voltage equations (A.6 - A.10) for the transit pulse must be adjusted. The drift velocity term which is a function of the transit time must include a correction factor due to trapping. For the OBIC system, in the reduced mobility case, the generated carriers will travel across the material in an extended transit time given by:

$$T_R' = \frac{w}{\mu_r E} = \frac{T_R \mu_o}{\mu_r} \qquad \text{A.13}$$

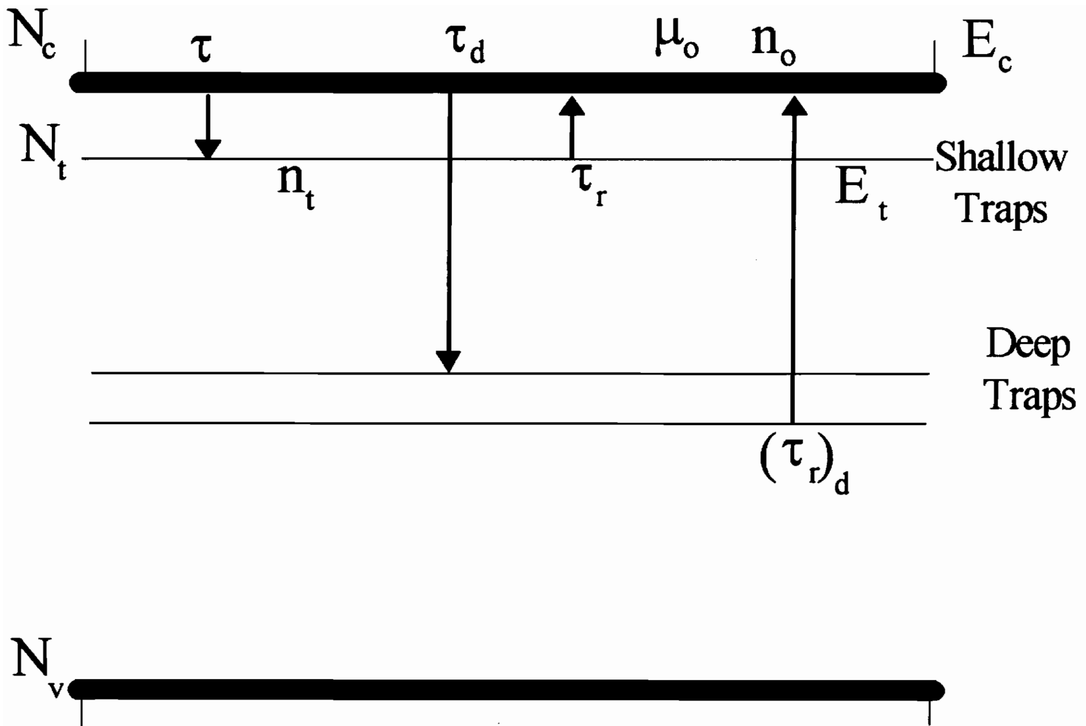

Figure A.4. Trapping Distribution in Samples

where μ_r is the reduced mobility [A.1] and is given by:

$$\mu_r = \mu_o \left[\frac{\tau^+}{\tau^+ + \tau_D} \right] \qquad \text{A.14}$$

and substituting equation 2.49 into equation A.14 gives:

$$\mu_r = \mu_o \left[1 + \left(\frac{N_T}{N_c} \right) \exp\left(\frac{E_T}{KT} \right) \right]^{-1} \qquad \text{A.15}$$

therefore, as the temperature increases the exponential term decreases, therefore $\mu_r \to \mu_O$ and $T'_R \to T_R$.

For the case where trapping is not significant ($\tau^+ \leq T_R$), the generated carriers penetrate some distance before being trapped. The result is an initial fast rising portion of the response is due to the drift of carriers ($t < T_R$) and is given by:

$$I = I_o \left\{ \frac{\tau^+ + \tau_D \exp\left[-\frac{\left(\tau^+ + \tau_D\right) t}{\tau_D \tau^+} \right]}{\left(\tau^+ + \tau_D\right)} \right\} \qquad \text{A.16}$$

and when their is little or no trapping $\tau_D \to \infty$ and equation A.16 goes to equation 2.51. Then second part of this response is a slowly decaying tail, due to the decrease in trapping and de-trapping processes and is given by[33,34,A2]:

$$I(t) = \frac{I_o}{T_R} \left(\frac{\tau^+}{\tau^+ + \tau_D} \right) \quad \text{for} \quad T_R < t < \left(\frac{\tau^+ + \tau_D}{\tau^+} \right) T_R \qquad \text{A.17}$$

and

$$I(t) = \left(\frac{I_o T_R}{\tau_D \tau^+}\right) \exp\left(-\frac{t}{\tau_D}\right) \quad \text{for} \quad t > T_R \qquad \text{A.18}$$

and in terms of the concentration can be written as:

$$T_R' \approx T_R \left(\frac{N_T}{N_c}\right) \exp\left(\frac{E_T}{KT}\right) \qquad \text{A.19}$$

where N_C and N_T refers to the density of states in the conduction band and density of the traps.

The reduced drift mobility for trapping in the EBIC system as given by equation A.15 is:

$$\mu' = \mu \left[1 + \left(\frac{N_t}{N_c}\right) \exp\left(\frac{E_t}{KT}\right)\right]^{-1} \qquad \text{A.20}$$

At sufficiently high temperatures, the probability of thermal release is high, the term $(N_T/N_C)\exp(E_T/KT)$ decrease which leads T'_R to T_R and $\mu' \approx \mu$. With decreasing temperatures, the second term in the denominator rapidly becomes dominant and the corrected drift mobility is given as:

$$\mu' = \mu \left[\left(\frac{N_c}{N_t}\right) \exp\left(-\frac{E_t}{KT}\right)\right] \qquad \text{A.21}$$

Therefore at high temperatures, shallow traps ($\tau_r << T_R$) have no effect on the measured drift mobility and the measured value is equal to the lattice mobility in the

particular band. With decreasing temperature an increasing fraction of the measured transit time will be due to the localization of the drifting carriers in the shallow centers. This however does not normally affect the experimental results because the density of these defects can be reduced by heat treatment[(A3)].

The second group centers (or the deep traps, defined by $\tau_{rd} >> T_R$) effect on the measurements will depend on the lifetime τ_d of the free carriers with respect to deep trapping. If $\tau_d > T_R$, then the presence of deep centers will have little effect. However, for instances where $\tau_d \approx T_R$, there will be a loss of free carriers during the transit, and N is no longer a constant in the equation for current and voltage. The pulses will have the form of Figure A.3 and T_R can still be obtained from current pulse. Therefore, the drift mobility can still be found from equation A.11.

Vita

Andre' Dominic Anthony Peter Cropper, born August 4th 1961 to Anthony and Vilma Cropper in the sunny caribbean islands of Trinidad and Tobago. Andre' attended New Town Boys School and Fatima College in Trinidad before departing for the United States of America to pursue a degree in Electrical Engineering. At Howard University Andre' obtained a Bachelor of Science in Electrical Engineering (Cum Laude) on 12th May 1984 and a Master of Engineering on 25th July, 1987. After teaching for four years at Norfolk State University, Andre' attended Virginia Polytechnic Institute and State University and earned a Doctorate Degree in Electrical Engineering on 12th May 1995. His resume reads as follows:

OBJECTIVE
Special interest in teaching at the University Level and performing further research in the field of semiconductor development.

EDUCATION

Doctor of Philosophy: Electrical Engineering,	Virginia Polytechnic Institute and State University, Blacksburg Va. 24061-0111. 12th May, 1995.
Master of Engineering: Electrical Engineering,	Howard University, Washington, D. C. 20059 25th July, 1987.
Bachelor of Science: Electrical Engineering,	Howard University, Washington, D. C. 20059 12th May, 1984.

EMPLOYMENT

1992-1995:	Virginia Polytechnic Institute and State University, Teaching/Research Assistant; School of Engineering.
Sum. (93 & 94):	Morgan State University Research Associate, Electronic Characterization Lab.
Sum. (90 & 92):	Morgan State University Director; NASA/Morgan Engineering Enrichment Program.
1990-1992:	Norfolk State University Instructor; School of Technology.
Sum. (91):	Consultant; Advanced Controls & Equipment Services, Freeport, Bahamas.
1988-1990:	Norfolk State University Part-time Instructor; School of Technology.

TEACHING RESPONSIBILITIES (at Norfolk State University)

Conduct classes in electronics, circuits, and introduction to microwave.
Acting Chairperson, Engineering Technology Program 1990-1992.
Member of CISE Infrastructure Planning Task Force, 1989.
Member of International Studies Task Force, 1989-1990.
Member of School of Technology Recruitment and Publicity committee, 1989-1990.
Chairperson of School of Technology Retention and Activity committee, 1989-1990.
Member of School of Technology Advisory committee 1988-92.

RESEARCH EXPERIENCES

Electrical Characterization of Wide Bandgap Materials under Dr. Moore, & Dr. Scott at Virginia Tech/Morgan State University, 1992-1994.

Development of Thin Film Diamond for National Science Foundation, under Dr. White, at Morgan State University, 1989-1991.

Characterization of Thin Film Diamond under Dr. Albin at Old Dominion University/NASA Langley, 1987-1988.

Designed and Characterized a Microwave Wafer Probe, under Dr. Spencer, at Howard University, 1984-1987.

PUBLICATIONS

"Diffusion Lengths in Diamond and Gallium Nitride Materials", Proc. Third International Conference on the Applications of Diamond Films & Related Materials, 1995.

" Electrical Characteristics of Gallium Nitride Layer on Sapphire Substrates", Proc. Fifth International Conference on the Formation of Semiconductor Interface, 1995.

"Diffusion Lengths in Diamond and Gallium Nitride Materials" Proc. Fourth International Symposium on Diamond Materials, 1995.

"An Electron Beam Induced Current Study of Gallium Nitride and Diamond Materials" Proc. Annual Symposium on Optical Materials for High Power Lasers, 1994.

"Damage Threshold Characterization of Thin Film Diamond" Proc. Third International Symposium on Diamond Materials; CECS Proc. 93-17, Pennington, 1993, p. 682.

"Laser Damage Threshold of Diamond Films" Optical Engineering, March 1989, vol. 28 No. 3 p. 281-285.

"Diamond for Solid State Laser Application & A Microwave Plasma Deposition System for Laboratory Use" Virginia Academy of Science, 1988.

"A Novel Design, Fabrication and Measurement of an X-Band Microwave Wafer Probe" (Master's Thesis Howard University, 1997.)

HONORS

Who's Who of Science and Engineering, 1994.
Teacher of the Year 1991, School of Technology, Norfolk State University.
Dean's List and Engineering Honor Roll, at Howard University.
Member of Beta Kappa Chi (Science Honor Society) at Howard University.
Member of Tau Beta Pi (Engineering Honor Society) at Howard University.
Outstanding Young Men of America Award, 1988.

ACTIVITIES

Vice President, Black Graduate Student Association @ Virginia Tech., 1993-1994.
Member of Virginia Tech. Water Polo Club. 1992-1994.
Special Guest Speaker @ St. Paul's High School, March 1991.
Member of Grand Bahama Players Theater Group, 1991.
Member Worship Committee, Christ the King Catholic Church, 1991.
Member of Tidewaterpolo Water Polo Club, 1989-1991.
Assistant Swim Coach @ Howard University, 1984-1987.
President, Graduate Student Council @ Howard University, 1984-87.
President, Engineering Student Association @ Howard University, 1984-87.
Most Outstanding Swimmer @ Howard University, 1982-84.
Outstanding Academic Athlete Mid-Eastern Athletic Conference Swimming,, 1982-84.
Member of Alpha Phi Alpha Fraternity.